POLYTECHNIQUE MONTRÉAL
affiliée à l'Université de Montréal

On the Mechanics of Flow-Induced Vibration of Soft Corals and Particle Interception

MOUAD BOUDINA
Département de génie mécanique

Mémoire présenté en vue de l'obtention du diplôme de *Maîtrise ès sciences appliquées*
Génie mécanique

Août 2020

© Mouad Boudina, 2020.

POLYTECHNIQUE MONTRÉAL
affiliée à l'Université de Montréal

Ce mémoire intitulé :

On the Mechanics of Flow-Induced Vibration of Soft Corals and Particle Interception

présenté par **Mouad BOUDINA**
en vue de l'obtention du diplôme de *Maîtrise ès sciences appliquées*
a été dûment accepté par le jury d'examen constitué de :

Sébastien LECLAIRE, président
Stéphane ÉTIENNE, membre et directeur de recherche
Frédérick GOSSELIN, membre et codirecteur de recherche
Christopher CAMERON, membre

ACKNOWLEDGEMENTS

I am very thankful to my advisors for valuable help and advice they fed me throughout these two years.

I am grateful to Stéphane Étienne for offering me the opportunity to expand my understanding of fluid-structure interaction and computational dynamics. It has been a great and rich experience to rediscover mechanics while coding.

I would like to thank Frédérick Gosselin for choosing me as his Masters student. His wise interpretations and critical reasoning impacted my scientific thinking; for his patience, kindness, and continuous uplifting I'm very indebted.

Many thanks go to Prof. Christopher Cameron from Université de Montréal for generously assigning time for interesting discussions about the biology of soft corals. Also it was a pleasure to follow him on a tour of his lab.

I sincerely acknowledge the financial support from NSERC Discovery Grants, as well as from the Génie Par Simulation (GPS) program. Among the GPS faculty I wish to express my gratitude to Prof. Dominique Pelletier who always encourages students and shows interest in their projects. He once, on his own initiative, helpfully handed me a monograph on numerical methods where I found the description of the particle tracer algorithm, a vital block that improved much my Python code. So I owe a large part of particle simulation results to him. Special thanks also to Dr. David Vidal for coordinating GPS workshops and seminars, and for being sympathetic and friendly with us.

I would not forget LM2 members, Stéphane's students, GPS fellows, office-mates, and everyone I met during my studies at Polytechnique Montréal who shared knowledge, identified code bugs, suggested ideas, or contributed in any way to this project. Thank you all.

RÉSUMÉ

Les coraux mous sont des espèces marines flexibles se déformant à l'effet des écoulements d'eau. Au passage d'une vague, alors que le tronc principal vacille, un mouvement particulier est observé: les branches se mettent à vibrer rapidement, avec de petits déplacements, et transversalement à la direction de l'écoulement. Dans ce mémoire, nous expliquons l'origine de ces vibrations et cherchons leur impact sur les coraux mous.

Le critère de Glauert-den Hartog étant invalidé pour une section de branche de corail idéalisée, et les fluctuations de l'écoulement d'eau de mer ayant une fréquence de pic assez petite, nous avançons que les vibrations induites par vortex (VIV) sont la cause la plus plausible du mouvement rapide des branches. Par ailleurs, le fait que les coraux mous soient des espèces se nourrissant en filtrant l'eau de ses particules comestibles, nous faisons l'hypothèse que ces vibrations peuvent influencer leur taux d'alimentation. À l'aide d'un code maison d'éléments finis d'interaction fluide-structure, en plus de scripts codés en Python, nous avons simulé les trajectoires de particules sphériques autour d'un cylindre circulaire, puis calculé le taux de capture. Nous avons trouvé que, lors de la synchronisation de fréquence, les cylindres vibrants capturent jusqu'à 40% plus de particules que ceux fixés. Ainsi, les VIV augmenteraient probablement le taux d'alimentation des coraux mous et leur offriraient une meilleure nutrition.

ABSTRACT

Soft corals are flexible marine species that deform when exposed to a flow of water. Under the action of a wave surge, while the stem sways back and forth at the low frequency of the wave, a yet unreported motion takes place: the branches vibrate at high frequency, with small amplitude, and transverse to the water flow. The goal of this thesis is twofold: to explain the origin of these vibrations, and to find their impact on soft corals.

Because the Glauert-den Hartog criterion is unfulfilled for an idealised coral branch, and since the peak frequencies of the seawater disturbance are too small, we consider vortex-induced vibrations (VIV) the only remaining probable cause of the observed rapid branch motion. Given that soft corals are sessile passive filter feeders that catch particles brought by currents, we hypothesise that these vibrations may affect their feeding rate. Using an in-house monolithic fluid-structure interaction (FSI) finite element solver along with a PYTHON code, we simulated trajectories of spherical particles around a circular cylinder and calculated the capture rate. We found that vibrating cylinders capture up to 40% more particles than fixed ones at lock-in. Thence, VIV plausibly increase the rate of food capture and offer soft corals better nutrition.

TABLE OF CONTENTS

LIST OF TABLES

LIST OF FIGURES

LIST OF SYMBOLS AND ACRONYMS

ALE	Arbitrary Lagrangian Eulerian
CFD	Computational Fluid Dynamics
DNS	Direct Numerical Simulation
IBM	Immersed Boundary Method
URANS	Unsteady Reynolds-averaged Navier-Stokes
VIV	Vortex-Induced Vibrations

m	cylinder mass
D	cylinder diameter
k	spring stiffness
ρ_f	fluid density
μ_f	fluid dynamic viscosity
ν_f	fluid kinematic viscosity
d_p	particle diameter
ρ_p	particle density
m_p	particle mass
$\boldsymbol{x}_\mathrm{p}$	particle centre position
$\boldsymbol{u}_\mathrm{p}$	particle centre velocity
$\boldsymbol{X}_\mathrm{cyl}$	cylinder centre position
M	cylinder mass number
ζ	damping ratio
$\boldsymbol{U}_\mathrm{f}$	flow velocity
$\boldsymbol{\chi}$	mesh displacement
$\boldsymbol{V}$	mesh velocity
p	pressure
f_v	vortex shedding frequency
f_n	natural frequency
St	Strouhal number
ρ^+	density ratio
Re	cylinder-based Reynolds number
Re_p	particle-based Reynolds number
R	diameter ratio
U_r	reduced velocity

α	angle of attack
$\boldsymbol{F}_{\mathrm{D}}$	drag
$\boldsymbol{F}_{\mathrm{P}}$	pressure load
$\boldsymbol{F}_{\mathrm{A}}$	added mass force
C_{L}	lift coefficient
C_{D}	drag coefficient
C_{m}	mass coefficient
$\dot{N}$	capture rate
η	capture efficiency/dimensionless capture rate
C_0	particle concentration
e	capture window length
θ_{c}	maximum angle of capture
δ	gain in capture rate
$Y_{\max}$	maximal transverse amplitude
$X_{\max}$	maximal stream-wise amplitude
γ	slenderness ratio
β	distortion coefficient
d_{cc}	counter-current distance
s	curvilinear coordinate
$\boldsymbol{t}$	tangential vector
$\boldsymbol{n}$	normal vector
$\boldsymbol{b}$	binormal vector
$\boldsymbol{\Omega}$	Darboux vector
$\boldsymbol{M}$	internal moment
$\boldsymbol{F}_{\mathrm{int}}$	internal stress
$\boldsymbol{f}_{\mathrm{ext}}$	external force
q	fluctuating lift variable
$\boldsymbol{w}$	rod displacement
EI	rod flexural rigidity
GJ	rod torsional rigidity
m_{l}	rod mass per unit length
Γ	rod aspect ratio
C_{Y}	rod Cauchy number
$\mathcal{R}$	reconfiguration number

LIST OF APPENDICES

CHAPTER 1 INTRODUCTION

In the very beginning of the *Flow-Induced Vibration* introduction, Robert D. Blevins portrays a gloomy, though realistic, situation of the damage fluid-induced instabilities engender to human constructions [15]. Engineers fear that fatigue and failure take upon bridges, stacks, power transmission lines, aircraft control surfaces, offshore structures, heat exchangers, and petroleum risers [16]. This constant apprehension about the presumed harmful vibrations, though, seems to be unique to humans, and absent in the living nature. Soft corals, such as the bipinnate sea plume *Antillogorgia bipinnata*, are found to live in peace with fluid-induced instabilities. Under a sea wave action, soft coral colonies deform, bend, and streamline with the flow, exhibiting a gentle back and forth swaying motion. Yet, as the flow speed peaks, the branches start to vibrate rapidly with low amplitude [17]. This unusual rapid motion is a mystery which has not been reported in the literature, at least to the extent of the content we looked into. Why do soft corals have this peculiar vibration? This plain question certainly holds a complex and intermingled answer from multiple scientific domains.

The vibrating soft coral constitutes a fluid-structure interaction (FSI) problem: it deals with a flexible structure (soft coral branches) within a fluid flow (water currents) that induces an excitation. The field of FSI flourished in the last century with a focus globally on industrial applications, and has recently found a place in the realm of the living nature [18, 19]. Studies on the streamlining of slender beams under steady currents [20], the swaying motion of thin plates in oscillatory flows [14, 21], and the modal shapes and frequencies of branching structure [22–24] furthered our understanding of the motion of slender species in land and sea. Soft corals dynamics display many of these features, but the rapid motion of the branches is still an intriguing element that we do not have a clear answer for. We intend to provide the scientific community a useful resource on the vibrational biomechanics of soft corals and similar biological organisms in general.

Thinking of soft coral branches as slender flexible cylinders, we have reasons to believe that vortex-induced vibrations might be implicated in this rapid motion. In fluid dynamics, vortices are a core element for understanding flows [25–27]; in nature, they are a key mechanism in the lives of species. There is evidence that black fly and mosquito larvae in water separate the flow with their body to create vortices and bring more food up to their fans [28, 29]. In terrestrial plants, when a raindrop splashes against spores in a leaf, a vortex ring appears and disperses them along farther places [30]. As for soft corals, since they feed upon particles brought by the water flow, the vibrations caused by vortices may have an impact on

food capture and nutrition. Biologists having long witnessed the role of hydrodynamics in the plasticity of soft corals [31, 32], hence fluid mechanics would bring a part of answer to their assumptions. We wish this thesis to bridge mechanics and biology, and that our results will offer biologists insight to help decipher unexplained, or even unexplored, phenomena associated with soft corals, and their relatives more broadly.

Moreover, the study of living systems to fulfill one's curiosity is not useless in itself, and might reveal series of inventions. In fact, "some of the highest achievements of the human mind in science [...] have indeed been curiosity-driven," asserted Michael P. Païdoussis in his *Fluid-Structure Interactions* [33]. Species have always found solutions to cope with natural constraints and preserve their existence. As engineers, it is then wise to pick these solutions and transpose them in concrete applications. We now witness a climbing trend on designing flexible beams and flapping flags profitting from instabilities to produce energy [34–38], bioinspired morphing blades for wind turbines to increase power efficiency [39], and underwater robotic fish to autonomously explore water environments [40]. We hope that mechanicians and engineers shall find in the vibrating soft coral problem a source of inspiration for industrial devices and energetics technologies, as well as a new paradigm for biomimetics applications.

1.1 Literature review

The literature review is threefold. First we dive into the basic biological concepts of soft corals. Then we present fluid-induced instabilities that usually take place in marine environment and could potentially give rise to the soft coral vibrations. Finally, we review the physics of filtering and particle collecting by stating theoretical, numerical, and experimental works.

1.1.1 Biology of soft corals

Definition and classification

Soft corals are marine species that belong to the class *Anthozoa*, together with stony corals and sea anemones [41] (Figure 1.1). They live attached to the sea bed, stuck to the same place. In biology, such species are known as benthic (living in the sea bed) and sessile (non-motile).

Species of the class *Anthozoa* are composed of a base unit organism called *polyp*, covering their entire body (Figure 1.2). The polyp is tubular, and has a mouth, a digestive system,

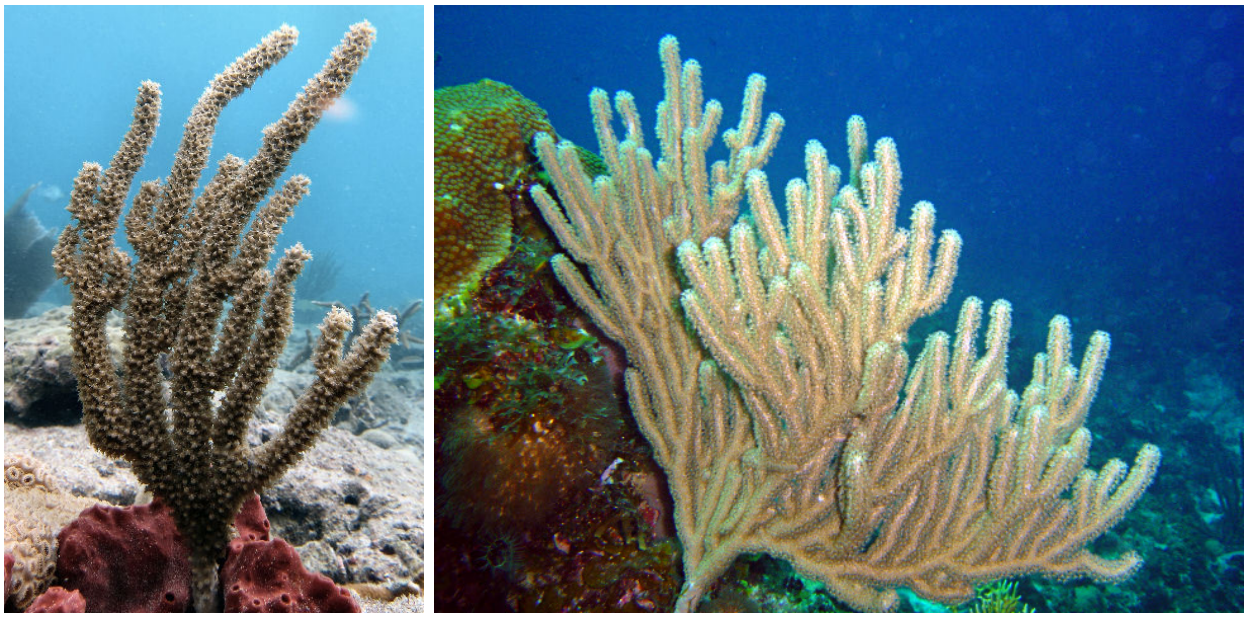

Figure 1.1 Examples of soft corals. Left: swollen knob candelabrum (*Eunicea mammosa*) [2]. Photo taken by © Charles G. Messing, reproduced with permission. Right: spiny sea rod (*Muricea elongata*) [3].

and tentacles [42]. In its early life, it starts as a (planula) larva, swimming in the sea until it hits a coral substrate and sticks to it. As it grows, it calcifies the region of contact, and fastens with the coral substrate. It becomes a *zooid*, a polyp that is henceforth an integral part of the coral [43].

A major subclass of *Anthozoa* is the group of corals with flexible skeleton: *Octocorallia*. They are commonly referred to as octocorals, and are named as such because they all have polyps with eight tentacles [42], as it could be noticed in Figure 1.2. Taxonomists distinguish three families of octocorals: the blue coral, of order *Helioporacea* (8 species), sea pens of order *Pennatulacea* (232 species), and soft corals and gorgonians (also called sea fans, rods, and whips) of order *Alcyonacea*. This latter order is the main representative of octocorals with more than 3400 species [44]. Old classifications emphasised the difference between soft corals and gorgonians [45], because soft corals do not have an internal structure, contrary to gorgonians. Yet, recent classifications have faded the boundaries between these two categories as the number of discoveries of species in *Alcyonacea* has been accumulating [42]. In this thesis we shall, accordingly, term all species of *Octocorallia* 'soft corals' (except if the difference is intended), for we consider softness, or structurally speaking *flexibility*, the main biological property of interest in the ensuing mechanical investigation.

Figure 1.2 Close up picture of polyps covering a sea fan. They have eight tentacles, each of them deploying pairs of nematocysts (stinging cells) opposite to each other [4] (Photo credits © Jurgen Freund, with permission).

Nutrition

Soft corals are *passive filter feeders*. Like other sessile species, they wait *passively* for water currents to *filter* their particulate nutritional content with their polyps. They require nitrogen and phosphate components for proper growth [43]. Example of food particles that soft corals feed upon are detritus and dissolved organic matter, phytoplankton (microalgae), protists (e.g. dinoflagellates), larvae (e.g. nauplii), copepods, and small zooplankton ($\sim 300\ \mu$m) [46].

The feeding process comprises four phases. When an edible particle comes close to the polyps, tentacles stretch and catch it (encounter phase). To keep the particle retained, corals usually activate their spines to pierce and neutralise it, or secrete adhesive mucous substance to retain it (retention phase). A successive encounter and retention event is referred to by the term 'capture'. The next step is to bring the particle down to the polyp's mouth (handling phase), then ingest it (ingestion phase) [47].

If a coral relies entirely on ingested food, it is called *heterotrophic*. Conversely, *phototrophic* corals carry in their tissue zooxanthellae [43], green microalgae symbionts, and photosynthesise their own organic compounds from light. Finally, *mixotrophic* corals benefit from both feeding modes alike [42]. In the West Indies, although most soft corals are mixotrophic, they do not always make profit of the two feeding modes. For instance, soft corals of deep waters receive hardly any light, hence do not rely much on photosynthesis. This is also the case

for soft corals in turbid waters, because of suspended sand and other fine granular matter screening light.

Besides, being mixotrophic is a powerful asset that soft corals possess, because they can shift from one feeding mode to the other if some external stress impinges on their habitat. In the San Blas achipelago, Panama, Baker [48] transplanted (scleractinian) corals of deep waters into shallow-water sites. He found that corals regulated their microalgae distribution to fit the light abundance in their new location. This response of the soft coral is known as biological *plasticity*.

Plasticity

As their names suggest, soft corals have diverse morphologies (i.e. forms and shapes), from long straight tubes (sea whips) to bushy structures (sea plumes) and flat sieves (sea fans). This diversity continues even within the same species relative to their habitat. For example, the species *Antillogorgia bipinnata* in deep waters has longer branches and larger polyps than its counterpart in shallow waters [49]. Cadena and Sanchez [50] propose that having long branches would help deep-water corals get as close as possible to the sea surface and benefit from light, as well as reach higher food concentration above the boundary layer. By this mean, soft corals are *plastic* because they are able to *acclimatise* to their surrounding environment, i.e. change their morphology into a more suitable one [51, 52].

As another manifestation of plasticity, Wainwright and Dillon [31] measured the orientation of sea fans *Gorgonia ventilana* and *Gorgonia flabellum* while growing (Figure 1.3). They pointed out that these corals have a preferred growth direction, perpendicular to the local speed. By facing the water current and exposing a larger area, sea fans maximise the number of particles intercepted, hence sieve food better [32]. Furthermore, Jeyasuria and Lewis [53] measured the Young's modulus of several soft corals, and found that deep water species are stiffer than those of shallow waters. In fact, in waters with permanent turmoil and disturbance, flexibility is a valuable property for soft corals because it allows deformation and reconfiguration, hence reducing hydrodynamic drag [54]. Multiplying branches and promoting a bushy structure is also a survival strategy that deep-water corals seek when transplanted in shallow waters [55].

While soft corals show plastic ability to get accustomed to their local environmental conditions, they cannot stand the increase of temperature, water acidity, and many other negative changes in climate that humans have brought about due to intense maritime transport, chemical spills, and agricultural runoffs, to name but a few [56].

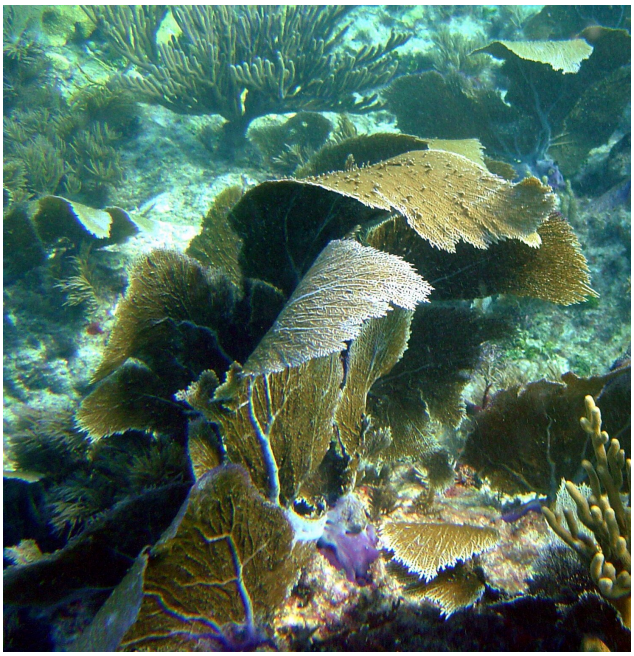

Figure 1.3 Sea fans facing the direction of the water current [5]

Benefits, threats, and glimmer of hope

Corals have a primordial role in the marine ecosystem. They offer shelter and home to several benthic species (e.g. small fish, urchins, lobsters, worms, etc.) [57]. They also protect coastal areas from natural disasters. For instance, coral reefs deflect the direction of tsunami waves and absorb their energy, hence reduce their height [58]. Economically, they provide regions with substantial income through many goods and services such as tourism, shoreline protection, and fisheries. In 2003, the annual net benefits, from these three activities combined, totalled $\sim$ \$30 billions (US\$, 2010) [59]. Unfortunately, many of these advantages are fading away because of the heavy loss and damaging of coral reefs.

Corals rely entirely on the surrounding water to adjust their body temperature (*poikilothermic* organisms) [43]. Being sensitive to temperature changes, corals bleach under a thermal stress, i.e. lose their zooxanthellae and become white and pale [60]. Figure 1.4 shows bleaching of a part of a soft coral. A temperature increase (or decrease) as faint as $1-2$°C above (or below) usual temperature extrema in tropical oceans may spark hot (cold) water bleaching [61]. Coral bleaching is all the more alarming in regions where the water stagnates and conserves heat (e.g. 'Give Up' reefs [62]).

Additionally, as the ocean absorbs more and more emitted greenhouse gases and acidifies, corals might face growth disturbances. The calcification rates of corals would drop down

Figure 1.4 A bleaching soft coral (*Sinularia polydactyla*) (reproduced from [6])

by 57% if the concentration of carbon dioxide (CO_2) doubles, and by 85% if it triples [63]. With this shortage in production of the main component of coral skeletons they become shorter, hence cannot protect themselves from outside endeavours anymore (e.g. predators, storms [43, 64]).

Finally, curio dealing, poaching, and overharvesting spare not the coral fauna. Soft corals like the organ pipe coral *Tubipora musica* and blue coral *Heliopora coerulea* have their charm exploited for jewelry and ornament commerce, in a complete violation of the Convention on International Trade in Endangered Species (CITES) [42].

These factors have put nearly 75% of the world's coral reefs under threat [65]. Yet, within this ecological crisis, many actions have been taken to protect reefs and preserve marine ecology. A rewarding step has been to establish Marine Protected Areas (MPAs), which are regions restricting destructive activities, hence promoting biodiversity and aquatic prosperity. By 2011, there were 2679 MPAs covering 27% of the coral reefs around the globe [65]. Local communities and social actors also provide a sustainable framework and healthy reef use through the creation of Locally Managed Marine Areas (LMMAs). Last but not least, some researchers think about coral farming as a worthwhile solution to regain impaired reefs [66]. Cultivating corals *ex situ* and transplanting them in the ocean would further reef restoration and recover the ecological balance. In order to implement an adequate coral farming, it is necessary to understand the biological and physical properties for coral growth and survival. Thus, we propose in this project to examine how hydrodynamics and soft coral structure combine to ensure optimal food particle interception, hence an appropriate growth.

1.1.2 Flow-induced vibrations

A flexible structure is susceptible to vibrate when a fluid flow crosses over it. The resulting interactions have been well identified, and large amounts of data have been collected [67]. Though, given the variety of flow conditions and body shapes, it is important to gather interactions under categories sharing similar mechanical features, so that engineers can profit from the prior knowledge when tackling a new problem. Naudascher and Rockwell [1] came with a methodology to assess a flow-induced vibration, summarised in Table 1.1. One should first pinpoint body and fluid oscillators. A flexible structure, or flexibly-mounted rigid structure, are both examples of body oscillators; gravity waves or acoustic signals that represent fluid oscillators. After that, the resulting vibration is classified into three categories based on the source of excitation. If the upstream flow has fluctuating velocities or pressure, the vibration is an extraneously-induced excitation (EIE). If a fluid instability drives the body oscillations (e.g. Bénard-von Kármán instability, which forms vortices in the wake), then the motion is an instability-induced excitation (IIE). Finally, if the fluid-dynamic forces on the body grow while it oscillates, the motion is self-excited and classified as a movement-induced excitation (MIE). Because of their complexity, some fluid-structure interactions may involve both fluid and body oscillators, as well as two or three types of excitation altogether [1].

excitation	oscillator	
	body	fluid
EIE	turbulence buffeting	acoustic noise
IIE	vortex shedding	impinging shear layer
MIE	flutter	oscillating shock front

Table 1.1 Classification proposed by Naudascher and Rockwell [1]. After identifying the oscillator (body, fluid, or both), the motion is either an extraneously-induced excitation (EIE), an instability-induced excitation (IIE), a movement-induced excitation (MIE), or a mix of them (inspired from [1]).

Extraneously-induced excitation

If a surface wave is regular (i.e. has a specific frequency) and passes over a structure, this latter sways with the same frequency. In reality, though, the sea surface elevation is irregular and comprises a wide range of frequencies. In response to this spectrum of surface waves, the structure buffets, hence the resulting motion is classified as an extraneously-induced excitation [1]. More generally, the power density spectrum also depends on the direction of a surface wave, in addition to its frequency.

Each region in the ocean has a specific spectral density (of surface elevation). The most popular models that reliably describe spectral densities are the Pierson-Moskowitz and the Joint North Sea Wave Project (JONSWAP) spectra [68]. The Pierson-Moskowitz spectrum is general for fully developed wind seas, and has a peak frequency f_{peak} inversely proportional to the wind speed U_{w} [69]

$$f_{\text{peak}} = 0.14\frac{g}{U_{\text{w}}}, \tag{1.1}$$

where g is the gravitational acceleration. The JONSWAP spectrum extends the Pierson-Moskowitz spectrum and fits the measurements in the North Sea [70]. Its peak frequency is

$$f_{\text{peak}} = \left(\frac{gx_{\text{f}}}{U_{\text{w}}^2}\right)^{-0.33}\frac{g}{U_{\text{w}}}, \tag{1.2}$$

where x_{f} is the fetch of the blowing wind. These models are also adopted in the West Indies, especially under hurricanes. Esquivel-Trava *et al.* [71] measured the spectral densities under 14 hurricanes in the Caribbean Sea and the Gulf of Mexico, in different directions, and found that the Pierson-Moskowitz spectrum fitted the best their measurements, with a peak frequency f_{peak} between 0.1 and 0.2 Hz.

Movement-induced excitation

Galloping is a movement-induced instability that arises for short bluff, non-circular (e.g. prismatic, with sharp angles) bodies, such as bridge decks and iced electric wire conductors [1, 67]. The frequency of motion is usually slow, and the body oscillates with large displacements. If the body put under the flow has lift and drag coefficients C_{L} and C_{D} changing with the angle of attack α, the quasi-steady state theory states that once

$$\frac{\mathrm{d}C_{\text{L}}}{\mathrm{d}\alpha} + C_{\text{D}} < 0, \tag{1.3}$$

galloping arises. Inequality (1.3) is known as the Glauert-den Hartog criterion.

The fluidelastic instability is another movement-induced excitation appearing if structures are arranged close to each other, perpendicular to the flow. Two cylinders put side-by-side have a combined vortex shedding if the centre-to-centre separation space is less than 1.4 diameters [15]. If the separation space is between 2 and 3 diameters, they have a bistable asymmetric shedding, and between 3 and 4 the vortex shedding becomes coupled. These situations generate synchronised vibration that causes relatively important displacements [72]. A separation space above $\gtrsim 4$ have no effect on the cylinders, and each of them observes an independent vortex shedding [15].

Instability-induced excitation: Vortex-induced vibrations

If fluid particles rotate around a common centre, the motion is said to have a vortex motion [25]. The vorticity is the measure of the angular velocity in the fluid. It is always present in real fluids around a body, because fluid particles adhere to the body surface and shear with those moving close to them, creating a velocity gradient (hence vorticity). When the Reynolds number Re is small, no vortex appears even with a non-zero vorticity. As the Reynolds number increases, two whirls (vortices) rotating in opposite directions form a recirculation region in the rear of the body [73]. This whirling zone oscillates starting from $Re \approx 20$ [74], and breaks into vortices that are shed periodically beyond $Re \approx 47$, forming the *von Kármán vortex street* [15]. Between $Re = 47 - 150$, the von Kármán vortex shedding is laminar, as pictured in Figure 1.5, and becomes slightly turbulent above $Re \approx 150$ [15]. At $Re \approx 180 - 194$ vortices deform spanwise and transition into a three-dimensional shedding [73, 75].

Vortices are shed periodically with a frequency f_v proportional to the upstream flow velocity U_0 and to the inverse of the characteristic length of the object D. The constant of proportionality is the Strouhal number

$$St = \frac{f_\mathrm{v} D}{U_0}, \tag{1.4}$$

which depends on the Reynolds number. The lift applied on the body is subsequently periodic, pushing the body upwards and downwards, which results, if the body is elastic, in *vortex-induced vibrations* (VIV). From this perspective, VIV are classified as an instability-induced excitation according to Naudascher and Rockwell [1].

Vortex-induced vibrations have received extensive amount of research. Among the earliest inquiries into the link between the vortex shedding and body motion were the experiments

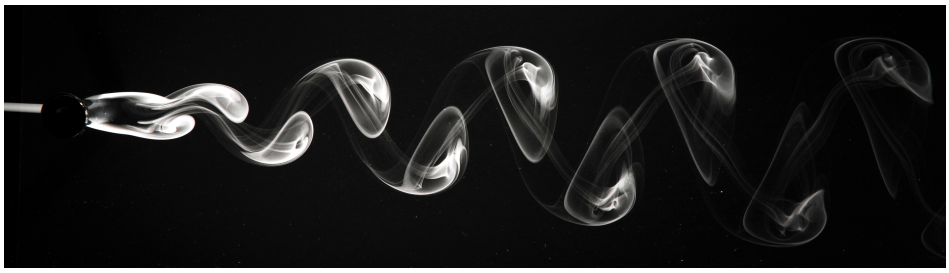

Figure 1.5 Pathlines showing a von Kármán vortex street in the wake of a fixed circular cylinder [7].

of Bishop and Hassan [67, 76], in which they forced a circular cylinder to vibrate at an imposed frequency f. They found that when f approaches the vortex shedding frequency f_v, the body and wake oscillations synchronise, and the hydrodynamic forces amplify, in a comparable manner with a harmonic oscillator [76]. They coined this phenomenon *lock-in*. Feng reported the same amplification in the transverse span and phase angle of a cross-flow restricted motion of circular and D-shaped cylinders [77]. The largest amplitudes are obtained for the lowest products $M\zeta$ of the mass number of the body M and the damping ratio ζ [78].

At lock-in, the shedding frequency sticks to the natural frequency of the body $f_\mathrm{v} \approx f_\mathrm{n}$, and the Strouhal number becomes equal to the inverse of the reduced velocity, defined as

$$U_\mathrm{r} = \frac{U_0}{f_\mathrm{n} D} \quad \left(\approx \frac{1}{St} \quad \text{at lock-in} \right). \tag{1.5}$$

Since $St \sim 0.15 - 0.20$ for circular cylinders at moderate Reynolds numbers [79], the lock-in happens at reduced velocities of $U_\mathrm{r} \sim 5 - 7$.

Unlike rigid structures, flexible cylinders with multiple natural frequencies have each of their modes peaking for a range of critical reduced velocities. Tensioned cables can have as many excited modes as 8 for the cross-flow vibration and 12 for the in-line vibration [80]. If they are slender enough, they exhibit travelling waves when they have free endpoints, and standing waves when they have pinned endpoints [81, 82]. A complex mixture of these wave propagation manners occurs when a finite flexible structure is put under a shear flow [83]. A flexible cantilever, on the other hand, observes a second large tip amplitude for $U_\mathrm{r} \sim 20$ [84], and the more it bends, the larger the excitation range of reduced velocities it exhibits [85].

Phenomenological models of VIV are important in applications, since they display the main fluid-structure dynamics as in real experiments and numerical simulations with much lower cost, and equally importantly, unveil the fundamental aspects of this instability. According to the classification of Païdoussis *et al.* [67], the types of VIV models are (i) forced system models, (ii) fluidelatic system models, and (iii) coupled system models. In the first type, the lift F_L is harmonic and forces the motion of the body under the vortex shedding frequency

$$F_\mathrm{L} = \frac{1}{2} \rho_\mathrm{f} U_0^2 D C_\mathrm{L} \sin\left(2\pi f_\mathrm{v} t\right), \tag{1.6}$$

with the lift coefficient C_L being constant, proportional to the amplitude of the measured fluctuating lift coefficient. If we denote by y the transverse displacement of the solid, the

forced system model reads

$$(m_\mathrm{s} + m_\mathrm{f})\ddot{y} + (r_\mathrm{s} + r_\mathrm{f})\dot{y} + h_\mathrm{s} y = F_\mathrm{L}, \tag{1.7}$$

with m being the mass, r the damping, h the stiffness, and the subscripts $(.)_\mathrm{s}$ and $(.)_\mathrm{f}$ referring to the solid and the fluid respectively.

Beyond the forced system models, fluidelastic models consider a lift varying with the solid motion through either global parameters (e.g. maximum amplitude $A = \max_t y(t)$, reduced velocity U_r) or local, temporal variables (e.g. vertical displacement y and its temporal derivatives $\dot{y}$ and $\ddot{y}$).

These previous models are restricted to harmonic oscillations and do not illustrate how wake dynamics evolve and act upon the body [67]. The coupled system models rectify this limitation and take the lift force as an unknown, coupled with the equation of the solid motion. The basis of this idea came from the work of Bishop and Hassan who hinted that the hydrodynamic load behaves as a 'non-linear self-excited fluid oscillator' [76]. An appropriate model for the lift coefficient C_L in expression (1.6) is the van der Pol equation [86]

$$\ddot{C}_\mathrm{L} + \varepsilon(2\pi f_\mathrm{v})(C_\mathrm{L}^2 - 1)\dot{C}_\mathrm{L} + (2\pi f_\mathrm{v})^2 C_\mathrm{L} = G. \tag{1.8}$$

The van der Pol equation guarantees a lift coefficient growing when it has small values (negative damping $C_\mathrm{L}^2 - 1 < 0$), and stabilising when its has large values (positive damping $C_\mathrm{L}^2 - 1 > 0$) [87]. After a duration (short when ε is large), the wake motion reaches a *limit-cycle* that depends only on the constants of the equation (1.8), whatsoever the initial condition of C_L.

The choice of the right-hand side function G of the equation (1.8) has been controversial throughout decades. Hartlen and Currie were the first to suggest that G is proportional to the transverse velocity [88]

$$G \propto \dot{y}. \tag{1.9}$$

The solution of this coupled system succeeded in reproducing the lock-in phenomenon and the limit-cycle of the vertical amplitude, yet the reason of this choice lacks a sound physical foundation [67]. This idea was put to test and discussed in the work of Facchinetti *et al.* [89] (Figure 1.6, left), who showed that a coupling proportional to the transverse acceleration

$$G \propto \ddot{y} \tag{1.10}$$

transposes more faithfully the real motion of a cylinder under VIV. The wake oscillator

model of Facchinetti *et al.* has received interest in many applications like infinite flexible cylinders [8, 34], slender cables under non-uniform flow [90, 91], and clamped beams bent under drag [85].

Finally, there are models, known as Birkhoff wake oscillators, that stem from the dynamics of the recirculation zone behind the solid, which swings up and down over a period, causing the vibration of the body [92, 93]. Birkhoff oscillators replace the fluctuating lift coefficient in equations (1.7) and (1.8) by the fluctuating rotation angle α of the wake. A possible coupling with the van der Pol oscillator is through the transverse acceleration $G \propto \ddot{y}$, as in the model of Nakamura [94,95]. The model of Tamura (Figure 1.6, right), on the other hand, assumes that the length of the recirculating region changes in time, and derives a coupling term proportional to the velocity and acceleration $G = -a\ddot{y} - b\dot{y}$ [9,96]. The dynamics found using this latter coupling showed several features of VIV, matched experimental results [93], and was extended to square cylinders [97] and flexible circular cylinders [98].

Vortex-induced vibrations have been an everyday challenge to engineers. The oil industry fears the failure of risers in offshore drilling sites, tall chimney stacks are prone to toppling down, and many human constructions are under the threat of vibrations. Engineers proposed a plethora of techniques to control and attenuate, if not suppress, these vibrations: structure stiffening, strakes, shrouds, slats, ribbons [15], and even corrugated cylinders inspired from harbor seal whiskers [99]. Yet, some recent trends have flipped the dark view of this instability, and favourably harnessed the potential of VIV into beneficial applications such as energy harvesting [34–37]. The topic of the present thesis falls within the same optimistic scope, and we will see that triggering VIV might be an essential strategy for soft corals to boost the number of edible particle interception, thence ensure a better nutrition.

1.1.3 Particle capture

In order to feed, coral polyps must encounter an edible particle, retain it, handle it to the mouth, and ingest it [47] (see section 1.1.1). The capture phase (i.e. encounter + retention) has been the main interest of many researchers in the mechanical and chemical fields, because it deals with the motion of particulate matter in a flowing fluid, and have applications related to the capture and sieving of dust, pollutants, or colloids. In the present mechanical context, we will consider the terms 'capture' and 'interception' as synonyms of 'encounter', since we assume that particles are retained as soon as they encounter an obstacle. We will also make abstraction of the coral branch and polyps in particular, and consider a generic collector with a circular cross-section of diameter D (i.e. circular cylinder) within a flow of an upstream speed U_0. Denoting the size and density of the particle as d_p and ρ_p, and the fluid density and

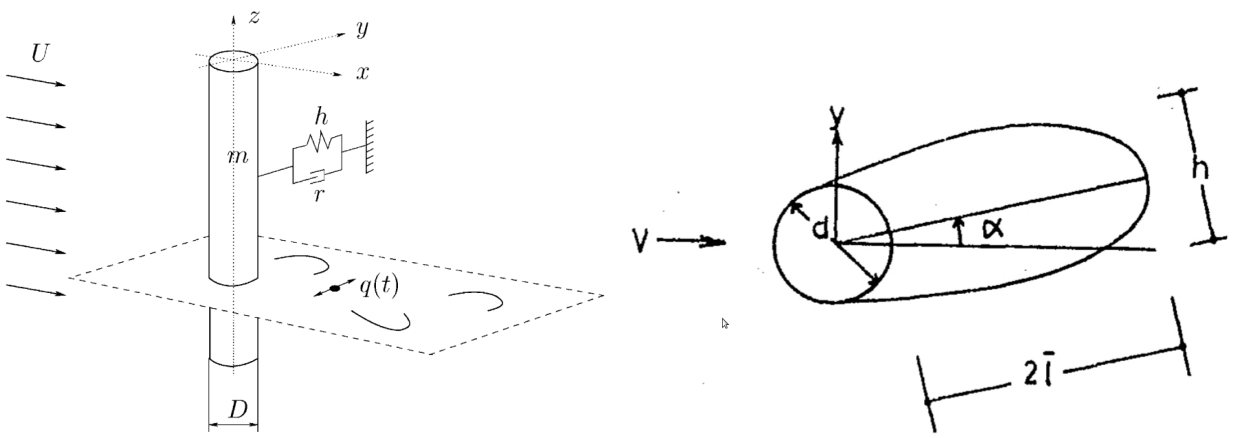

Figure 1.6 Schematics of the models of Facchinetti *et al.* (left) and Tamura (right) (reproduced from [8] and [9], with permission).

dynamic viscosity as ρ_f and μ_f, the important parameters associated with particle capture are the ratio of densities, ratio of diameters, and the collector-based Reynolds number

$$\rho^+ = \frac{\rho_\mathrm{p}}{\rho_\mathrm{f}}, \quad R = \frac{d_\mathrm{p}}{D}, \quad Re = \frac{\rho_\mathrm{f} U_0 D}{\mu_\mathrm{f}}. \tag{1.11}$$

Capture mechanisms

According to Rubenstein and Koehl [100], the capture mechanisms are categorised into (i) direct interception, (ii) inertial impaction, (iii) gravitational deposition, (iv) diffusional or motile-particle deposition, and (v) electrostatic attraction.

A particle is directly intercepted when it hits the cylinder after ideally following exactly a flow streamline, which is usually the case for massless particles. A dimensionless index assessing the intensity of such a capture mode is

$$N_\mathrm{DI} = \frac{d_\mathrm{p}}{D} \, (= R) \,, \tag{1.12}$$

If a particle carries important inertia, however, it tends to deviate from the flow streamlines, especially if they curve close to the collector. Rubenstein and Koehl propose the index

$$N_\mathrm{I} = \frac{(\rho_\mathrm{p} - \rho_\mathrm{f}) d_\mathrm{p}^2 U_0}{18 \mu_\mathrm{f} D} = \frac{1}{18} (\rho^+ - 1) R^2 Re. \tag{1.13}$$

The gravitational capture mode is similar to the inertial impaction, the particle velocity being here the settling velocity. Finally, diffusional deposition concerns small particles subject to

Brownian motion, as well as motile, swimming particles that actively change their direction relative to the flow. The intensity for both types is estimated with the following dimensionless index

$$N_{\mathrm{M}} = \frac{\mathcal{D}}{U_0 D}, \tag{1.14}$$

where the diffusional coefficient $\mathcal{D}$ is given by the Stokes-Einstein formula

$$\mathcal{D} = \frac{kT}{3\pi\mu_{\mathrm{f}} d_{\mathrm{p}}}, \tag{1.15}$$

with k the Boltzmann constant and T the ambient temperature. The electrostatic attraction is like the diffusional deposition, and happens if the particle and collector have opposite electric charges.

Capture efficiency

Consider a cylindrical collector in uniform flow as illustrated in Figure 1.7. The collector is deemed efficient if it intercepts a considerable number of particles over a certain duration. The measure of the collector quality is the capture efficiency, denoted usually as η. When N_{init} particles are initially released, from the same starting line upstream from the collector, η is expressed as [10]

$$\eta = \frac{N}{N_{\mathrm{init}}}, \tag{1.16}$$

with N the number of captured particles. This definition gives the fraction of particle that the collector intercepts, but does not tell from where they were released. In fact, particles launched sparsely would be dispersed relatively far from the collector and result in few interceptions, whereas the same set of particles launched very close to the horizontal streamline would stay concentrated relatively near the collector and result in more interceptions. In two-dimensional problems, a finer definition of η accounting for the release span is given by [13, 101]

$$\eta = \frac{\dot{N}}{C_0 U_0 D}, \tag{1.17}$$

where $\dot{N}$ is the rate of capture (#/s) and C_0 the particle concentration in the fluid (per unit length, $\#/\mathrm{m}^2$). The denominator $\dot{N}_{\mathrm{init}} = C_0 U_0 D$ represents the rate at which particles are released, upstream from the collector, from a release window of length D. By analogy, if the window from which the captured particles are released has a length of e (see Figure 1.7), we have $\dot{N} = C_0 U_0 e$, hence the efficiency becomes [11, 12]

$$\eta = \frac{e}{D}. \tag{1.18}$$

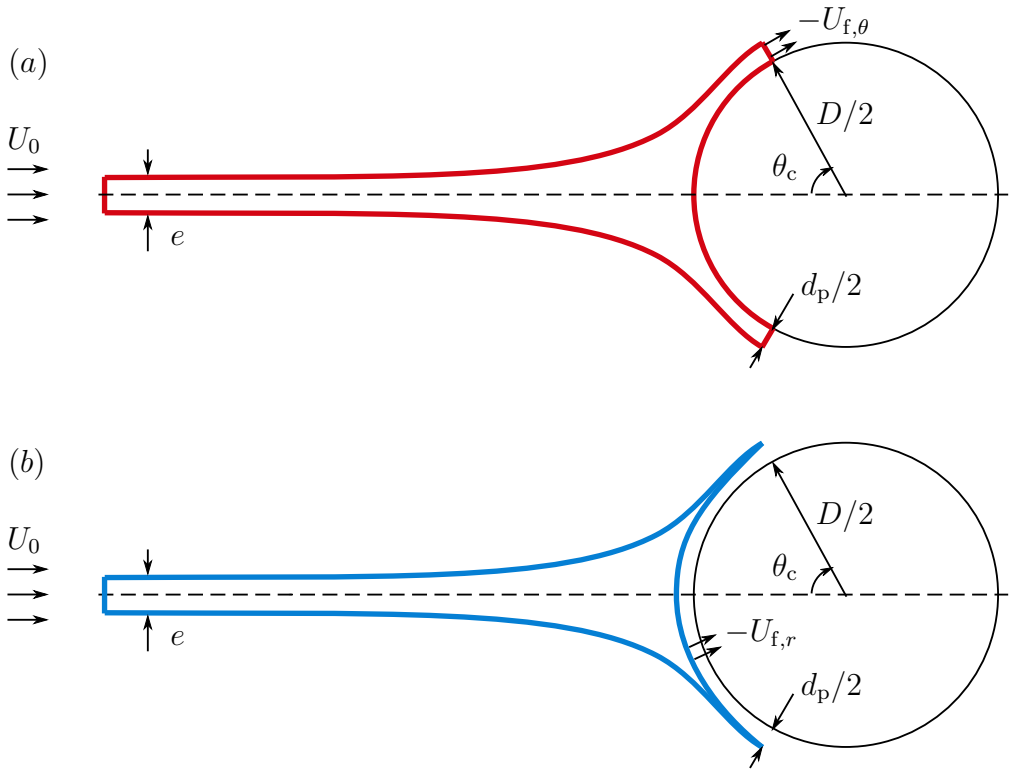

Figure 1.7 Control volumes used by (*a*) Haugen and Kragset [10] and Espinosa-Gayosso *et al.* [11,12] and (*b*) Weber and Paddock [13]. Particles that are ultimately captured enter from the window of length e. The outermost captured particle hits the cylinder at the maximum angle of capture θ_c. The radial and angular components of the fluid velocity are denoted $U_{\mathrm{f},r}$ and $U_{\mathrm{f},\theta}$.

Therefore, the calculation of the capture efficiency is possible without the knowledge of the initial number of particles, and requires only the length of what we call the *capture window*.

Influence of diameter ratio and Reynolds number

The above definitions led to the study of capture from different perspectives. Experimentally, Palmer *et al.* [101] counted the number of intercepted particles advected by a water flow around a fixed rigid cylinder, and found that the capture efficiency, as defined in (1.17), increases with the diameter ratio and Reynolds number according to the following power law

$$\eta = 0.224 Re^{0.718} R^{2.08}. \tag{1.19}$$

The majority of the particles were captured at the front side of the cylinder, over an angular extension of $\pm 50°$, whereas only 5% of them were found at the rear for high Reynolds numbers.

Haugen and Kragset [10] reproduced the numerical version of Palmer *et al.* experiments. They simulated the flow around a cylinder with The Pencil Code [102] using the immersed boundary method (IBM). They waited until the von Kármán vortex street establishes, then spread the particles from a centred slot of a size of the collector diameter. These particles were spheres undergoing only the hydrodynamic drag

$$\boldsymbol{F}_{\mathrm{D}} = -\frac{1}{2}\frac{C_{\mathrm{D}}}{C_{\mathrm{c}}}\rho_{\mathrm{f}}\pi\left(\frac{d_{\mathrm{p}}}{2}\right)^2 ||\boldsymbol{u}_{\mathrm{p}} - \boldsymbol{U}_{\mathrm{f}}||\,(\boldsymbol{u}_{\mathrm{p}} - \boldsymbol{U}_{\mathrm{f}}); \tag{1.20}$$

where $\boldsymbol{u}_{\mathrm{p}}$ is the particle velocity, and $\boldsymbol{U}_{\mathrm{f}}$ the local velocity of the flow field at the centre of the particle. They used the Schiller-Nauman interpolation of the drag coefficient C_{D} [103], and corrected the force with the Stokes-Cunningham factor C_{c} because of the noncontinuum aspects appearing when dealing with very small particles. The calculation of the capture efficiency from relation (1.16) indicated a power law as in equation (1.19)

$$\eta \sim Re^{0.7} R^2, \tag{1.21}$$

and found no particle intercepted on the rear for $Re = 20 - 200$, in agreement with the experiments of Palmer *et al.* [101].

Unlike the two previous studies, Espinosa-Gayosso *et al.* [12] calculated the capture efficiency from (1.18) without simulating any particle advection. Assuming neutrally buoyant particles do not cross streamlines, they calculated the (time-averaged) length e of the capture window from a balance equation by virtue of mass conservation in the control volume represented in

Figure 1.7(a)

$$\eta = \frac{e}{D} = \frac{2}{U_0 D} \int_{D/2}^{D/2+d_\mathrm{p}/2} -U_{\mathrm{f},\theta}(r,\theta)|_{\theta_\mathrm{c}} \mathrm{d}r, \tag{1.22}$$

with $U_{\mathrm{f},\theta}$ being the angular component of the fluid velocity. The angle θ_c is where the farthest captured particle hits the cylinder, and is defined implicitly through [12]

$$U_{\mathrm{f},r}(r,\theta)|_{D/2+d_\mathrm{p}/2,\theta_\mathrm{c}} = 0, \tag{1.23}$$

with $U_{\mathrm{f},r}$ being the radial component of the fluid velocity. For $Re \lesssim 180$ they ran two-dimensional DNS, using OpenFOAM [104], because the vortex shedding stays parallel to the main flow direction [75] (see section 1.1.2). Beyond $Re = 180$, they shifted to three-dimensional simulations for a realistic calculation of η. They indicated that the quadratic variation in the diameter ratio $\eta \sim R^2$ was valid only for small particles ($R \lesssim 0.05$), and overestimating the capture rate for large particles. However, the power law in the Reynolds number depended on the flow regime. When vortices appear ($Re \approx 47$) they found $\eta \sim Re^{0.7}$ as in Palmer *et al.* [101]. Nonetheless, for $50 < Re < 180$, the exponent 0.7 decreased down to ~ 0.65. Switching into three-dimensional DNS, they found that the exponent was slightly smaller than 0.5 in the entire range $180 < Re < 1000$. Had they continued with two-dimensional DNS, the exponent would keep a value around 0.6-0.65. Haugen and Kragset [10] used the same integral formula in (1.22), but, approximating the angular velocity $U_{\mathrm{f},\theta}$ using boundary theory considerations, they analytically derived a power law $\eta \sim Re^{0.5}$, in contradiction with their numerical data. Haugen and Kragset [10] thought this discrepancy came from the steady flow assumption when obtaining the integral form (1.22). Now the power $\sim Re^{0.7}$ turns out to be understandable since they kept two-dimensional computation for high Reynolds flows. Espinosa-Gayosso *et al.* [12] concluded that three-dimensional simulations are the right way to evaluate the capture efficiency above $Re = 180$.

Regarding low-Re flows, Espinosa-Gayosso *et al.* [11] proposed to work with the stream function through

$$U_{\mathrm{f},r} = \frac{1}{r}\frac{\partial \psi}{\partial \theta}, \quad U_{\mathrm{f},\theta} = -\frac{\partial \psi}{\partial r}. \tag{1.24}$$

Since $\psi = 0$ at the cylinder edge $r = D/2$ (no-slip condition), they replaced (1.24) in (1.22) and got

$$\eta = \frac{2\psi\left(D/2 + d_\mathrm{p}/2, \theta_{\mathrm{c}0}\right)}{U_0 D}. \tag{1.25}$$

Here $\theta_{\mathrm{c}0}$ is the maximum angle of capture for a vanishing particle size, $\theta_{\mathrm{c}0} = \lim_{d_\mathrm{p}\to 0} \theta_\mathrm{c}$.

Instead of the implicit equation (1.23), they suggested a new definition of θ_{c0}

$$\left.\frac{\partial^2 U_{f,r}}{\partial r^2}\right|_{D/2,\theta_{c0}} = 0. \tag{1.26}$$

Espinosa-Gayosso *et al.* [11] followed a theoretical-numerical hybrid approach to calculate η. They took the asymptotic expression of the stream function including inertial effects that Skinner [105] proposed using perturbation methods

$$\begin{aligned}\psi = {} & a(\Delta)\left(r\ln r - \frac{r}{2} + \frac{1}{2r}\right) \\ & + \frac{Re}{2}\left[\frac{a^2(\Delta)}{32}\left(2r^2\ln^2 r - r^2\ln r + \frac{r^2}{4} - \frac{1}{4r^2}\right) + \frac{b(\Delta)}{8}\left(r^2 - 2 + \frac{1}{r^2}\right)\right]\sin 2\theta\end{aligned} \tag{1.27}$$

where $\tilde{r} = r/(D/2)$, and a and b are respectively odd third and first order polynomials in the variable

$$\Delta = \frac{1}{1/2 - \gamma - \ln Re/8}, \tag{1.28}$$

with $\gamma = 0.577215...$ the Euler-Mascheroni constant. Rather than using the approximate polynomial expression of a and b, they numerically calculated them by fitting the equation (1.27) to their DNS solution. The curve of the efficiency for $Re < 47$ was best approximated by

$$\eta = \frac{1}{2.002 - \ln Re + f(Re)}\ \frac{R^2}{(1+R)^{k(Re)}}, \tag{1.29}$$

with

$$f(Re) = 0.953\ln(6.25 + Re) - 1.62, \tag{1.30}$$

$$k(Re) = 0.872\ln(19.1 + Re) - 1.92. \tag{1.31}$$

Notice that the quadratic variation of η in the diameter ratio is still valid for viscous flows since

$$\frac{R^2}{(1+R)^{k(Re)}} \approx R^2 \quad \text{for } R \leq 0.05 \text{ and } Re \leq 10. \tag{1.32}$$

The idea of expressing the capture efficiency with the stream function was presented back to the paper of Weber and Paddock [13]. Using (1.24), they obtained the same equation (1.25), though with a different control volume represented in Figure 1.7(b)

$$\eta = \frac{2}{U_0 D}\int_0^{\theta_c} -(D/2 + d_p/2)U_{f,r}(r,\theta)|_{D/2+d_p/2}\mathrm{d}\theta = \frac{2\psi\left(D/2 + d_p/2, \theta_c\right)}{U_0 D}. \tag{1.33}$$

The maximum angle of capture θ_c is defined here from the following condition

$$U_{f,r} < 0 \quad \text{for } \theta \in (-\theta_c, \theta_c). \tag{1.34}$$

Because the particles are assumed to be small ($d_p \ll D$), and since ψ and $\partial\psi/\partial r$ equal zero at the cylinder edge (central streamline and no-slip condition), the development of ψ in (1.33) into Taylor series yields

$$\eta = \frac{d_p^2}{4U_0 D}\frac{\partial^2\psi}{\partial r^2}\bigg|_{D/2,\theta_c} = \frac{1}{4}R^2\left(\frac{D}{U_0}\frac{\partial^2\psi}{\partial r^2}\bigg|_{D/2,\theta_c}\right) = \frac{1}{4}R^2\xi_c, \tag{1.35}$$

with $\xi_c = (D/U_0)\partial^2\psi/\partial r^2|_{D/2,\theta_c}$ being the dimensionless vorticity at the maximum capture position. For $Re \leq 1$, they used Kaplun's approximation of the stream function [106, 107]

$$\psi = U_0 D(\Delta - 0.87\Delta^3)\left(\tilde{r}\ln\tilde{r} - \frac{\tilde{r}}{2} + \frac{1}{2\tilde{r}}\right)\sin\theta, \tag{1.36}$$

where Δ is defined in equation (1.28). This implies that the dimensionless vorticity ξ_c simply reads

$$\xi_c = 4(\Delta - 0.48\Delta^3). \tag{1.37}$$

In the range $1 < Re < 200$, they took numerical results from literature and found that ξ_c was best fitted with

$$\xi_c = 1.76Re^{0.52}. \tag{1.38}$$

Substituting the expressions (1.37) and (1.38) in (1.33), the final semi-analytical expression of the capture efficiency is

$$\eta = \begin{cases} (\Delta - 0.48\Delta^3)R^2, & Re \leq 1, \\ 0.44Re^{0.52}R^2, & 1 < Re < 200. \end{cases} \tag{1.39}$$

The prior studies agreeing on the square variation of efficiency in the diameter ratio $\eta \sim R^2$, the table 1.2 lists the different exponents n found in the scaling in the Reynolds number $\eta \sim Re^n$.

Influence of collector motion

We have seen how the capture efficiency depends on the flow conditions and the particle size in the case of a fixed collector. Yet, passive filter feeders and terrestrial collectors are flexible and move continuously due to the surrounding flow. It is then important to consider the

study	method	exponent	range
Weber and Paddock [13]	semi-analytical	0.520	$1 < Re < 200$
Palmer *et al.* [101]	experimental	0.718	$38 < Re < 486$
Haugen and Kragset [10]	2D DNS, IBM	0.700	$20 < Re < 1685$
Espinosa-Gayosso *et al.* [12]	2D DNS	0.700	$47 < Re \lesssim 100$
	3D DNS	0.500	$180 < Re \lesssim 1000$

Table 1.2 Summary of the exponents n found in the scaling of capture efficiency with the Reynolds number $\eta \sim Re^n$, in the case of a fixed cylinder.

motion of the collector when conducting studies on living species.

To gain insight about the influence of collector motion on capture, McCombe and Ackerman [108] imposed pure transverse and stream-wise oscillations for a set of amplitudes and frequencies to a circular collector, launched particles, and calculated the capture efficiency as did Palmer *et al.* [101]. They found that the transverse motion is beneficial for the capture (up to 4 times higher), especially if the oscillations are rapid and the flow is of low Reynolds number. However, as the Reynolds number increases, the capture efficiency drops below the case of a fixed collector (by $20 - 30\%$ for $Re \sim 560$).

In terrestrial vegetation, the best way to capture more particles is to let the collector free to oscillate in both transverse and stream-wise directions. In a series of in-field experiments, McCombe and Ackerman [108] counted the number of pollen grains captured by a timothy grass (*Phleum pratense*) in four configurations: fixed, restricted to transverse motion only, restricted to longitudinal motion only, and untethered (i.e. free to move). It was the latter configuration that achieved the highest capture efficiency, followed by the case of transverse motion only.

On the numerical side, Krick and Ackerman [109] simulated flows, with ANSYS CFX [110], around cylinders vibrating transverse and stream-wise to the upstream fluid velocity. They solved the unsteady Reynolds-averaged Navier-Stokes (URANS) equations with a k-ω SST turbulence model. The particles were subjected to the drag $\boldsymbol{F}_\mathrm{D}$ and the pressure gradient force

$$\boldsymbol{F}_\mathrm{P} = -\frac{4}{3}\pi \left(\frac{d_\mathrm{p}}{2}\right)^3 \boldsymbol{\nabla} p, \tag{1.40}$$

where p is the fluid pressure. The drag $\boldsymbol{F}_\mathrm{D}$ was the same as in equation (1.20), though without the Stokes-Cunningham correction factor. They calculated a scaled version of the efficiency

$$\eta = \frac{N}{N_\mathrm{init}} \left(\frac{l_\mathrm{init}}{D}\right), \tag{1.41}$$

with l_{init} being the slot length from which particles are released ($l_{\text{init}} > D$). As in McCombe and Ackerman [108], they found that transverse vibrations increase the capture efficiency, but only if the transverse amplitude $Y_{\max}$ is large ($Y_{\max} \approx 1.06D$), whereas barely vibrating cylinders ($Y_{\max} \approx 0.06D$) resulted in a decrease in η. When it comes to stream-wise oscillations, they were overall detrimental for capture, even for large stream-wise amplitudes $X_{\max} \approx 0.48D$. Krick and Ackerman [109] pointed out the idea of 'additional momentum', which says that a particle hitting a transversely oscillating cylinder acquires relative momentum, hence is more likely to penetrate into the boundary layer, while in contrast a longitudinally oscillating cylinder ($Y_{\max} \ll X_{\max}$) results in a zero net momentum over a period.

1.2 Synthesis

Biologists conducted a number of experiments on soft corals, in-field and in water flume, to investigate how water flow affects the feeding rate [32, 111–113]. Although these works came with valuable results, their interpretation is not always clear, given that many factors can be involved in the capture process such as the morphology of the branches, polyps size, tentacles length, and swimming ability of food particles. It follows that data often have non-negligible statistical variance and errors, which adds a certain difficulty in grasping the essentials of the results. This disparity is among the reasons why interpretation of results is chiefly qualitative and assumption-based. Furthermore, the numerous experimental methods, species, and food particles considered yielded various results without any gateways, hence hard to utilise in explaining phenomena. This is why a unified framework that extracts the common features is deemed essential. A fluid mechanics scope is a good fit for this task. By clearing the unneeded biological complexity and using scaled (i.e. dimensionless) parameters, it idealises the study of soft corals intercepting food and uncovers basic mechanisms of particle capture.

We have seen that data describing VIV on the one hand, and particle capture by fixed collectors on the other hand, are abundant in literature. Surprisingly, though, we have no study that connects VIV with particle capture. Even the handful of papers that examined the effect of collector motion [108, 109] were imposing oscillation frequencies and amplitudes, not always covering the values seen in the living world. Species in nature vibrate in response to the fluid flow, and the motion frequency and amplitude vary in an intertwined manner and cannot be decoupled. The scarcity of data on vibrating collectors will let biologists unable to draw clear and founded conclusions on particle capture process in species. Engineers too are concerned with this shortage in data. In fact, VIV have been already recognised as a promising driver for energy harvesting, so there are reasons to think they might bring

advantage, yet hidden, to particle filtering as well. There is, hence, a real need to supply the scientific community with an analysis of particle capture by collectors under VIV.

More and more studies are using computational fluid dynamics (CFD) to simulate the flow and particle capture. Not only the computational capacities are constantly improving, but the numerical simulations have the advantage over experiments of freely handling flow conditions and changing parameter values, which provides data spanning several configurations. In the previous works, we also note the diversity of CFD codes, as well as methods to compute the flow field and particle advection. The calculation method of the capture efficiency is not unique either, and consisted on counting each of the captured particles [10, 109] or calculating the flux of captured particles through the capture window length [11, 12]. It is always enriching to have data from different sources because they give the opportunity to compare the level of credibility of methods. The numerical approach has, nevertheless, caveats if the numerical errors are uncontrolled. For instance, using ANSYS CFX, Krick and Ackerman [109] reported integration errors due to the removal of a number of particles when the amplitude of the collector motion is large, and managed to introduce a correction factor. Even though they insisted this correction may not alter qualitatively the results, it gave a 14-fold difference in values between the worst and best cases. Unlike commercial software, in-house codes are better in controlling errors and spotting their origin, yielding more reliable results.

1.3 Goals and outline

In this project, we inquire into the biomechanics of soft coral vibrations by confirming two hypotheses:

- soft coral vibrations at the branch level are vortex-induced,
- vortex-induced vibrations increase the rate of food interception.

We adopt a numerical approach. We will compute fluid flows using CaDyF [114], an in-house FSI finite element solver developed at Polytechnique Montréal. Besides, a Python code [115] will import the output of CaDyF, solve the trajectories of particles advected by the flow, and calculate the rate of interception.

In chapter 2 we present the numerical methodology and describe the simulation strategy of CaDyF. Chapter 3 puts forward some arguments that support vortex-induced vibrations as the most plausible cause of the soft coral branch motion, ruling out other types of flow-induced instabilities. In chapter 4, we idealise the soft coral branch into a circular cylinder, assimilate

food particles to spheres, and state the governing equations of the advection dynamics. We also introduce the definition of the capture rate, and list the important dynamical variables influencing the capture process. Chapter 5 is dedicated to the case of a fixed cylinder. This step will help us understand the basics of the capture process without the influence of the vibration frequency. In addition, we propose an analytical derivation of the power law that the capture rate follows. In the subsequent chapter 6, we let the cylinder free to oscillate, and analyse how the motion affects the capture rate. In chapter 7 we move on to three-dimensional finite element simulations, using the PYTHON based solver FEniCS, of a clamped Kirchhoff rod under hydrodynamic drag and vortex-induced lift. Our main motivation is to reproduce a realistic motion of a living soft coral branch under a wave action. In the end, chapter 8 discusses the results we obtained, proposes further improvements of our idealised model, and paves the way for potential applications.

CHAPTER 2 FLUID-STRUCTURE SIMULATIONS

This thesis is based mainly on two-dimensional flow simulations. CaDyF is the in-house code we used in this study [114]. It has been developed over decades owing to the efforts of students and professors at Polytechnique Montréal. CaDyF solves monolithically the coupled fluid-structure system with a mixed finite element formulation. In this chapter, we present the fluid-structure equations of a rigid body within a fluid flow, and explain the numerical integration method.

2.1 Fluid-structure coupling

We describe the sea water as an incompressible fluid, of density ρ_f and dynamic viscosity μ_f. In an Arbitrary Lagrangian-Eulerian (ALE) framework, the continuity and Navier-Stokes equations read

$$\boldsymbol{\nabla} \cdot \boldsymbol{U}_\mathrm{f} = 0, \tag{2.1}$$

$$\frac{\partial \boldsymbol{U}_\mathrm{f}}{\partial t} + \left[(\boldsymbol{U}_\mathrm{f} - \boldsymbol{V}) \cdot \boldsymbol{\nabla}\right] \boldsymbol{U}_\mathrm{f} = \frac{1}{\rho_\mathrm{f}} \left[-\boldsymbol{\nabla} p + \mu_\mathrm{f} \nabla^2 \boldsymbol{U}_\mathrm{f}\right], \tag{2.2}$$

where $\boldsymbol{U}_\mathrm{f}$ and p are respectively the fluid velocity and pressure. $\boldsymbol{V}$ is the velocity of the mesh due to the body motion. Each element of the mesh acts as a linearly deforming solid of Lamé coefficients λ and μ [116]. Denoting the derivative with respect to the original configuration as ∇_0, the equation of the mesh displacement $\boldsymbol{\chi}$ is [117]

$$\nabla_0 \cdot \mathbf{S} = \mathbf{0}, \tag{2.3}$$

$$\mathbf{S} = 2\mu \mathbf{E} + \lambda (\mathrm{tr}\mathbf{E}) \mathbf{I}, \tag{2.4}$$

where $\mathbf{I}$ is the identity tensor, and

$$\mathbf{E} = \frac{1}{2} \left(\boldsymbol{\nabla}_0 \boldsymbol{\chi} + \boldsymbol{\nabla}_0 \boldsymbol{\chi}^\mathsf{T}\right) \tag{2.5}$$

the strain tensor of that 'pseudo-solid' element. The velocity of the moving mesh is then given by

$$\frac{\partial \boldsymbol{\chi}}{\partial t} = \boldsymbol{V}. \tag{2.6}$$

On the other hand, the rigid body is a harmonic oscillator of mass m, damping coefficient c,

and stiffness k. Its position $\boldsymbol{X}$ is solution of

$$m\frac{\mathrm{d}^2\boldsymbol{X}}{\mathrm{d}t^2}+c\frac{\mathrm{d}\boldsymbol{X}}{\mathrm{d}t}+k\boldsymbol{X}=\boldsymbol{F}_{\mathrm{hydro}}. \tag{2.7}$$

Here $\boldsymbol{F}_{\mathrm{hydro}}$ is the total hydrodynamic load on the rigid body

$$\boldsymbol{F}_{\mathrm{hydro}}=\oint_{(\Gamma)}\left[-p\mathbf{I}+\mu_{\mathrm{f}}\left(\boldsymbol{\nabla}\boldsymbol{U}_{\mathrm{f}}+\boldsymbol{\nabla}\boldsymbol{U}_{\mathrm{f}}^{\mathsf{T}}\right)\right]\mathrm{d}\boldsymbol{n}, \tag{2.8}$$

with (Γ) being the boundary of the body and $\mathrm{d}\boldsymbol{n}$ the integration element pointing outwards. Denoting the upstream velocity as U_0, and a characteristic length of the rigid body as D, we use the following dimensionless variables

$$\begin{gathered}\bar{\boldsymbol{U}}_{\mathrm{f}}=\frac{1}{U_0}\boldsymbol{U}_{\mathrm{f}},\quad \bar{\boldsymbol{V}}=\frac{1}{U_0}\boldsymbol{V},\quad \bar{\boldsymbol{\chi}}=\frac{1}{D}\boldsymbol{\chi},\quad \bar{\boldsymbol{X}}=\frac{1}{D}\boldsymbol{X},\\ \bar{p}=\frac{p}{\rho_{\mathrm{f}}U_0^2},\quad \bar{t}=\frac{tU_0}{D},\quad \bar{\boldsymbol{n}}=\frac{1}{D}\boldsymbol{n},\quad \bar{\boldsymbol{\nabla}}=D\boldsymbol{\nabla},\end{gathered} \tag{2.9}$$

to obtain the fully coupled system

$$\bar{\boldsymbol{\nabla}}\cdot\bar{\boldsymbol{U}}_{\mathrm{f}}=0, \tag{2.10a}$$

$$\frac{\partial\bar{\boldsymbol{U}}_{\mathrm{f}}}{\partial\bar{t}}+\left[(\bar{\boldsymbol{U}}_{\mathrm{f}}-\bar{\boldsymbol{V}})\cdot\bar{\boldsymbol{\nabla}}\right]\bar{\boldsymbol{U}}_{\mathrm{f}}=\left[-\bar{\boldsymbol{\nabla}}\bar{p}+\frac{1}{Re}\bar{\nabla}^2\bar{\boldsymbol{U}}_{\mathrm{f}}\right], \tag{2.10b}$$

$$\bar{\nabla}_0\mathbf{S}=\mathbf{0},\quad \mathbf{S}=2\mu\mathbf{E}+\lambda(\mathrm{tr}\mathbf{E}), \tag{2.10c}$$

$$\mathbf{E}=\frac{1}{2}\left(\bar{\boldsymbol{\nabla}}_0\bar{\boldsymbol{\chi}}+\bar{\boldsymbol{\nabla}}_0\bar{\boldsymbol{\chi}}^{\mathsf{T}}\right), \tag{2.10d}$$

$$\frac{\mathrm{d}^2\bar{\boldsymbol{X}}}{\mathrm{d}\bar{t}^2}+2\zeta\left(\frac{2\pi}{U_{\mathrm{r}}}\right)\frac{\mathrm{d}\bar{\boldsymbol{X}}}{\mathrm{d}\bar{t}}+\left(\frac{2\pi}{U_{\mathrm{r}}}\right)^2\bar{\boldsymbol{X}}=\frac{1}{M}\bar{\boldsymbol{F}}_{\mathrm{hydro}}, \tag{2.10e}$$

$$\bar{\boldsymbol{F}}_{\mathrm{hydro}}=\oint_{(\Gamma)}\left[-\bar{p}\mathbf{I}+\frac{1}{Re}\left(\bar{\boldsymbol{\nabla}}\bar{\boldsymbol{U}}_{\mathrm{f}}+\bar{\boldsymbol{\nabla}}\bar{\boldsymbol{U}}_{\mathrm{f}}^{\mathsf{T}}\right)\right]\mathrm{d}\bar{\boldsymbol{n}}, \tag{2.10f}$$

where

$$Re=\rho_{\mathrm{f}}U_0D/\mu_{\mathrm{f}}, \tag{2.11}$$

$$U_{\mathrm{r}}=\frac{2\pi U_0}{D}\sqrt{\frac{m}{k}}, \tag{2.12}$$

$$\zeta=\frac{c}{2\sqrt{mk}}, \tag{2.13}$$

$$M=\frac{m}{\rho_{\mathrm{f}}D^2}, \tag{2.14}$$

are the Reynolds number, the reduced velocity, the damping ratio, and the mass ratio. For

every simulation case throughout this project we take $\zeta = 0$ and $M = 1$.

2.2 Domain and boundary conditions

The fluid domain, in all the ensuing simulations, is the same, and large enough ($-40 \leq \bar{x} \leq 120$ and $-60 \leq \bar{y} \leq 60$) to avoid confinement effects [118]. We discretised it into Taylor-Hood ($\mathcal{P}_2 - \mathcal{P}_1$) triangular elements, as a result of which the velocity is third order accurate and the pressure is second order accurate [119].

Initially, the fluid is at rest in the whole domain. The boundary conditions on the fluid velocity $\bar{\boldsymbol{U}}_\mathrm{f}$ are a uniform Dirichlet at the entry ($\bar{x} = -40$), homogeneous Neumann at the exit ($\bar{x} = 120$), symmetry at the top and bottom boundaries ($\bar{y} = \pm 60$), and no-slip at the rigid body edge (Γ). Finally, the node displacement $\bar{\boldsymbol{\chi}}$ at (Γ) takes the same value as the rigid body displacement.

2.3 Time integration

CaDyF integrates the coupled system (2.10) using hp-adaptive Backward Differential Formulas (BDF) methods [117]. The order and time step adjust automatically so that the local truncation error remains smaller than a constant absolute tolerance equal to 10^{-5}. When the rigid body is fixed, CaDyF discards the equation (2.10e), and solves the fluid problem in an Eulerian frame of reference ($\bar{\boldsymbol{\chi}} = \mathbf{0}$).

CHAPTER 3 ORIGIN OF SOFT CORAL VIBRATIONS

At the first glance, it is not clear what causes the vibrations of the soft coral branches, because many types of flow-induced instabilities may be involved, such as buffeting, galloping, or fluidelastic vibrations. In this chapter, we will state simple and basic arguments to regard these causes as improbable, and lay out the argument to conclude that the vortex-induced vibrations are the only plausible source of the observed soft coral high frequency motion.

3.1 Clues about vortex-induced vibrations

To get an idea about the rough scale of the phenomenon, we analysed a video of a vibrating bipinnate sea plume under a sea wave action [17] with the software IMAGEJ [120]. First, by tracking some debris moving with the flow, we estimated the water speed to $U_0 \sim 10$ cm/s. Then, taking a branch diameter of $D \sim 2$ mm [41, 121], and assuming that the seawater and pure water have the same kinematic viscosity $\nu_\mathrm{f} = \mu_\mathrm{f}/\rho_\mathrm{f} \approx 10^{-6}$ m^2/s, we found that the Reynolds number is $Re = U_0 D/\nu_\mathrm{f} \sim 200$. This value suggests that there is a von Kármán vortex street downstream of the branches. Moreover, we followed parts of the branch having pronounced displacements over several periods, and estimated the vibration frequency to $f_\mathrm{n} \sim 7 - 9$ Hz. Therefore, it yields a reduced velocity of $U_\mathrm{r} = U_0/f_\mathrm{n} D \sim 5 - 7$. All these ingredients are specific to VIV at lock-in.

3.2 Refuting buffeting

To see whether the soft coral vibration is due to a turbulence buffeting, we looked at the wave spectral density of regions in the Gulf of Mexico. In the website of the National Data Buoy Center (NDBC) [122], we collected recent measurements in the stations: Orange Beach (Station 42012, south-east of Mobile, Alabama, depth 25.9 m), Galveston (Station 42035, east of Galveston, Texas, depth 16.2 m), Grand Isle Outer (Station 42093, Louisiana, depth 33.5 m), and Edgmont Channel Entrance (Station 42098, Florida, depth 12 m). As shown in Figure 3.1, all the spectra have a peak in amplitude at a frequency between 0.15 and 0.24 Hz, and drop beyond 0.5 Hz. This range of frequencies matches with the gentle swaying motion of the soft coral, but does not suit the rapid motion of the branches. Even if we consider that the spectral density follows the Pierson-Moskowitz spectrum, the peak frequency would be $f_\mathrm{peak} = 0.14 g/U_\mathrm{w}$. Then taking a wind velocity of $U_\mathrm{w} \sim 5$ m/s (10 knots) yields $f_\mathrm{peak} \sim 0.3$ Hz. Therefore, the main harmonic in sea waves is, in any case, much smaller

than the frequencies of the observed branch oscillations ($f_{\mathrm{n}} \sim 5 - 7$ Hz, 20 times higher). Buffeting is an implausible cause for the observed high frequency soft coral vibrations.

3.3 Refuting fluidelastic instability

Since the branches of a bipinnate sea plume *Antillogorgia bipinnata* lay side-by-side in the same plane perpendicular to the flow, we may suspect fluidelastic vibrations. In general, they are attached with uniform spacing along the vertical main stem. The separation distance at the attachment level is about 3 to 8 diameters [41], and varies according to the habitat (separation distance of about 7 diameters in deep waters [49]). Yet, as for a clamped flexible beam, the vibrations have no effect near the clamped end, hence the instability takes place only relatively away from the stem. Because the branches diverge away, they become more isolated from each other, thus making the fluidelastic instability less probable. We based our estimation on a dried *A. bipinnata* (Figure 3.2), and found that the separation distance was between 4.5 diameters and 8.5 diameters. Since the fluidelastic instability occurs only when the separation distance is less than 4 diameters (section 1.1.2, chapter 1), we consider the branches independent and we do not expect a fluidelastic instability to appear.

3.4 Refuting galloping

The shape of a soft coral branch resembles, overall, a slender cylinder with a circular cross-section. The polyps covering it have a size of only 10% or less of the branch diameter [41]. They represent, hence, a small geometrical perturbation of a circular cylinder. Under cross-flow, the circular cylinder is 'immune to galloping' and is well-known to undergo only VIV [67, 123]. The soft coral branch is then, by analogy, unlikely to gallop. But how unlikely is it?

We decided to turn to a quantitative analysis and evaluate the Glauert-den Hartog criterion [124, 125]. It states that galloping can arise if

$$\frac{\mathrm{d}C_{\mathrm{L}}}{\mathrm{d}\alpha} + C_{\mathrm{D}} < 0, \tag{3.1}$$

where C_{L} and C_{D} are the lift and drag coefficients, and α the angle of attack. To find out whether the soft coral fulfils this criterion, we simulated two-dimensional flows around an idealised branch cross-section of *A. bipinnata*. Figure 3.3 shows the flow field around the idealised coral branch cross-section with two diametrically opposed protuberances having a size of 10% of the cylinder diameter. Considering the observed transverse displacements of

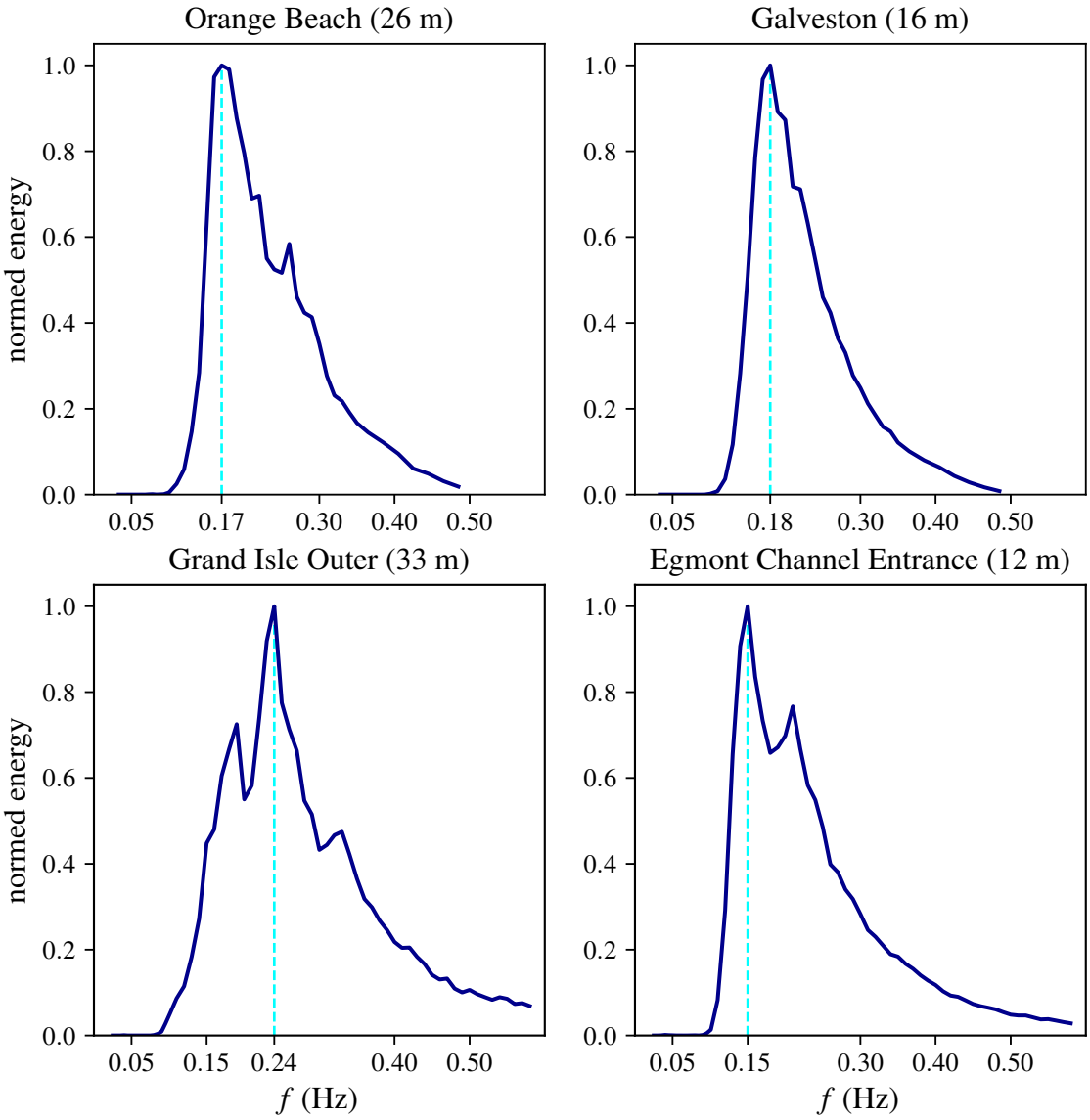

Figure 3.1 Density spectra of regions in the Gulf of Mexico (National Data Buoy Center, from March 31st to April 5th, 2020). Between parentheses is the sea depth in each region. The highlighted dashed line marks the peak frequency.

Figure 3.2 Dried bipinnate sea plume (*Antillogorgia bipinnata*) [2]. The separation space between branches goes from 4.5 to 8.5 diameters. Photo by © Charles G. Messing, with permission.

the branch, the reasonable range of angles of attack is between 0° and 20°. We extracted the fluid-dynamic coefficients and calculated the quantity $\mathrm{d}C_\mathrm{L}/\mathrm{d}\alpha + C_\mathrm{D}$ using a cubic spline interpolation of data points as shown in Figure 3.4. This quantity is slightly decreasing, but stays always positive and close to 1. Therefore, according to the Glauert-den Hartog criterion, galloping is ruled out as a cause of soft coral vibrations.

Table 3.1 summarises the arguments presented in this chapter. We can claim that the rapid motion of the soft coral branches is not extraneously-induced by turbulence buffeting nor movement-induced by fluidelastic instability or galloping, and is rather due to vortices forming in the wake behind the branch.

flow-induced instability	category	likelihood	
		probable	improbable
Turbulence buffeting	extraneously-induced excitation		x
Fluidelastic instability	movement-induced excitation		x
Galloping	movement-induced excitation		x
Vortex-induced vibrations	instability-induced excitation	x	

Table 3.1 Summary of the likelihood of each potential flow-induced instability as the cause of the rapid motion of the soft coral branches.

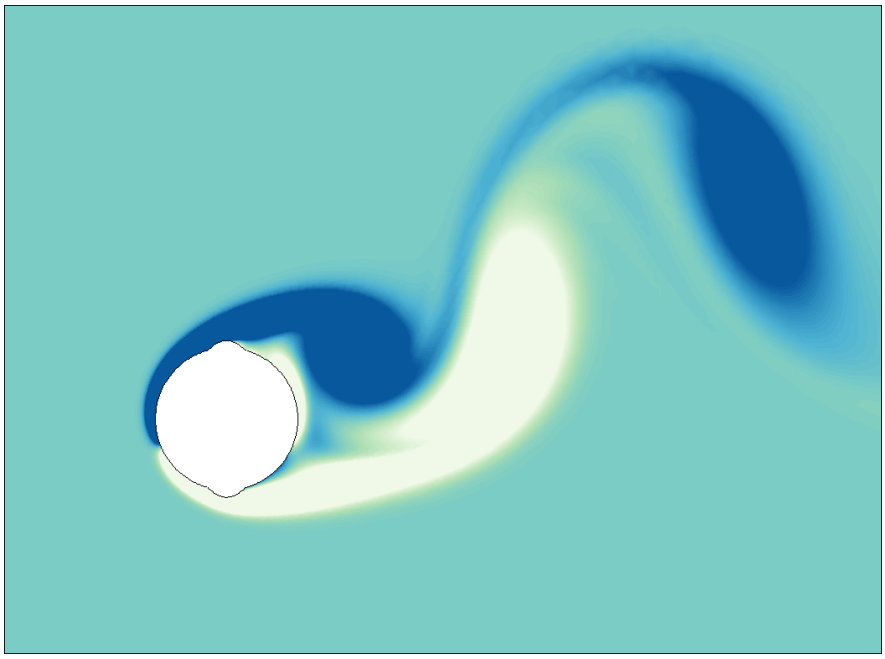

Figure 3.3 Vorticity contour plot of a flow around an idealised soft coral cross-section at the angle of attack 20° ($Re = 200$). The cross-section is a circle, and polyps are the two diametrically opposed arcs of circle. Their size is 10% of the circle diameter.

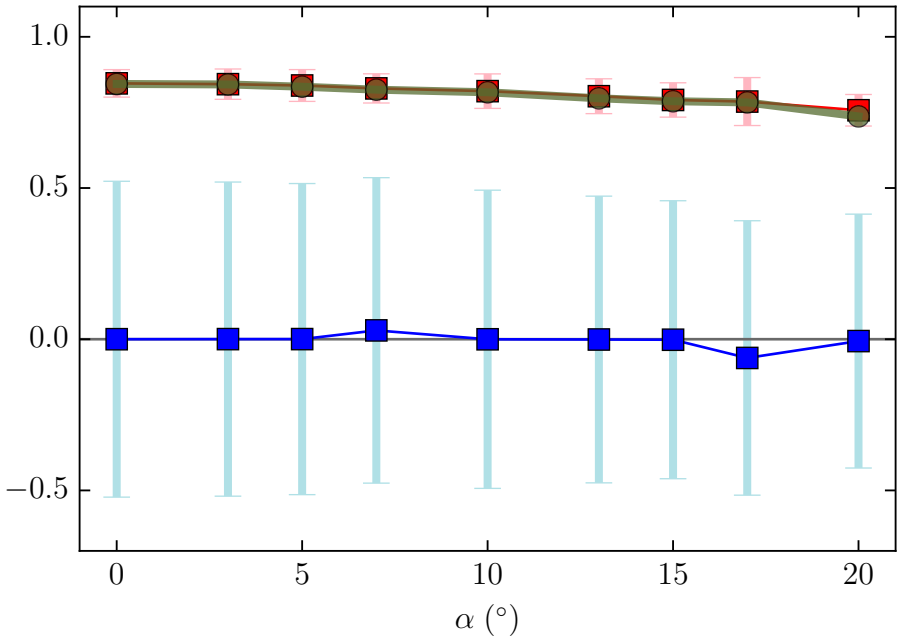

Figure 3.4 Mean values of the fluctuating drag (■) and lift (■) coefficients of an idealised branch cross section (Figure 3.3) at $Re = 200$. The bars refer to the maximum and minimum values of the variables. We calculated the mean value of $\mathrm{d}C_\mathrm{L}/\mathrm{d}\alpha + C_\mathrm{D}$ (●) from cubic spline interpolation of data points.

CHAPTER 4 PARTICLE ADVECTION AND CAPTURE RATE

After diagnosing the main probable cause of the observed soft coral vibrations, in this chapter we add a new ingredient to the the water flow-coral branch system: food particles. Our goal is to simulate the trajectories of particles advected by the flow, detect the ones intercepted by the branch, and quantify the rate of capture.

4.1 Branch model

The special skin texture of soft corals, as well as the series of polyps covering it, influence certainly in its vicinity the fluid behaviour, thereby the particle capture. Yet, owing to the small size of the polyps that cover the branch of *A. bipinnata*, which is about 10% of the branch diameter [41], we decided to idealise the biologically complex soft coral branch and consider a circular cylinder. This approach brings our study back into a familiar fluid dynamics problem, aligns with the benchmark problem in the particle filtering literature, and unmasks the basic mechanisms of particle interception.

We simulate fluid flows around fixed and vibrating cylinders, in order to highlight the difference in particle capture. We consider a spring-mounted cylinder subjected to a two-dimensional cross-flow as schematised in Figure 5.1. The cylinder is a harmonic oscillator free to move stream-wise and transverse to the main flow. The hydrodynamic load $\boldsymbol{F}_{\mathrm{hydro}}$, defined in equation (2.10f), forces its motion. Therefore, its position $\boldsymbol{X}_{\mathrm{cyl}}$ verifies the equation (2.10e)

$$\frac{\mathrm{d}^2\bar{\boldsymbol{X}}_{\mathrm{cyl}}}{\mathrm{d}\bar{t}^2} + \left(\frac{2\pi}{U_{\mathrm{r}}}\right)^2 \bar{\boldsymbol{X}}_{\mathrm{cyl}} = \bar{\boldsymbol{F}}_{\mathrm{hydro}}. \tag{4.1}$$

The cylinder stands initially at the position $\bar{\boldsymbol{X}}_{\mathrm{cyl}} = \boldsymbol{0}$. The domain contains 96 000 nodes and 48 000 triangular elements, with smaller ones in the wake and close to the cylinder to resolve the vortex shedding and the boundary layer (Figure 4.2). An example of flow solution is shown in Figure 4.3.

4.2 Particle dynamics

4.2.1 Governing equations

We consider food particles as spheres of diameter d_{p} and density ρ_{p}. We assume they have no influence on the flow nor mutual interaction. Furthermore, these particles cannot change

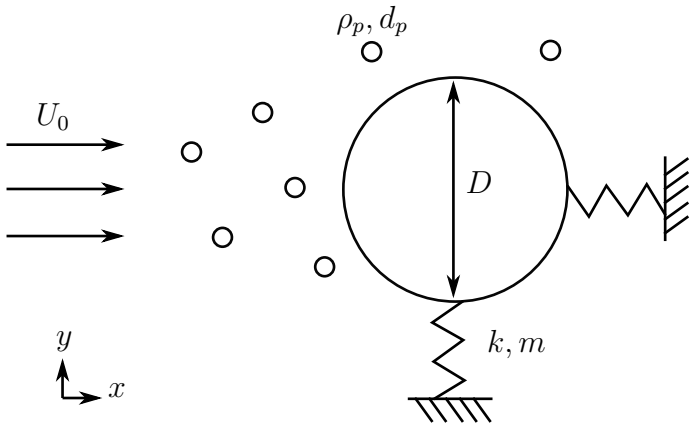

Figure 4.1 Schematics of particles advected by a flow around a free-to-oscillate cylinder

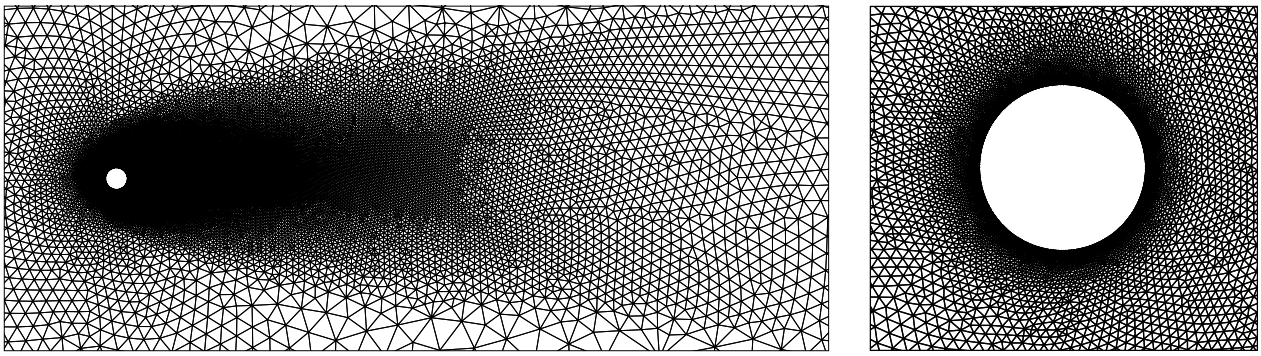

Figure 4.2 Close-ups of the fluid mesh highlighting the densification of elements (a) in the wake and (b) around the boundary layer.

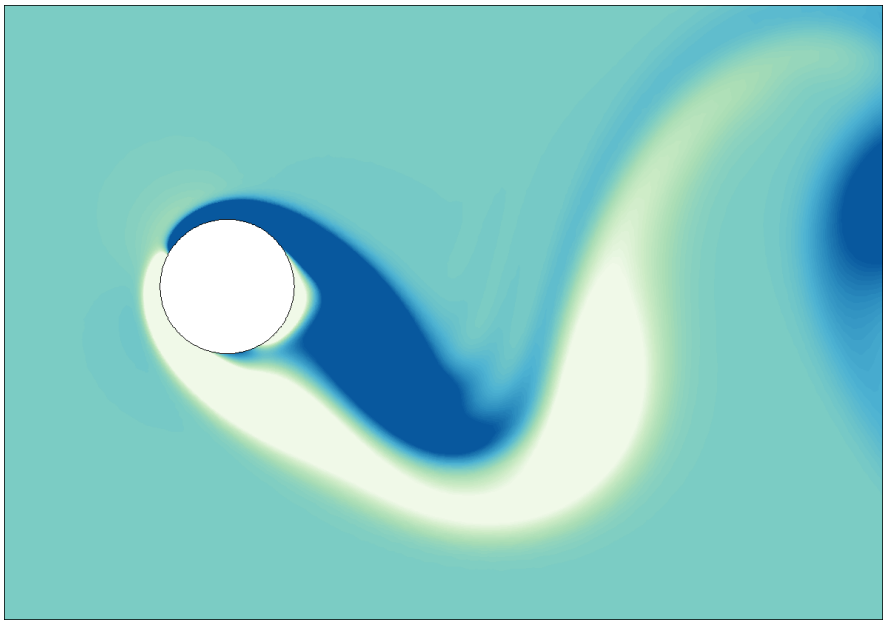

Figure 4.3 Vorticity contour of a flow around a vibrating cylinder at $Re = 100$ and $U_\mathrm{r} = 5$

actively their trajectory, as in the case of a swimming plankton for instance. Neglecting gravity and buoyancy effects, the remaining forces applied on a particle are the drag $\boldsymbol{F}_\mathrm{D}$, the pressure load $\boldsymbol{F}_\mathrm{P}$, and the added mass force $\boldsymbol{F}_\mathrm{A}$. The governing equations describing the particle trajectory are

$$\frac{\mathrm{d}\boldsymbol{x}_\mathrm{p}}{\mathrm{d}t} = \boldsymbol{u}_\mathrm{p}, \tag{4.2a}$$

$$\frac{\mathrm{d}\boldsymbol{u}_\mathrm{p}}{\mathrm{d}t} = \frac{1}{m_\mathrm{p}}(\boldsymbol{F}_\mathrm{D} + \boldsymbol{F}_\mathrm{P} + \boldsymbol{F}_\mathrm{A}), \tag{4.2b}$$

where $m_\mathrm{p} = \rho_\mathrm{p}\pi d_\mathrm{p}^3/6$ is the mass of the particle, $\boldsymbol{x}_\mathrm{p}$ its position, and $\boldsymbol{u}_\mathrm{p}$ its velocity.

Now let us give the expressions of these forces. First, the drag reads

$$\boldsymbol{F}_\mathrm{D} = -\frac{1}{2}C_\mathrm{D}\rho_\mathrm{f}\pi\left(\frac{d_\mathrm{p}}{2}\right)^2 ||\boldsymbol{u}_\mathrm{p} - \boldsymbol{U}_\mathrm{f}||\,(\boldsymbol{u}_\mathrm{p} - \boldsymbol{U}_\mathrm{f})\,, \tag{4.3}$$

where C_D is the drag coefficient of a sphere. It is a function of the particle-based Reynolds number

$$Re_\mathrm{p} = \frac{\rho_\mathrm{f}\,||\boldsymbol{u}_\mathrm{p} - \boldsymbol{U}_\mathrm{f}||\,d_\mathrm{p}}{\mu_\mathrm{f}}, \tag{4.4}$$

which is unknown *a priori*. For this reason we considered the Schiller-Nauman interpola-

tion [103]

$$C_{\mathrm{D}} = \frac{24}{Re_{\mathrm{p}}}(1 + Re_{\mathrm{p}}^{0.687}), \tag{4.5}$$

which is valid for $Re_{\mathrm{p}} < 800$.

Next, the pressure load is given by

$$\boldsymbol{F}_{\mathrm{P}} = -\frac{4}{3}\pi \left(\frac{d_{\mathrm{p}}}{2}\right)^3 \boldsymbol{\nabla} p. \tag{4.6}$$

Finally, the added mass force is proportional to the acceleration of the particle relative to the fluid

$$\boldsymbol{F}_{\mathrm{A}} = -C_{\mathrm{m}}\rho_{\mathrm{f}}\frac{4}{3}\pi \left(\frac{d_{\mathrm{p}}}{2}\right)^3 \left(\frac{\mathrm{d}\boldsymbol{u}_{\mathrm{p}}}{\mathrm{d}t} - \frac{\mathrm{d}\boldsymbol{U}_{\mathrm{f}}}{\mathrm{d}t}\right). \tag{4.7}$$

Here C_{m} is the mass coefficient of a sphere. Neglecting the dependence of C_{m} on the confinement of the particle as well as its position with respect to boundaries [126], we took it as a constant equal to 1/2.

Using the following dimensionless numbers

$$\rho^{+} = \frac{\rho_{\mathrm{p}}}{\rho_{\mathrm{f}}}, \quad R = \frac{d_{\mathrm{p}}}{D},$$

we rewrite the particle-based Reynolds number as

$$Re_{\mathrm{p}} = ReR\left|\left|\bar{\boldsymbol{u}}_{\mathrm{p}} - \bar{\boldsymbol{U}}_{\mathrm{f}}\right|\right|, \tag{4.8}$$

and the governing system (4.2) becomes

$$\frac{\mathrm{d}\bar{\boldsymbol{x}}_{\mathrm{p}}}{\mathrm{d}\bar{t}} = \bar{\boldsymbol{u}}_{\mathrm{p}}, \tag{4.9a}$$

$$\frac{\mathrm{d}\bar{\boldsymbol{u}}_{\mathrm{p}}}{\mathrm{d}\bar{t}} = \bar{\boldsymbol{F}}_{\mathrm{D}} + \bar{\boldsymbol{F}}_{\mathrm{P}} + \bar{\boldsymbol{F}}_{\mathrm{A}} = \bar{\boldsymbol{F}}_{\mathrm{total}}, \tag{4.9b}$$

with

$$\bar{\boldsymbol{F}}_{\mathrm{D}} = -\frac{18}{\rho^{+}R^2 Re}\left(1 + Re_p^{0.687}\right)\left(\bar{\boldsymbol{u}}_{\mathrm{p}} - \bar{\boldsymbol{U}}_{\mathrm{f}}\right), \tag{4.10}$$

$$\bar{\boldsymbol{F}}_{\mathrm{P}} = -\frac{1}{\rho^{+}}\bar{\boldsymbol{\nabla}}\bar{p}, \tag{4.11}$$

$$\bar{\boldsymbol{F}}_{\mathrm{A}} = -\frac{C_{\mathrm{m}}}{\rho^{+}}\left(\frac{\mathrm{d}\bar{\boldsymbol{u}}_{\mathrm{p}}}{\mathrm{d}\bar{t}} - \frac{\mathrm{d}\bar{\boldsymbol{U}}_{\mathrm{f}}}{\mathrm{d}\bar{t}}\right). \tag{4.12}$$

4.2.2 Numerical solution

Temporal integration

We wrote a PYTHON code [115] that imports the flow solution of CADYF, which is in an ALE frame, and integrates the system of equations (4.9) in a Lagrangian frame with a forward Euler scheme. The particles start from the line $\bar{x}_0 = -2$ (for a given $\bar{y}_0$) upstream from the cylinder centre, where the flow is horizontal enough and unperturbed. The local fluid speed is then assigned as their initial velocity.

The time step depends on the Reynolds number and the characteristics of the particle. To find out an upper bound of the time step, let us rewrite the system of equations (4.9) as

$$\frac{\mathrm{d}\bar{\boldsymbol{x}}_\mathrm{p}}{\mathrm{d}\bar{t}} = \bar{\boldsymbol{u}}_\mathrm{p}, \tag{4.13a}$$

$$\frac{\mathrm{d}\bar{\boldsymbol{u}}_\mathrm{p}}{\mathrm{d}\bar{t}} = -\frac{1 + Re_\mathrm{p}^{0.687}}{\tau}\bar{\boldsymbol{u}}_\mathrm{p} + \Phi(\bar{\boldsymbol{U}}_\mathrm{f}, \frac{\mathrm{d}\bar{\boldsymbol{U}}_\mathrm{f}}{\mathrm{d}\bar{t}}, \bar{\boldsymbol{\nabla}}\bar{p}, Re_\mathrm{p}), \tag{4.13b}$$

where

$$\tau = \frac{\rho^+ R^2 Re}{18}\left(1 + \frac{C_\mathrm{m}}{\rho^+}\right), \tag{4.14}$$

and Φ regroups all remaining force terms (assuming $\bar{\boldsymbol{u}}_\mathrm{p}$ and Re_p are independent, Figure 4.6). The integration scheme is

$$\bar{\boldsymbol{x}}_\mathrm{p}^{n+1} = \bar{\boldsymbol{x}}_\mathrm{p}^{n} + \Delta\bar{t}\bar{\boldsymbol{u}}_\mathrm{p}, \tag{4.15a}$$

$$\bar{\boldsymbol{u}}_\mathrm{p}^{n+1} = \left[1 - \left(1 + Re_\mathrm{p}^{n\,0.687}\right)\frac{\Delta\bar{t}}{\tau}\right]\bar{\boldsymbol{u}}_\mathrm{p}^{n} + \Delta\bar{t}\Phi(\bar{\boldsymbol{U}}_\mathrm{f}^{n}, \frac{\mathrm{d}\bar{\boldsymbol{U}}_\mathrm{f}^{n}}{\mathrm{d}\bar{t}}, \bar{\boldsymbol{\nabla}}\bar{p}^{n}, Re_\mathrm{p}^{n}). \tag{4.15b}$$

Thus, a sufficient condition for the scheme stability is

$$\Delta\bar{t} < 2\tau = \frac{1}{9}(\rho^+ + C_\mathrm{m})R^2 Re. \tag{4.16}$$

Interpolation and capture criterion

The integration requires, at each time step, the fluid velocity and pressure at the particle position. It is necessary then to find the element hosting the particle to interpolate these variables. We used the particle tracer algorithm for unstructured grids proposed by Löhner and Ambrosiano [127]. It searches recursively, neighbour to neighbour, the new host element in the vicinity of the known previous one [128]. Having calculated the new position of the particle, the code checks if this latter hits the cylinder boundary, as a result of which it is

considered as captured. We refer to this capture definition as the *solid contact criterion*. The reader is invited to see the details of the particle tracer algorithm and the implementation of the solid contact criterion in appendices A and B.

Example of trajectories

An example of particle advection simulation is shown in Figure 4.4. We simulated the trajectories of two particles in a flow at $Re = 100$ around a cylinder undergoing VIV with $U_\mathrm{r} = 5$. Before $\bar{t} = 2.6$, the two particles follow a relatively straight path. The instant $\bar{t} \approx 2.6$ represents a transition in the trajectory behaviour, and reveals the outcome of each particle. On the one hand, the red upper particle succeeds in drifting upwards, far enough form the cylinder to escape capture. It enters a region of negative vorticity (blue in Figure 4.4), acquires momentum, then crosses the cylinder. The blue lower particle, on the other hand, slows down because it meets the stagnation point of the flow. From $\bar{t} = 3.7$ until its capture at $\bar{t} = 5.6$, it remains too close to the cylinder, following its downward motion, then ends up hitting its edge.

Figure 4.5 shows the time evolution of the ratios of the pressure load and added mass force to the drag norms. We see that the hydrodynamic forces preserve the same proportions to each other $||\boldsymbol{F}_\mathrm{P}|| \,/\, ||\boldsymbol{F}_\mathrm{D}|| \approx 0.66$ and $||\boldsymbol{F}_\mathrm{A}|| \,/\, ||\boldsymbol{F}_\mathrm{D}|| \approx 0.33$ before $\bar{t} = 2.6$. After that, these ratios drop when the non-captured particle enters the negative vorticity region and crosses the cylinder ($\bar{t} \approx 3.4$). The drag becomes two times and twenty times greater than the pressure load and the added mass force respectively. At this same time, the captured particle observes an opposite action: both ratios peak, with the pressure load being eight times higher than, and the added mass force almost equal to the drag. This peak in ratios occurs when the particle is near the stagnation point, and its velocity relative to the fluid takes the lowest value $\left|\left|\bar{\boldsymbol{u}}_\mathrm{p} - \bar{\boldsymbol{U}}_\mathrm{f}\right|\right| \approx 10^{-3}$ as depicted in Figure 4.6. The particle then immerses into the boundary layer of the upper part of the cylinder around $\bar{t} \approx 3.7$. We see that, between $\bar{t} = 3.7$ and 4.5, the drag catches up with the pressure load while the added mass effect dwindles. As the cylinder starts to move upwards ($\bar{t} \approx 4.5$), the gap between the pressure load and the drag widens again until the particle finishes up by being intercepted at $\bar{t}_\mathrm{c} = 5.6$.

Finally, one thing to mention is that the particle-based Reynolds number stays always below $Re_\mathrm{p} \approx 6 \times 10^{-2}$ for both captured and non-captured particles, as represented in Figure 4.6. This finding led us to derive an alternative method for trajectory calculation, which we invite the reader to look over in appendix C.

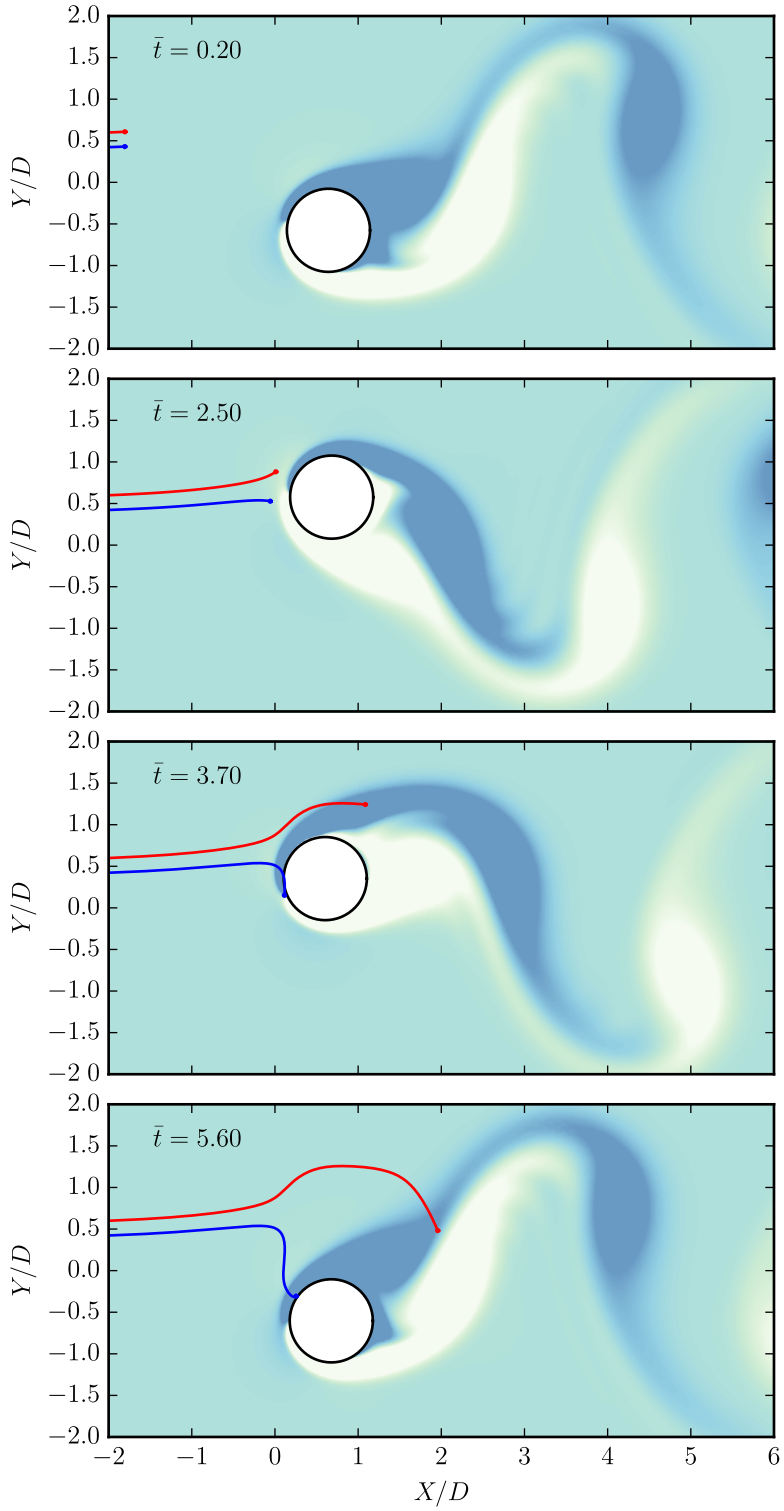

Figure 4.4 Snapshots of the trajectory of particles having a diameter ratio $R = 0.031$ advected by a flow at $Re = 100$ and $U_{\mathrm{r}} = 5$. After escaping the capture, the red particle enters in the region of negative vorticity ($\bar{t} = 3.7$, dark blue), as a result of which it deviates downwards ($\bar{t} = 5.6$). On the other hand, as soon as it approaches the cylinder, the blue particle slows down, meets the stagnation point ($\bar{t} = 3.7$) and enters inside the boundary layer. It is worth to mention that this particle remains confined within the boundary layer, and does not touch the cylinder edge until $\bar{t} = 5.6$.

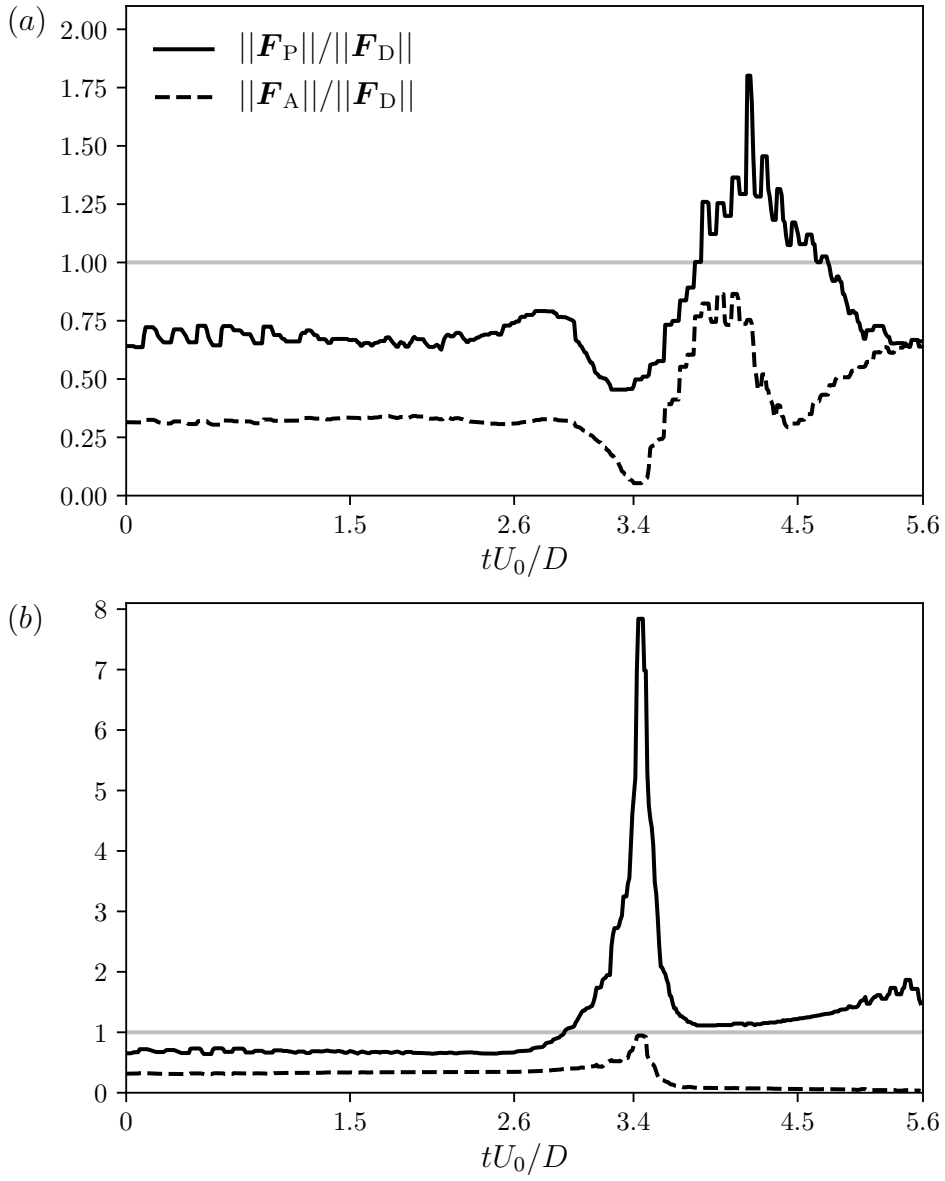

Figure 4.5 Evolution of the norms of the pressure load and the added mass force normalised by the norm of the drag for the (a) non-captured and (b) captured particles.

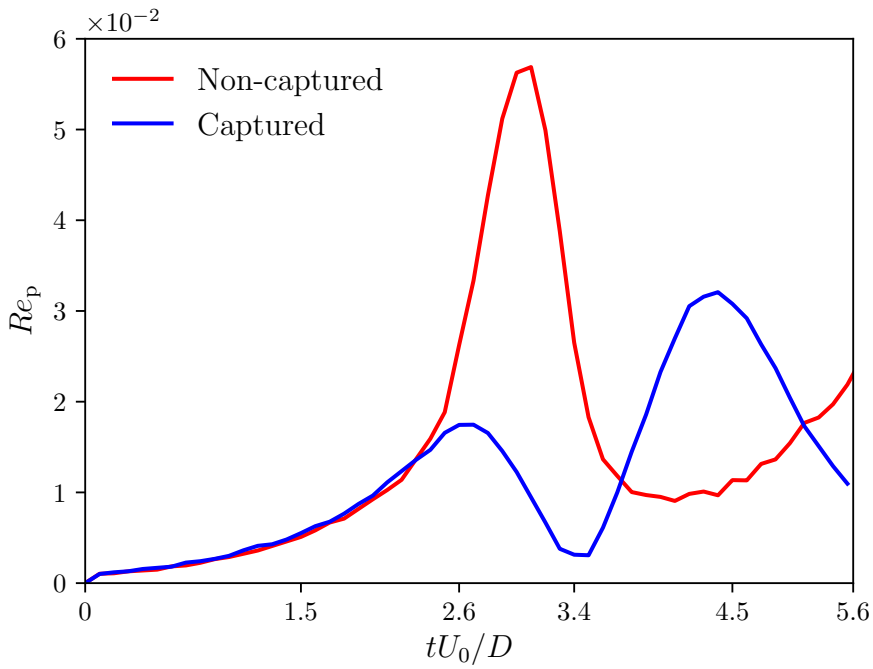

Figure 4.6 Particle-based Reynolds number versus time. Since $Re_\mathrm{p} = ReR\left|\left|\bar{\boldsymbol{u}}_\mathrm{p} - \bar{\boldsymbol{U}}_\mathrm{f}\right|\right|$, this graph also gives the profile of the variation of the particle relative velocity (in this example $ReR = 100 \times 0.031 = 3.1$).

4.3 Capture rate

With the ability to simulate particle trajectories and detect the captured ones, we tackle the rate at which the cylinder intercepts them. The capture rate $\dot{N}$ is the number of particles that the cylinder captures per unit time. As illustrated in Figure 4.7, the particle that would be ultimately captured enters necessarily through an opening that we call the *capture window*. Thereby, the capture rate also equals the flux of particles through this capture window

$$\dot{N} = C_0 U_0 e. \tag{4.17}$$

Here C_0 is the particle concentration per unit length ($\#/\mathrm{m}^2$), which we assume constant and uniform, and e is the length of the capture window.

4.3.1 Calculation strategy

Automated dichotomy

From the definition (4.17), we calculate the capture rate $\dot{N}$ through the length of the capture window e. As shown in Figure 4.7, the capture window is determined by the initial ordinates

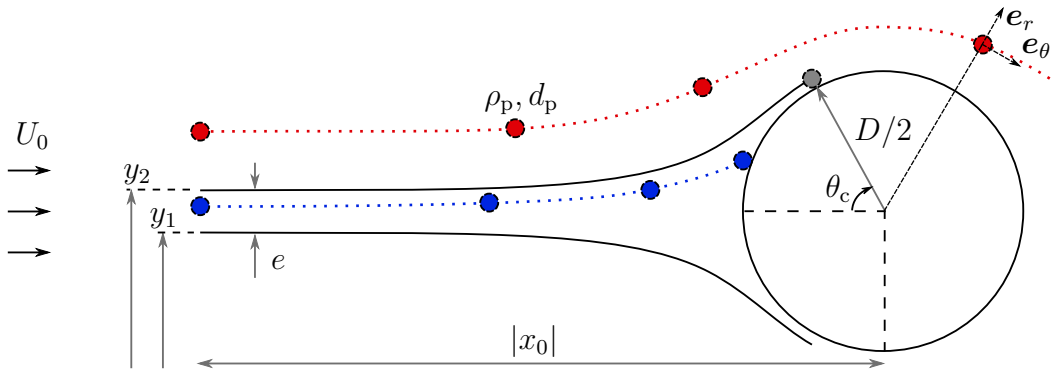

Figure 4.7 Schematics of particle advected by a flow around a fixed cylinder. Particles are launched from a distance $-x_0$ upstream from the the cylinder. Because it starts near the symmetry line, the blue particle is captured, whereas the red particle starts from a large y-position and succeeds in crossing the cylinder and escaping capture. The gray particle is the farthest particle that the cylinder intercepts. Its trajectory starts from the ordinate y_2, and defines the upper border of the capture domain. The length of the capture window is equal to $e = y_2 - y_1$, and θ_c represents the maximum angle of capture.

y_1 and y_2 of the farthest particles (in gray) that are intercepted in lower and upper sides of the cylinder, so its length is written as

$$e = y_2 - y_1. \tag{4.18}$$

First, we consider captured (blue) and non-captured (red) particles, launched from the same starting line $x_0 = -2$ upstream from the cylinder. Their initial positions, y^{c} and y^{nc}, are necessarily bounds of either border, say the upper one ($y^{\mathrm{c}} < y_2 < y^{\mathrm{nc}}$). Next, we release a third particle between the two previous ones, from the middle of their initial ordinates $y^{\mathrm{m}} = (y^{\mathrm{c}} + y^{\mathrm{nc}})/2$. If it escapes capture, then the upper border y_2 is necessarily between the initial ordinates of this new particle and the former captured one ($y^{\mathrm{c}} < y_2 < y^{\mathrm{m}}$). Our Python code [115] repeats this dichotomic process until it reaches a resolution of one thousandth of the particle diameter. An overview of the implementation of this method is given in Algorithm 4.1.

Temporal decomposition

The borders of the capture region are, in fact, varying periodically in time as a result of the vortex shedding and cylinder motion. Consequently, the capture rate is also periodic, to

Algorithm 4.1 Part of the automated dichotomy process calculating an approximation of ordinates $y_{1,2}$ of the farthest captured particle intercepted in the lower and upper sides of the cylinder.

Particle P^{c} starting from y^{c} is captured
Particle P^{nc} starting from y^{nc} escapes capture

while $|y^{\mathrm{nc}} - y^{\mathrm{c}}| > d_{\mathrm{p}}/1000$ **do**
  $y^{\mathrm{m}} = (y^{\mathrm{c}} + y^{\mathrm{nc}})/2$
  Simulate the trajectory of the particle P^{m} starting from y^{m}
  if P^{m} is captured **then**
    $y^{\mathrm{c}} \leftarrow y^{\mathrm{m}}$
  end if
  if P^{m} escapes capture **then**
    $y^{\mathrm{nc}} \leftarrow y^{\mathrm{m}}$
  end if
end while

 # If $y^{\mathrm{nc}} > y^{\mathrm{c}}$, it means that we found the ordinate y_2 of the upper farthest captured particle,
 # otherwise it is the ordinate y_1 of the lower farthest captured particle.
return y^{c}

which we propose the following time-dependent expression

$$\dot{N}(t) = \langle \dot{N} \rangle + \dot{N}_{\mathrm{a}} \sin\left(\frac{2\pi t}{T} + \varphi\right). \tag{4.19}$$

The governing period T depends on the state of the cylinder. If this latter is fixed, T is the vortex shedding period because it is the only periodic behaviour present in the system. If it vibrates, T is the period of the stream-wise — not transverse – motion of the cylinder. Indeed, the cylinder describes a lemniscate, such as the one in Figure 4.8, so it captures particles in the same way whether during the upper or the lower loop.

We calculate the capture rate at instants $t = 0$, $T/4$, and $T/2$, and determine the three unknowns in equation (4.19) from the following

$$\langle \dot{N} \rangle = \frac{\dot{N}(0) + \dot{N}(T/2)}{2}, \tag{4.20a}$$

$$\dot{N}_{\mathrm{a}} = \sqrt{\left[\dot{N}(0) - \langle \dot{N} \rangle\right]^2 + \left[\dot{N}(T/4) - \langle \dot{N} \rangle\right]^2}, \tag{4.20b}$$

$$\varphi = \arcsin\left(\frac{\dot{N}(0) - \langle \dot{N} \rangle}{\dot{N}_{\mathrm{a}}}\right). \tag{4.20c}$$

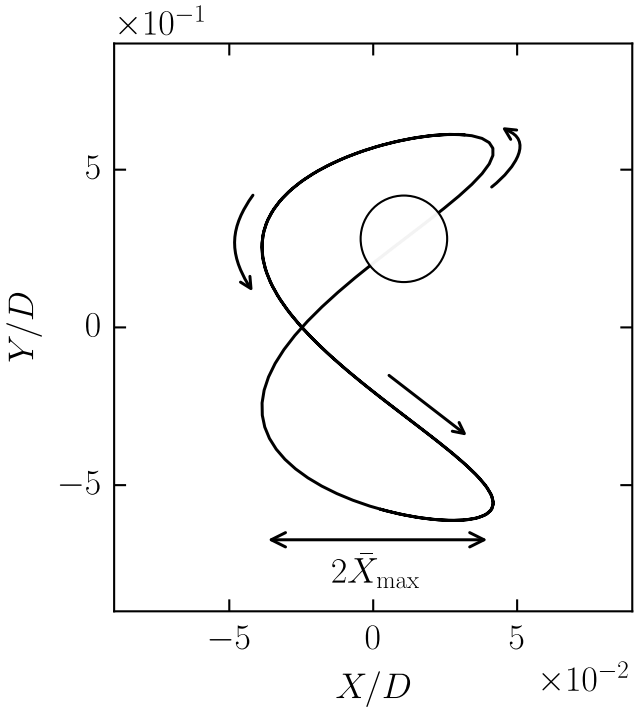

Figure 4.8 Example of a (centred) limit-cycle trajectory of a cylinder at $Re = 100$ and $U_\mathrm{r} = 5$. The X-axis, Y-axis, and cylinder diameter are not to scale.

4.3.2 Dimensional analysis

In addition to time, the capture rate is a function of the fluid, cylinder, and particle properties altogether

$$\dot{N}\ [\mathrm{s}^{-1}],\quad t[\mathrm{s}],\quad U_0\ [\mathrm{m\ s}^{-1}],\quad \rho_\mathrm{f}\ [\mathrm{kg\ m}^{-3}],\quad \mu_\mathrm{f}\ [\mathrm{kg\ m}^{-1}\mathrm{s}^{-1}],\quad D\ [\mathrm{m}],\quad k\ [\mathrm{N\ m}^{-1}],\quad m\ [\mathrm{kg}],$$
$$d_\mathrm{p}\ [\mathrm{m}],\quad \rho_\mathrm{p}\ [\mathrm{kg\ m}^{-3}],\quad C_0\ [\mathrm{m}^{-2}]. \tag{4.21}$$

The Buckingham Π theorem [129] states that $11 - 3 = 8$ independent dimensionless variables fully describe the problem. We choose them

$$\eta = \frac{\dot{N}}{C_0 U_0 D},\quad \bar{t} = \frac{D}{U_0},\quad Re = \frac{\rho_\mathrm{f} U_0 D}{\mu_\mathrm{f}},\quad R = \frac{d_\mathrm{p}}{D},\quad U_\mathrm{r} = \frac{U_0}{D}\sqrt{\frac{k}{m}},$$
$$\rho^+ = \frac{\rho_\mathrm{p}}{\rho_\mathrm{f}},\quad M = \frac{m}{\rho_\mathrm{f} D^2},\quad c_0 = C_0 D^2. \tag{4.22}$$

Therefore, the dimensionless capture rate η in our case reduces to the capture efficiency, according to definitions (1.17) and (1.18) (section 1.1.3, chapter 1), which itself equals the

dimensionless length of the capture window

$$\eta = \frac{\dot{N}}{C_0 U_0 D} = \frac{e}{D} = \bar{e}. \tag{4.23}$$

Owing to the decomposition in equation (4.19), the dimensionless time $\bar{t}$ intervenes only as an argument in the sine function

$$\eta = \langle \eta \rangle + \eta_\mathrm{a} \sin\left(\frac{2\pi \bar{t}}{\bar{T}} + \varphi\right), \tag{4.24}$$

with $\bar{T}$ being the dimensionless governing period. Thus, the variables $\langle \eta \rangle$, η_a, and φ are independent of $\bar{t}$. Moreover, for all simulations in the present work, we kept the mass ratio of the cylinder and the particle density ratio constant equal to $M = 1$ and $\rho^+ = 2$, beside a constant particle concentration ($c_0 = \text{constant}$). Henceforth, the remaining variables that determine the capture rate are the Reynolds number, the diameter ratio, and the reduced velocity

$$Re = \frac{\rho_\mathrm{f} U_0 D}{\mu_\mathrm{f}}, \quad R = \frac{d_\mathrm{p}}{D}, \quad U_\mathrm{r} = \frac{2\pi U_0}{D}\sqrt{\frac{m}{k}}, \tag{4.25}$$

and we write

$$\eta = \mathscr{F}(Re, R, U_\mathrm{r}). \tag{4.26}$$

CHAPTER 5 CASE OF A FIXED CYLINDER

We begin our study progressively from the case of a fixed cylinder. Although the reduced velocity is not defined for a motionless body, we assume that the cylinder is fixed in the asymptotic case when $U_\mathrm{r} \to 0$ (infinite spring stiffness). We introduce, therefore, the particle capture rate by a fixed cylinder as

$$\eta_\mathrm{fixed} = \lim_{U_\mathrm{r}\to 0} \eta = \mathscr{F}_0(Re, R). \tag{5.1}$$

5.1 Numerical results

We simulated the trajectories of particles of diameter ratios between $R = 0.008$ and 0.1, advected by flows at Reynolds numbers from $Re = 3$ to 300. The scheme in Figure 5.1 contrasts particles with the cylinder to have an idea of how small they are.

First, we evaluated the magnitude of the two terms in the temporal decomposition of the capture rate η in (4.24), namely the mean capture rate $\langle\eta\rangle_\mathrm{fixed}$ and the amplitude of the transient rate $\eta_\mathrm{a,fixed}$. Figure 5.2 shows the ratio $\eta_\mathrm{a,fixed}/\langle\eta\rangle_\mathrm{fixed}$ versus the Reynolds number for different particles. Since it is always less than 0.02, we consider that the sine function in equation (4.24) can be considered as a small fluctuation of the mean capture $\langle\eta\rangle_\mathrm{fixed}$. Therefore, in the ensuing sections, we will assume that $\eta_\mathrm{fixed} \approx \langle\eta\rangle_\mathrm{fixed}$ and present results of mean capture rate only.

Next, in order to see the influence of the particle size, we considered each flow with a specific Reynolds number Re and calculated the capture rate for the diameter ratios $0.008 \leq R \leq 0.1$. The results are displayed in Figure 5.3(a). For small particles $R \leq 0.05$, the mean capture rate varies as the square of the diameter ratio $\langle\eta\rangle_\mathrm{fixed} \sim R^2$ for all Reynolds numbers. Large particles $R \geq 0.05$ also follow the same power law, but only for low Reynolds numbers $Re < 50$. As Re increases, $\langle\eta\rangle_\mathrm{fixed}$ deviates more and more above $\sim R^2$. Recalling that vortices start to shed at $Re \approx 50$, the gap between the mean capture rate and the square variation in the diameter ratio, for large particles, becomes more pronounced as the von Kármán street establishes.

In Figure 5.3(b) we look at the variation of the mean capture rate with the Reynolds number for each single particle. We found that particles having $R \leq 0.031$ follow the power law in $\sim Re^{1/2}$ irrespective of the flow regime. As for the largest particles $R = 0.05$ and 0.1, the mean capture rate follows this law before $Re \leq 50$, then switches to a linear variation

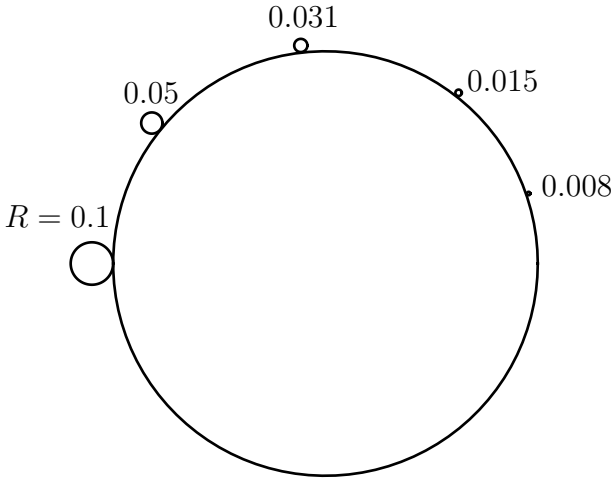

Figure 5.1 Schematics comparing particles and cylinder sizes. We recall that $R = d_\mathrm{p}/D$ is the diameter ratio.

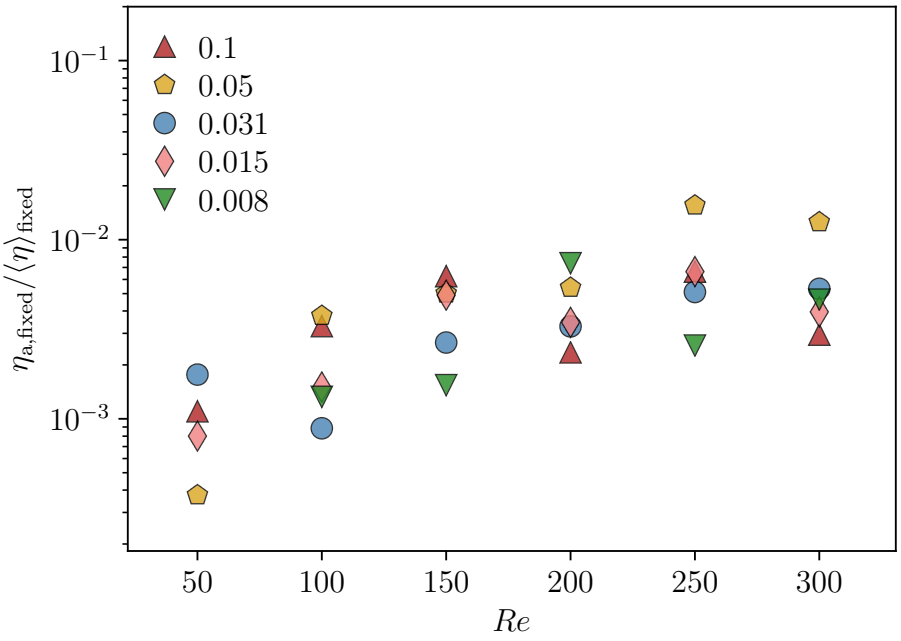

Figure 5.2 Ratio of the amplitude of the transient term $\eta_{\mathrm{a,fixed}}$ to the mean value $\langle\eta\rangle_{\mathrm{fixed}}$ of the capture rate by a fixed cylinder versus Reynolds number ($0.008 \leq R \leq 0.1$). The amplitude $\eta_{\mathrm{a,fixed}}$ represents only a small fluctuation that does not exceed 2% of $\langle\eta\rangle_{\mathrm{fixed}}$. For $Re < 50$, we found that $\eta_{\mathrm{a,fixed}} = 0$, so we did not plot it in the graph.

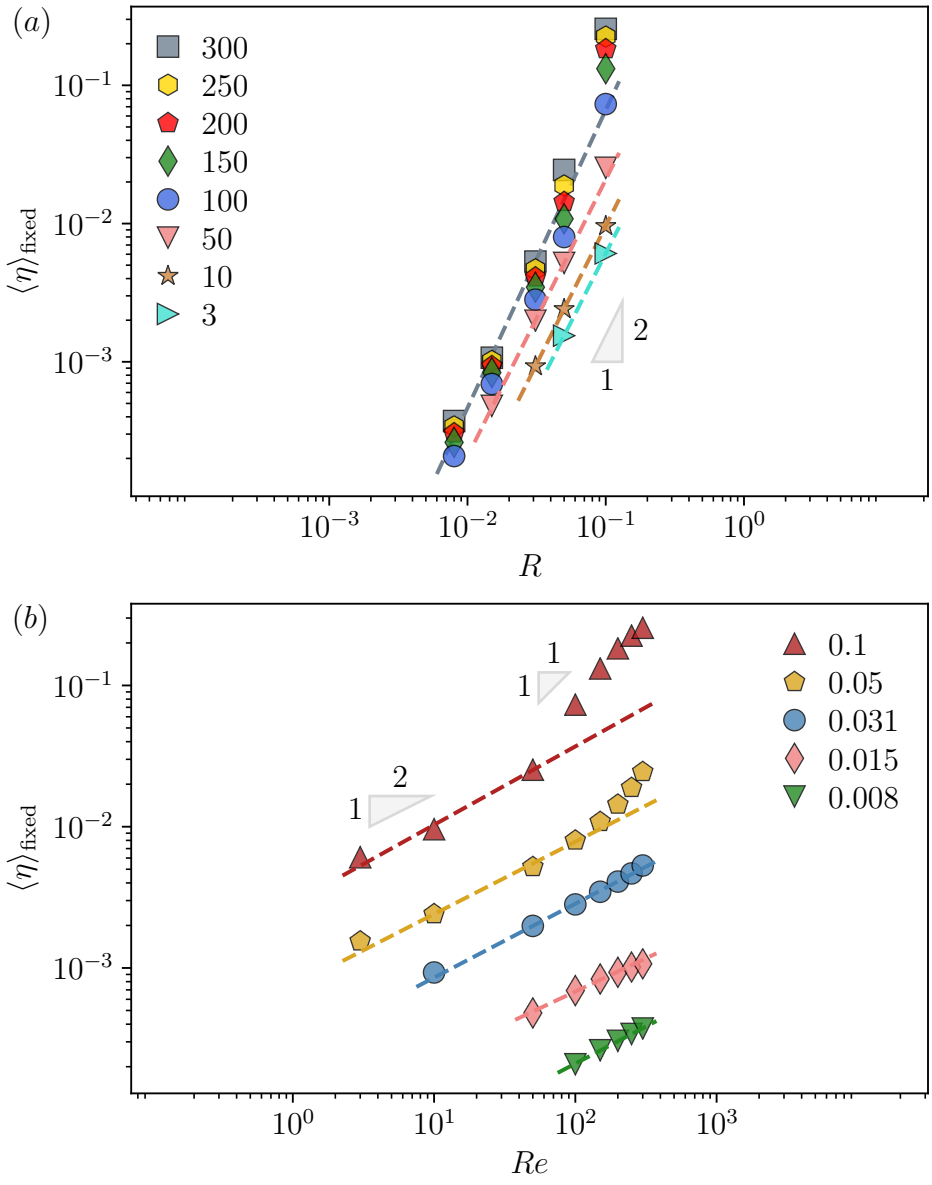

Figure 5.3 The mean capture rate for a fixed cylinder as a function of (a) the particle diameter ratio for $3 \leq Re \leq 300$, and (b) the Reynolds number for $0.008 \leq R \leq 0.1$. The dashed lines are power law fits, valid for specific ranges of data points listed in Tables 5.1 and 5.2.

Re	p	incertitude	r^2	R-validity
300	2.15	0.11	0.87	≤ 0.031
250	2.06	0.08	0.86	≤ 0.031
200	2.01	0.10	0.86	≤ 0.031
150	1.95	0.02	0.86	≤ 0.031
100	2.14	0.05	0.88	≤ 0.05
50	2.00	0.02	0.95	≤ 0.05

Table 5.1 Exponents p found by fitting $\sim R^p$ to numerical data points in Figure 5.3(a), for each Reynolds number Re.

R	p	incertitude	r^2	Re-validity
0.1	0.55	0.10	0.99	≤ 50
0.05	0.51	0.08	0.99	≤ 100
0.031	0.52	0.02	0.98	≤ 250
0.015	0.47	0.04	0.95	≤ 200
0.008	0.53	0.02	0.99	≤ 300
0.1	1.03	0.09	0.99	≥ 100
0.05	1.03	0.10	0.99	≥ 50

Table 5.2 Exponents p found by fitting $\sim Re^p$ to numerical data points in Figure 5.3(b), for each diameter ratio R.

$\langle\eta\rangle_{\text{fixed}} \sim Re^1$ after.

In summary, we found that the best power function fit of the mean capture rate yields ($r^2 = 0.99$, Figure 5.4)

$$\langle\eta\rangle_{\text{fixed}} = 0.38 R^{2.09} Re^{0.52} \tag{5.2}$$

as the Reynolds number and the diameter ratio verify $R^2 Re^{1/2} < 0.028$. This means that equation (5.2) is valid even for large particles provided the flow is viscous, and in inertial flows provided the particles are small.

5.2 Role of the boundary layer

5.2.1 Qualitative interpretation

Because the interception depends on the local state of the fluid close to the cylinder edge, we introduce the boundary layer as an important factor in the interception mechanism. In Figure 5.5 we drew the boundary layer thickness in the upper side of the cylinder for an inertial flow ($Re = 100$), and superimposed small and large particles on it. We see that the blue small particle $R = 0.015$ can be completely immersed into the boundary layer after

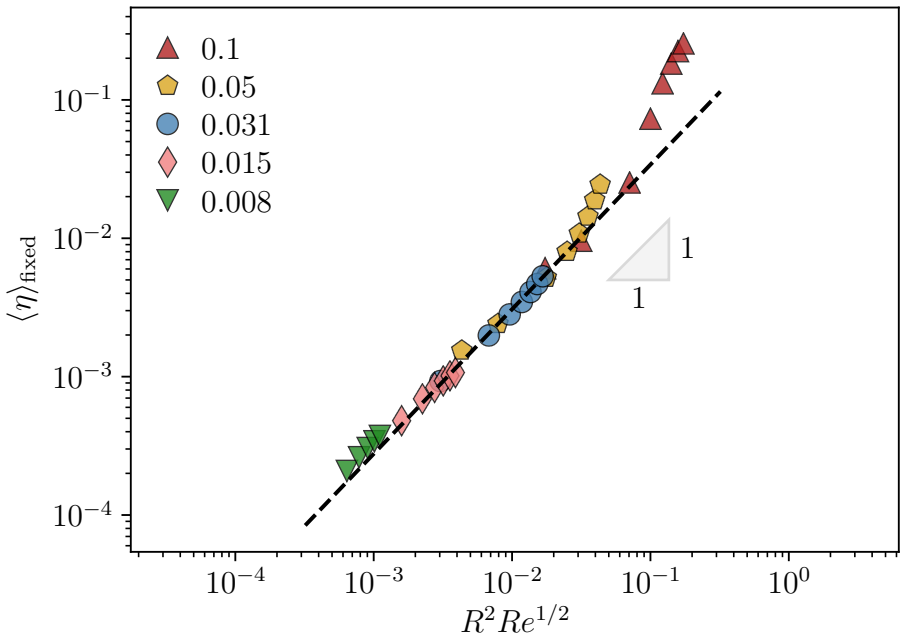

Figure 5.4 The mean capture rate for a fixed cylinder versus $R^2Re^{1/2}$ for $3 \leq Re \leq 300$ and $0.008 \leq R0.1 \leq$. The dashed line is the power function fit of data points for $R^2Re^{1/2} < 0.028$ ($r^2 = 0.99$): $\langle\eta\rangle_{\text{fixed}} = cR^aRe^b$ with $a = 2.09 \pm 0.06$, $b = 0.52 \pm 0.01$ and $c = 0.378 \pm 0.044$.

entering from near the stagnation point. Being inside, the particle decelerates and settles on the cylinder edge. Yet, only particles launched from a fine region around the symmetry line are able to reach the stagnation point and penetrate the boundary layer. Otherwise, they would deviate before approaching to the cylinder, like the red one in Figure 5.5(a). From this respect, the boundary layer 'shields' the cylinder from the majority of small particles, leading to a narrow capture window $e \ll D$, hence a low capture rate.

On the other hand, the particle with a diameter ratio of $R = 0.1$ has a size larger than the thickness of the boundary layer as shown in Figure 5.5(b). Therefore, even particles launched relatively far from the symmetry line preserve their momentum, deviate less, and impact the cylinder without any effect from the boundary layer. Thus, the capture window is wider and the capture rate higher. The boundary layer 'shield' cannot resist big particles.

Now that we focused on a single flow and described how the size of the particles is related to the capture rate, let us consider a single particle and see the influence of the Reynolds number on the interception process. In Figure 5.6 we plotted the pathlines of a viscous and inertial flows ($Re = 3$ and 100), which are representative of streamlines upstream from the cylinder assuming the flow there is steady enough. For the viscous flow, these pathlines diverge relatively far from the cylinder. Hence, particles ultimately captured are necessarily

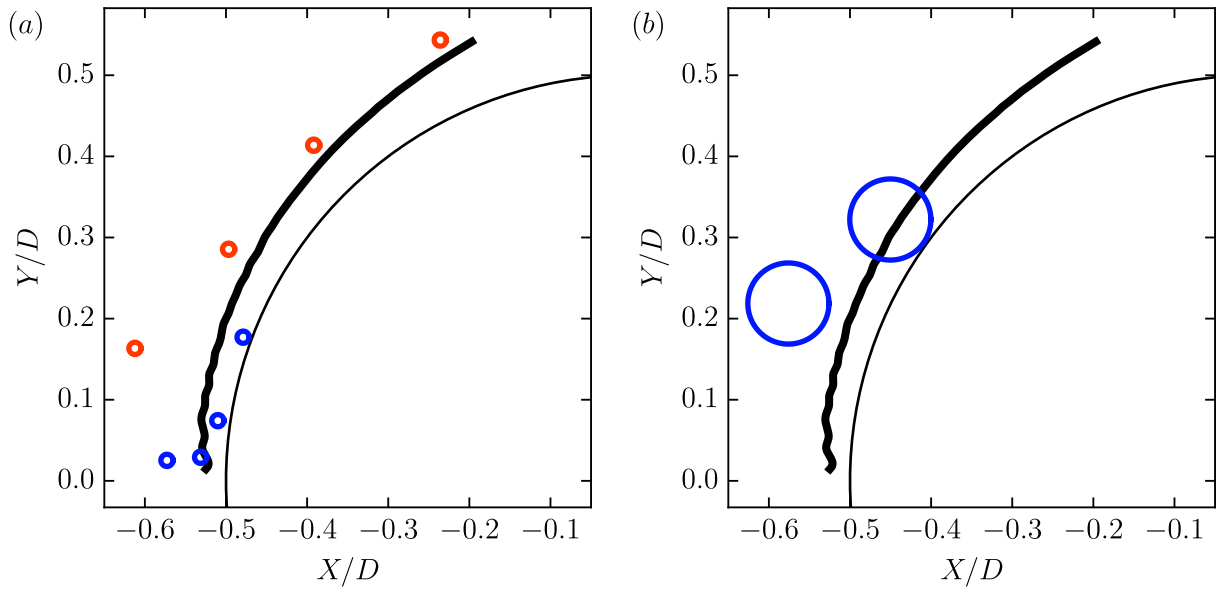

Figure 5.5 Numerical boundary layer thickness (bold black line) at $Re = 100$. (a) The blue particle of $R = 0.015$ is small enough to enter inside the boundary layer and remain within until capture. The red particle has the same size but launched far from the separation line. The boundary layer deviates it and prevents the cylinder from interception. (b) The particle of $R = 0.1$ is larger than the boundary layer, hence impacts the cylinder unaffected by the boundary layer.

launched from a narrow region around the symmetry line, say within the two pathlines (C) in Figure 5.6(a). If not, they would diverge early like the pathlines (A) or (B), and easily cross over the cylinder. For the inertial flow, conversely, as more fluid particles are carried in proximity of the cylinder edge, pathlines compress and diverge less. Consequently, even particles starting between the pathlines (B) and (C) in Figure 5.6(b), for example, will acquire enough momentum to travel straightly till the stagnation point, then immerse into the boundary layer and get intercepted. Thus, increasing the Reynolds number opens out more the capture window and augments the capture rate.

5.2.2 'Direct interception' versus 'Inertial impaction'

We found earlier in this chapter that the mean capture rate $\langle\eta\rangle_{\text{fixed}}$ follows the power law in equation (5.2) only when $R^2Re^{1/2} < 0.028$. To identify the behaviour of particle dynamics in this regime, we simulated the trajectory of the farthest captured particle having a small size of $R = 0.015$ in a flow at $Re = 100$ ($R^2Re^{1/2} = 0.002 < 0.028$). We examine the time evolution of the total hydrodynamic force applied on the particle (see equation (4.9b)), projected in the radial and angular directions $\bar{F}_{\text{total},r} = \bar{\boldsymbol{F}}_{\text{total}} \cdot \boldsymbol{e}_r$ and $\bar{F}_{\text{total},\theta} = \bar{\boldsymbol{F}}_{\text{total}} \cdot \boldsymbol{e}_\theta$, as represented in the top of Figure 5.7. We notice that the trajectory comprises three phases. From the starting line, the total force points almost radially away from the cylinder ($\bar{F}_{\text{total},r} > 0$ and $|\bar{F}_{\text{total},\theta}|/\bar{F}_{\text{total},r} \ll 1$), meaning that the particle travels almost straightly without deviation until it slows down as long as it gets close to the cylinder. We term this phase as the *approach*. The next phase, the *turn*, is when $\bar{F}_{\text{total},\theta}$ starts to increase and takes over $\bar{F}_{\text{total},r}$. The fluid slows down the particle near the stagnation point, then carries it sideways and curves its trajectory. After that, during the *settling* phase, while the particle enters the boundary layer, $\bar{F}_{\text{total},r}$ drops below zero and changes the sign. At that moment, the repulsive action of the hydrodynamic load transitions into an attracting action towards the cylinder, and the particle ends up being captured.

To check whether particle advection cases verifying the power law (5.2) share similar behaviour, we computed the trajectory of a larger particle $R = 0.05$ in a less inertial flow $Re = 50$, yet still in the power law regime ($R^2Re^{1/2} = 0.018 < 0.028$). As seen in the middle of Figure 5.7, this particle also goes through the approach, turn, and settling phases: the component $\bar{F}_{\text{total},r}$ peaks, decreases near zero, $\bar{F}_{\text{total},\theta}$ arises and takes over $\bar{F}_{\text{total},r}$, and finally immerses the particle inside the boundary layer. Since the particle drifts and settles down *directly* at the cylinder edge, we deduce that the regime where the power law (5.2) is valid corresponds to the 'direct interception' capture mode.

In contrast, we computed an advection case of the large particle $R = 0.1$ at $Re = 100$. Here

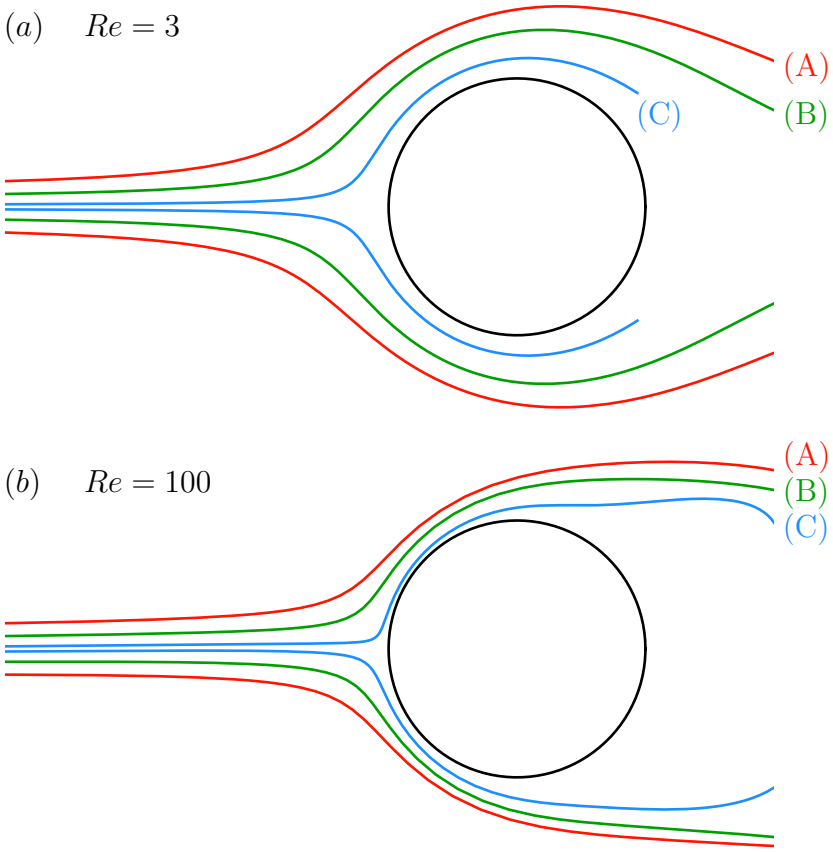

Figure 5.6 Pathlines illustrating the boundary layer thinning from (a) $Re = 3$ to (b) $Re = 100$. We assimilate streamlines to pathlines prior to the cylinder because the flow there is weakly transient. When the flow is viscous, the pathlines start to diverge far from the cylinder. Small particles should be released in a fine region between the pathlines (C) in order to be captured. When the flow is inertial, on the other hand, the pathlines compress and diverge close to the cylinder. In this case, even particles released between the pathlines (C) and (B) make their way until they hit the cylinder.

$R^2 Re^{1/2} = 0.1 > 0.028$ and the capture rate $\langle\eta\rangle_{\text{fixed}}$ stops following the power law (5.2). In the bottom of Figure 5.7, we first notice that this particle moves faster than the two smaller ones discussed above, and the durations of the three phases shrink. In the approach phase, $\bar{F}_{\text{total},\theta}$ starts climbing up while $\bar{F}_{\text{total},r}$ is still important, meaning that the particle deviates early and keeps a considerable radial momentum. We also point out that the trajectory is not sharply curved, and the particle travels as much distance during the turn phase as during the settling phase. Also, at the instant of capture, the magnitude of the radial and angular components of the total force take values $\bar{F}_{\text{total},r} \approx -0.3$ and $\bar{F}_{\text{total},\theta} \approx 0.7$, which are greater than in previous cases. These features are different from those pictured in earlier simulations, and show rather a particle moving rapidly and *impacting* the cylinder with high momentum. Again we deduce, by analogy, that the regime where the power law (5.2) underestimates the capture rate corresponds to the 'inertial impaction' capture mode.

We understood so far that the capture rate correlates positively with both the Reynolds number and the diameter ratio. But how can we explain the square variation in the diameter ratio? And why particles undergoing direct interception have a capture rate proportional to the square root of the Reynolds number, or in other words, to the inverse of the boundary layer thickness?

5.3 Power law derivation

In this section we propose an analytical derivation of the power law of the capture rate. We assume that the flow is steady upstream from the cylinder, and we discard any temporal variation. We start from the equation (1.18), and calculate the capture rate η through the length of the capture window e. This latter intervenes in the following balance equation by virtue of mass conservation on the control volume shown in Figure 5.8

$$\int_{(\mathcal{A})} \boldsymbol{U}_{\text{f}} \mathrm{d}\boldsymbol{n} + \int_{(\mathcal{S})} \boldsymbol{U}_{\text{f}} \mathrm{d}\boldsymbol{n} + \int_{(\mathcal{C})} \boldsymbol{U}_{\text{f}} \mathrm{d}\boldsymbol{n} + \int_{(\mathcal{B})} \boldsymbol{U}_{\text{f}} \mathrm{d}\boldsymbol{n} = 0. \tag{5.3}$$

The control volume is formed with: the capture window ($\mathcal{A}$), the trajectories ($\mathcal{S}$) of the outermost captured particles, the cylinder's arc of circle ($\mathcal{C}$) defined between the maximum capture angles $\pm\theta_{\text{c}}$, and the two segments ($\mathcal{B}$) linking the cylinder edge and particle centre. The vector $\mathrm{d}\boldsymbol{n}$ is the integration element pointing outwards.

Because of the no-slip condition at the cylinder edge, the integral over ($\mathcal{C}$) is equal to zero. Also, assuming that the particles follow exactly the streamlines, the integral over ($\mathcal{S}$) vanishes.

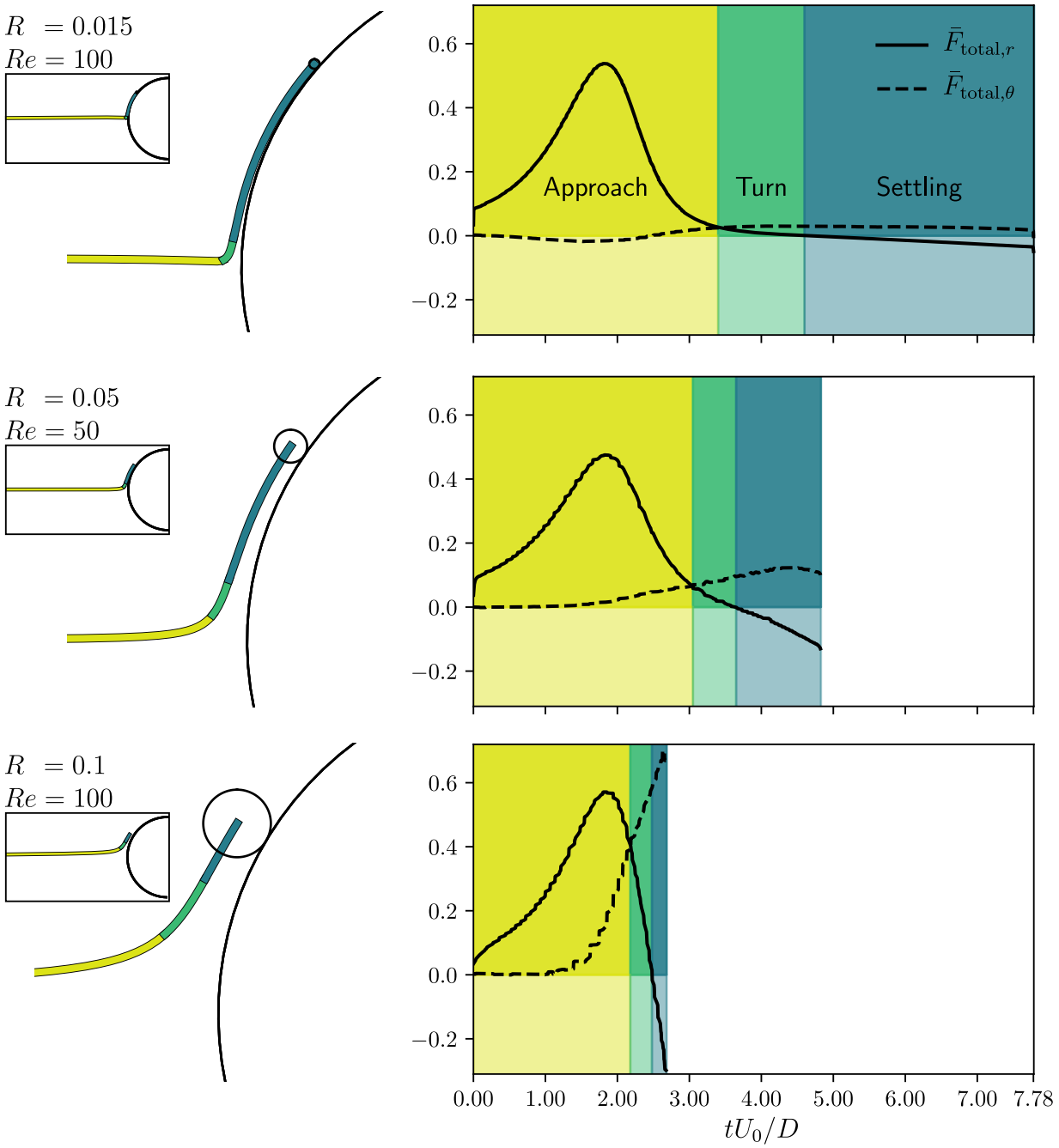

Figure 5.7 Time evolution of the dimensionless radial $\bar{F}_{\text{total},r}$ and angular $\bar{F}_{\text{total},\theta}$ components of the total hydrodynamic force applied on the outermost captured particles. The radial vector $\boldsymbol{e}_r$ points away from the cylinder and the angular vector $\boldsymbol{e}_\theta$ is clockwise (see Figure 4.7 for the polar frame definition). In the case of the particle $R = 0.015$ at $Re = 100$ (top), $\bar{F}_{\text{total},r}$ is positive during the approach phase (in yellow), meaning that it is repulsive. Meanwhile, $\bar{F}_{\text{total},\theta}$ is negligible, hence the particle keeps a straight path. In the turn phase (in green) we have $\bar{F}_{\text{total},\theta} > \bar{F}_{\text{total},r}$, and this latter keeps decreasing until it drops below zero at $\bar{t} \approx 4.6$. Subsequently, during the settling phase (in blue), the hydrodynamic force becomes attractive. Apart from arriving at the cylinder more rapidly, the forces evolution in the case $R = 0.05$ at $Re = 50$ (middle) shares the same features as above. However, for $R = 0.1$ at $Re = 100$ (bottom), since $\bar{F}_{\text{total},\theta}$ intersects with $\bar{F}_{\text{total},r}$ while this latter is still around its peak, the particle deviates early before getting close to the cylinder. Also, the force components take values of $\bar{F}_{\text{total},r} \approx -0.3$ and $\bar{F}_{\text{total},\theta} \approx 0.7$, which are larger than in previous cases.

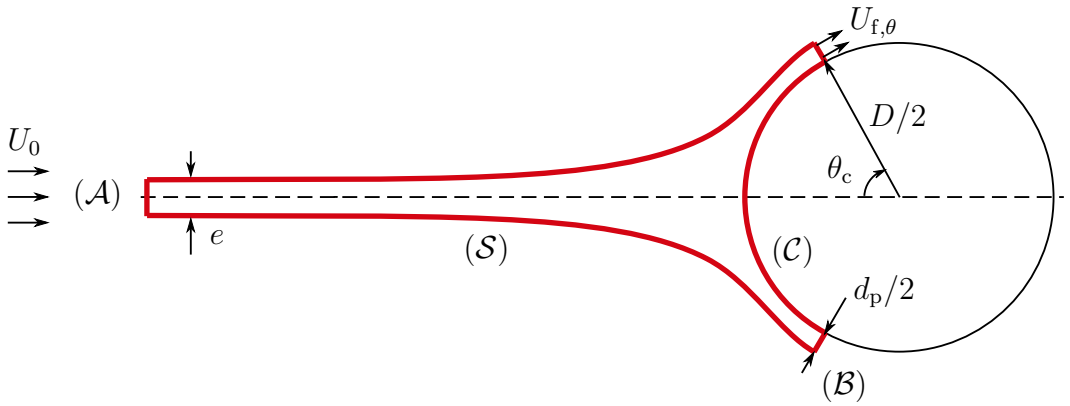

Figure 5.8 Control volume considered in equation (5.3) defining the capture window length. Here $U_{\mathrm{f},\theta}$ is the angular component of the fluid velocity, and θ_c the maximum angle of interception.

Therefore, we are left with

$$-eU_0 + 2\int_{D/2}^{D/2+d_\mathrm{p}/2} U_{\mathrm{f},\theta}\mathrm{d}r = 0, \tag{5.4}$$

with $U_{\mathrm{f},\theta}$ the angular component of the fluid velocity.

Now we introduce the stream function ψ and rewrite $U_{\mathrm{f},\theta}$ as

$$U_{\mathrm{f},\theta} = \frac{\partial\psi}{\partial r}. \tag{5.5}$$

Equation (5.4) becomes

$$eU_0 = 2\psi(D/2 + d_\mathrm{p}/2, \theta_\mathrm{c}), \tag{5.6}$$

considering that the cylinder edge is a streamline, i.e. $\psi(D/2, \theta) = 0$. Switching to dimensionless variables

$$\bar{\psi} = \frac{\psi}{U_0 D}, \quad \bar{e} = \frac{e}{D}, \tag{5.7}$$

and given the definition of η in equation (4.23), we get

$$\eta = \bar{e} = 2\bar{\psi}(1/2 + R/2, \theta_\mathrm{c}). \tag{5.8}$$

Next, assuming $R \ll 1$, we expand (5.8) to the second order in R around $1/2$

$$\eta \approx \bar{\psi}(1/2, \theta_\mathrm{c}) + \left(\frac{R}{2}\right)\left.\frac{\partial\bar{\psi}}{\partial\bar{r}}\right|_{1/2,\theta_\mathrm{c}} + \frac{1}{2}\left(\frac{R}{2}\right)^2\left.\frac{\partial^2\bar{\psi}}{\partial\bar{r}^2}\right|_{1/2,\theta_\mathrm{c}}. \tag{5.9}$$

Again, $\partial\bar{\psi}/\partial\bar{r}|_{\bar{r}=1/2} = 0$ due to the no-slip condition, and the cylinder edge is a streamline *per se*, so $\bar{\psi}|_{\bar{r}=1/2} = 0$. We obtain thus the quadratic variation in the diameter ratio

$$\eta \approx \frac{1}{8} R^2 \left.\frac{\partial^2 \bar{\psi}}{\partial \bar{r}^2}\right|_{1/2,\theta_c}. \tag{5.10}$$

Up to this stage, all previous models [10, 12, 13] agree with the same quadratic variation in the diameter ratio. Whereas they ended their analytical model at this step, here we push further our derivation and propose a new approach to get into the square root variation in the Reynolds number.

Since the particle diameter is too small compared to the cylinder ($d_p \ll D$), its curvature is much higher ($d_p^{-1} \gg D^{-1}$). In other words, the particle is so small that, once close enough to the cylinder edge, this latter appears like a flat plate. We could arguably suppose, hence, that the boundary layer of a cylinder has the same properties as for a plate, and use the analytical expression of the stream function [130]

$$\bar{\psi} = \sqrt{\frac{2\bar{x}}{Re}} f\left(\bar{y}\sqrt{\frac{Re}{2\bar{x}}}\right), \tag{5.11}$$

where f is solution of the Blasius equation. However, we decide to work with a new system of coordinates (θ, ρ) that transforms a flat plate into a circle, defined with a certain relation

$$x = x(\theta, \rho), \tag{5.12a}$$

$$y = y(\theta, \rho). \tag{5.12b}$$

The expression (5.11) is an inner expansion of the boundary layer solution to the order $O(1/Re)$, and it does not keep the same form just by simply inserting the new coordinate system (5.12) into (5.11) [107]. According to Kaplun's correlation theorem [131], we shall first choose a system of coordinates such that the flat plate defined by $(x, y = 0)$ should correspond to the circle of radius $D/2$ defined by $(\theta, \rho = 0)$, then use the following

$$x(\theta, \rho) \approx x(\theta, 0), \tag{5.13a}$$

$$y(\theta, \rho) \approx \rho \frac{\partial y}{\partial \rho}(\theta, 0), \tag{5.13b}$$

so that the stream function in the new system of coordinates becomes

$$\bar{\psi} = \bar{\psi}\left(x(\theta,0), \rho\frac{\partial y}{\partial \rho}(\theta,0)\right). \tag{5.14}$$

Let us consider the Joukowski transformation $\mathscr{J}$ [132]

$$z = \mathscr{J}(Z) = Z + \frac{(D/2)^2}{Z}, \tag{5.15}$$

and put

$$Z = (\rho + D/2)e^{i\theta}. \tag{5.16}$$

Then for a fixed ρ, the variable Z draws a circle of radius $\rho + D/2$ as θ goes through $[0, 2\pi]$. Replacing (5.16) in (5.15) we obtain

$$z = x + iy = \left(\rho + D/2 + \frac{(D/2)^2}{\rho + D/2}\right)\cos\theta + i\left(\rho + D/2 - \frac{(D/2)^2}{\rho + D/2}\right)\sin\theta, \tag{5.17}$$

yielding

$$x = x(\theta,\rho) = \left(\rho + D/2 + \frac{(D/2)^2}{\rho + D/2}\right)\cos\theta, \tag{5.18a}$$

$$y = y(\theta,\rho) = \left(\rho + D/2 - \frac{(D/2)^2}{\rho + D/2}\right)\sin\theta. \tag{5.18b}$$

Here we see that $\rho = 0$, which corresponds to the circle of radius $D/2$, leads to $y = 0$, hence the first condition of Kaplun's theorem is verified. The transformation (5.18) is illustrated in Figure 5.9.

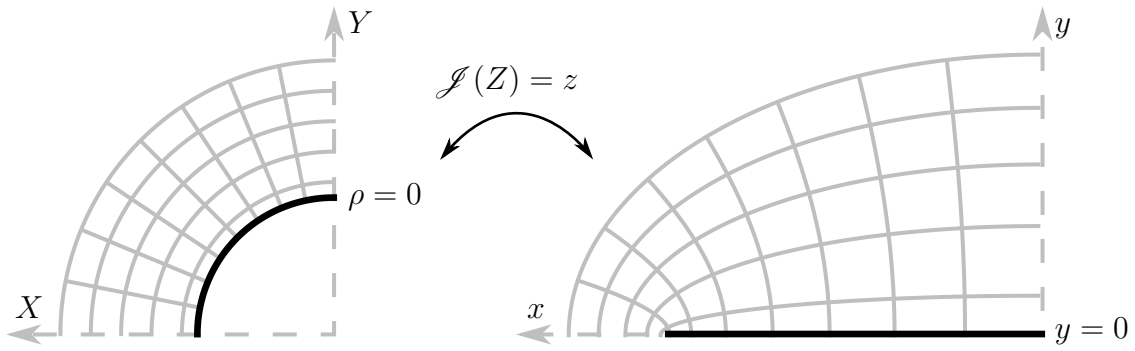

Figure 5.9 Joukowski transformation as defined in equations (5.15) and (5.18). The circle $\rho = 0$ in the (X, Y)-plane corresponds to the flat plate $y = 0$ in the (x, y)-plane.

Expanding around $\rho = 0$ we get

$$x(\theta, \rho = 0) = \cos\theta, \tag{5.19}$$

$$\rho\frac{\partial y}{\partial r}(\theta, \rho = 0) = 2\rho\sin\theta, \tag{5.20}$$

which reads in dimensionless variables

$$\bar{x}(\theta, \bar{\rho} = 0) = \cos\theta, \tag{5.21a}$$

$$\bar{\rho}\frac{\partial \bar{y}}{\partial \bar{\rho}}(\theta, \bar{\rho} = 0) = 2\bar{\rho}\sin\theta. \tag{5.21b}$$

Therefore, replacing (5.21) in (5.14) we get

$$\bar{\psi} = \bar{\psi}\left(\bar{x}(\theta, 0), \bar{\rho}\frac{\partial \bar{y}}{\partial \bar{\rho}}(\theta, 0)\right) = \sqrt{\frac{2\cos\theta}{Re}}f\left(2\bar{\rho}\sin\theta\sqrt{\frac{Re}{2\cos\theta}}\right). \tag{5.22}$$

Finally, coming back to the original variable $\bar{r} = \bar{\rho} + 1/2$, and since $\partial^2/\partial\bar{r}^2 = \partial^2/\partial\bar{\rho}^2$, the second derivative of the stream function at the capture location of the outermost particle $\bar{r} = 1/2$, $\theta = \theta_c$ is

$$\left.\frac{\partial^2\bar{\psi}}{\partial\bar{r}^2}\right|_{1/2,\theta_c} = (2\sin\theta_c)^2\sqrt{\frac{Re}{2\cos\theta_c}}f''(0), \tag{5.23}$$

whence, from (5.10)

$$\eta \approx \frac{\sin^2\theta_c f''(0)}{2\sqrt{2}\cos^{1/2}\theta_c}Re^{1/2}R^2. \tag{5.24}$$

With $f''(0) = 0.4696$ [107, 130], and taking for instance $\theta_c \approx 80°$, we find

$$\eta \approx 0.38Re^{1/2}R^2. \tag{5.25}$$

We got hence the same scaling (5.2) as in the curve fit of numerical data in Figure 5.4. We understand then, from this theoretical derivation, that the quadratic variation in the diameter ratio and exponent 1/2 in the Reynolds number are related to the smallness of particles and the effect of the boundary layer thickness on the capture process, as qualitatively described in section 5.2.1.

CHAPTER 6 CASE OF A VIBRATING CYLINDER

After revealing the influence of the Reynolds number and diameter ratio on the capture rate for a fixed cylinder, in this chapter we let the cylinder free to oscillate in cross-flow and in-line directions, and study how the motion affects the interception of particles.

6.1 Numerical results

We present simulation results of particles having diameter ratios between $R = 0.015$ and 0.1, advected by flows of Reynolds numbers from $Re = 50$ to 200. Even though VIV appear for Reynolds numbers as small as $Re = 20$ [74], we discarded the cases $20 \leq Re < 50$ because the vibration amplitude is too small to affect the capture rate. We varied the spring stiffness of the cylinder so that the reduced velocity takes values $1 \leq U_{\mathrm{r}} \leq 13$.

Similarly to the previous chapter, we compare first the mean capture rate $\langle\eta\rangle$ and the amplitude of the transient rate η_{a} in the temporal decomposition of the capture rate in equation (4.24). As seen in Figure 6.1, the ratio $\eta_{\mathrm{a}}/\langle\eta\rangle$ is less than 0.1 for small and large reduced velocities, and does not exceed 0.2 at lock-in $U_{\mathrm{r}} \sim 5$ (with the exception of four outliers). Although we cannot neglect the temporal variation in η, unlike in the case of a fixed cylinder, we chose to dedicate this chapter for the mean capture rate only, as we aim to depict how vibrations influence the capture process overall.

Figure 6.2 shows the mean capture rate $\langle\eta\rangle$ as a function of the reduced velocity U_{r}. We see that $\langle\eta\rangle$ is a bell-shaped function of the reduced velocity. It starts from almost the same value as for a fixed cylinder ($U_{\mathrm{r}} \sim 1$), peaks at lock-in ($U_{\mathrm{r}} \sim 5$), then decreases down for high reduced velocities. To evaluate the benefit that the vibration brings to particle interception, we define the gain in capture rate δ as the relative difference between capture rates by vibrating and fixed cylinders

$$\delta = \frac{\langle\eta\rangle - \langle\eta\rangle_{\mathrm{fixed}}}{\langle\eta\rangle_{\mathrm{fixed}}}. \tag{6.1}$$

As shown in Figure 6.3, at lock-in ($U_{\mathrm{r}} \sim 5$), the gain in capture δ takes values from 20% to 40% depending on the particle size and Reynolds number. Moreover, as it is the case for the mean capture $\langle\eta\rangle$, the gain δ also varies significantly with the reduced velocity U_{r}. This fact suggests that a cylinder kinematic variable must intervene in the value of δ. Let us find out this hidden variable.

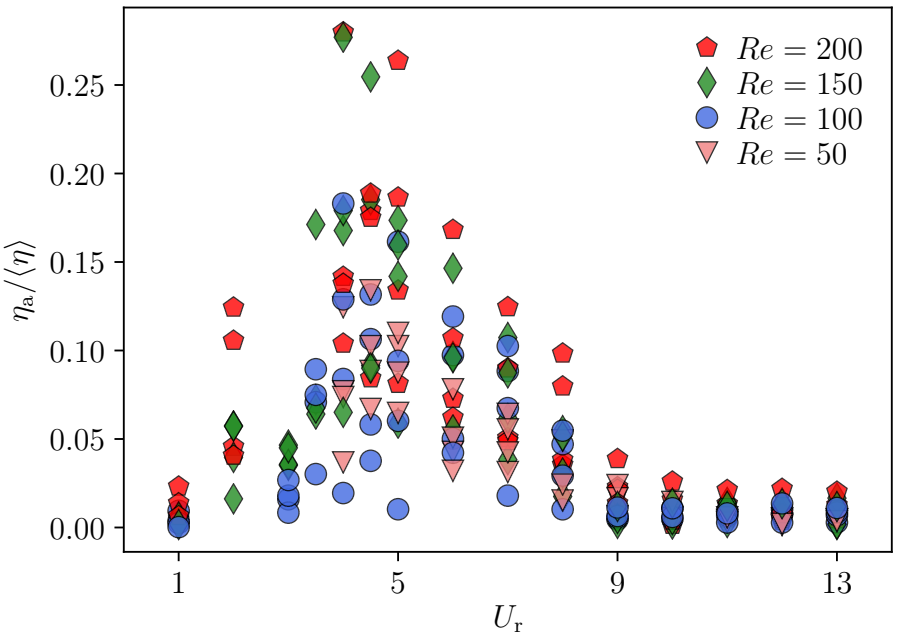

Figure 6.1 Ratio of the amplitude of the transient term $\eta_{a,fixed}$ to the mean value $\langle\eta\rangle_{fixed}$ of the capture rate by a vibrating cylinder versus reduced velocity for diameter ratios $0.015 \leq R \leq 0.1$ and Reynolds numbers $50 \leq Re \leq 200$.

6.2 Amplitude responses

We start by investigating the link between the gain δ and the amplitude response of the cylinder. Figure 6.4 shows the dimensionless responses of the transverse and stream-wise amplitudes of the cylinder, denoted $\bar{Y}_{max}$ and $\bar{X}_{max}$. The curves of δ, $\bar{Y}_{max}$, and $\bar{X}_{max}$ with U_r look very similar: they all peak at lock-in, and decrease for small and large reduced velocities. Indeed, Figure 6.5 shows that δ is positively correlated with $\bar{Y}_{max}$ and $\bar{X}_{max}$. The vibrating cylinder captures 40% more particles than its fixed counterpart for $\bar{Y}_{max} \sim 0.7$ and $\bar{X}_{max} \sim 5 \times 10^{-2}$.

This result is intuitive since a cylinder with large $\bar{Y}_{max}$ filters a wider cross-flow space and is more likely to catch particles. Similarly, a cylinder with a large $\bar{X}_{max}$ has more space to accelerate against the stream and reach an important counter-current velocity (in fact, the maximum stream-wise span and speed are proportional owing to the periodic motion, $\bar{X}_{max} \propto d\bar{X}_{max}/d\bar{t}$). As a consequence, particles get into the cylinder with a higher relative speed, hence hit it more often.

We mention, nonetheless, that the cylinder scores an overall loss in capture for $U_r > 9$ even in the presence of vibration, in the detrimental zone $0 < \bar{Y}_{max} \lesssim 0.3$ and $0 < \bar{X}_{max} \lesssim 8 \times 10^{-3}$.

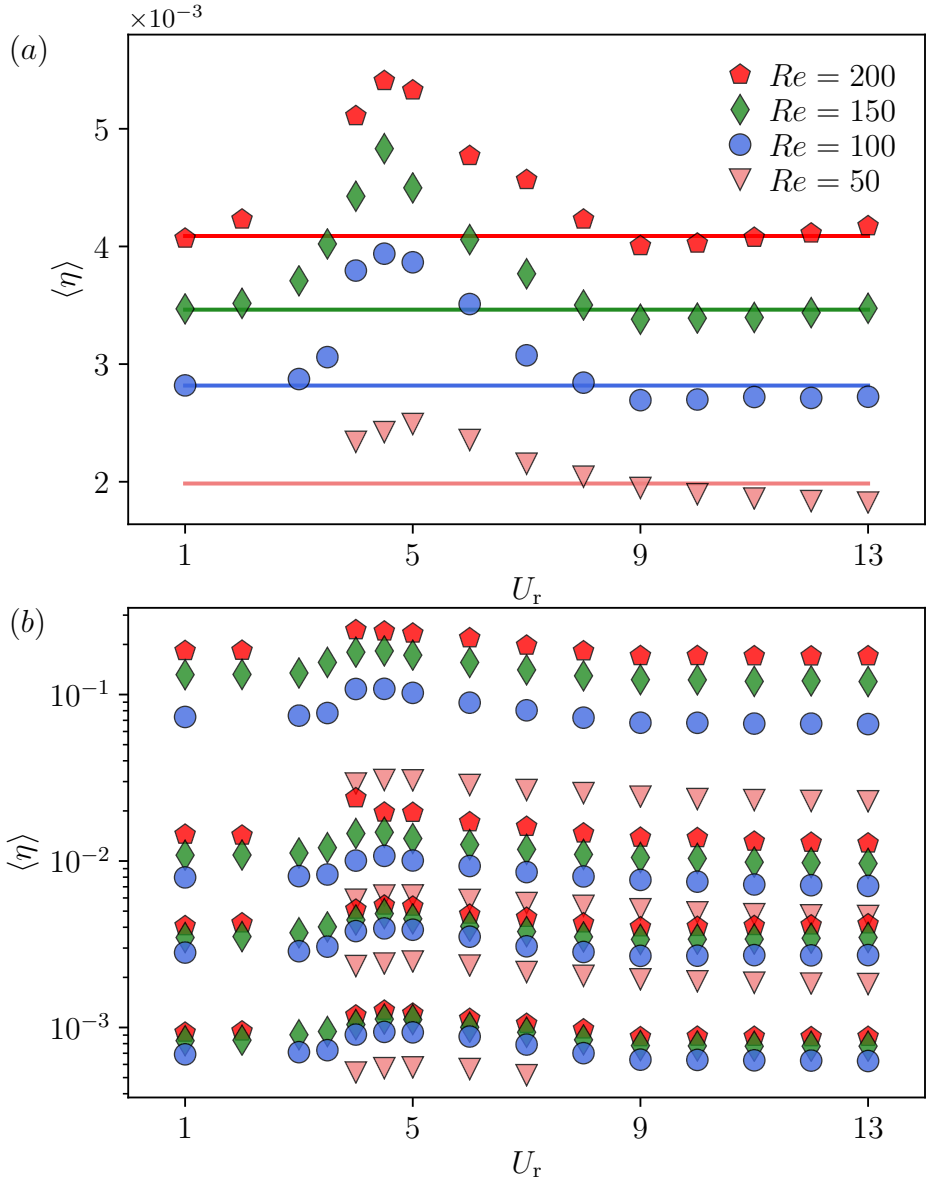

Figure 6.2 Mean capture rate versus the reduced velocity for (a) the particle $R = 0.031$ and (b) all particles, in fluid flows of Reynolds numbers $50 \leq Re \leq 200$. The solid horizontal line for each Reynolds number in (a) is the mean capture rate for a fixed cylinder $\langle \eta \rangle_{\text{fixed}}$.

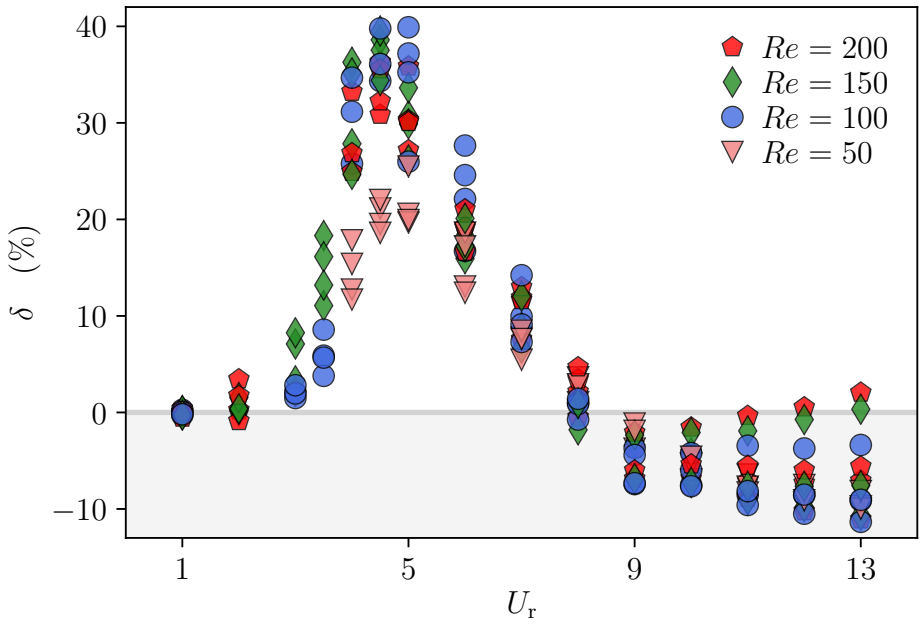

Figure 6.3 Gain in capture rate versus reduced velocity for all particles $R = 0.1$, 0.05, 0.031, and 0.015 in fluid flows of Reynolds numbers $50 \leq Re \leq 200$.

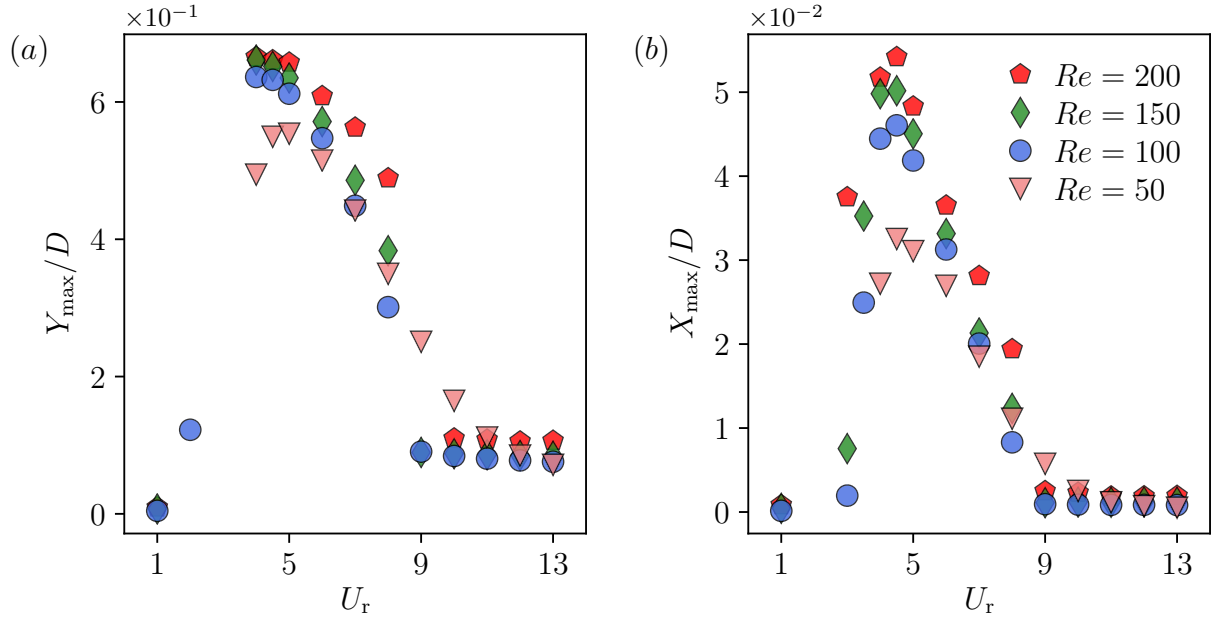

Figure 6.4 Response of (a) the transverse and (b) the stream-wise amplitudes

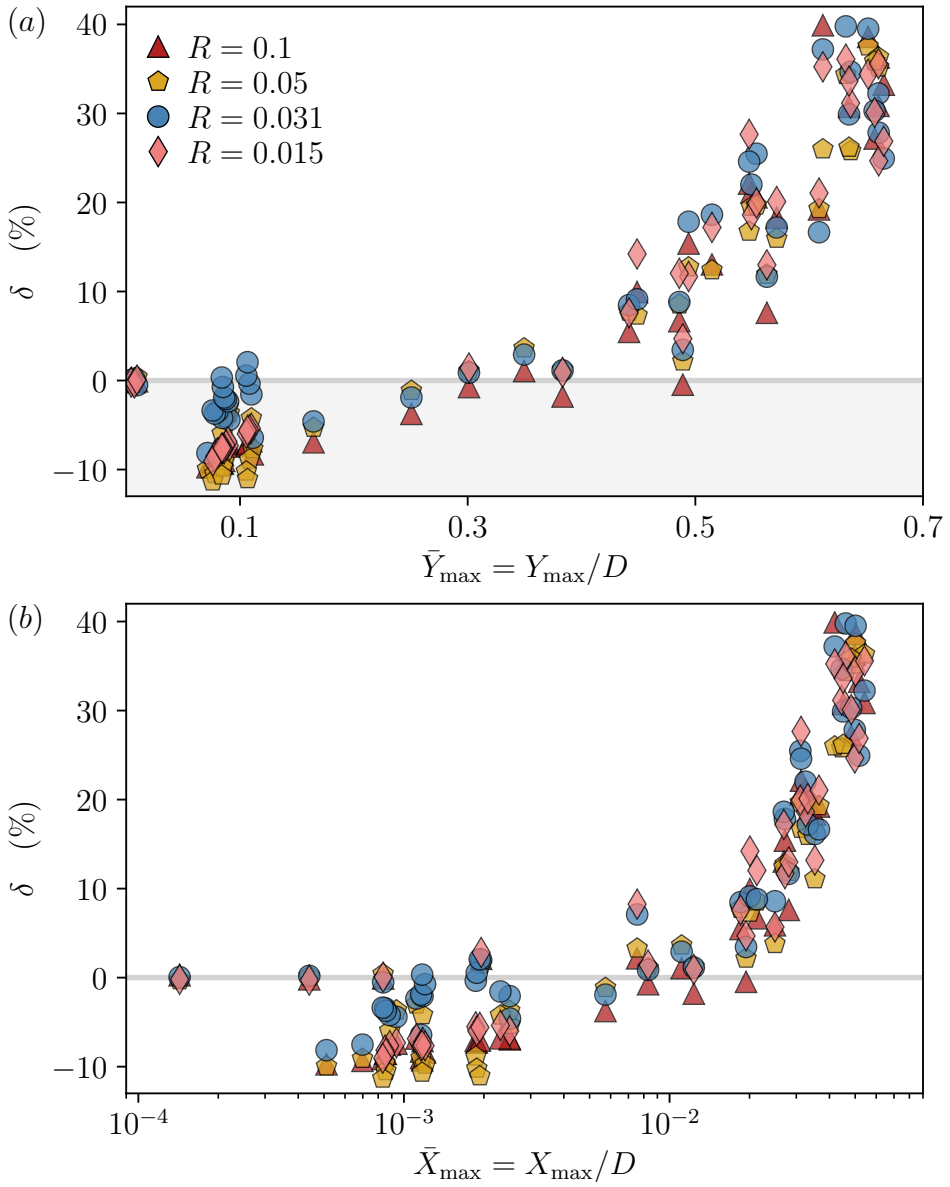

Figure 6.5 Gain in capture rate as a function of the (a) transverse and (b) stream-wise amplitude of the cylinder. The x-axis in (b) is logarithmic to visualise better the staggered data points.

One way to explain this finding is that while U_r increases, the transverse oscillation of the cylinder slows down, and its period becomes larger than the characteristic time of particle advection. Particles then see a cylinder that switches places up and down slowly, staying a long time in either side, hence giving them the chance to escape capture. For this reason, the cylinder misses several interception events, so it would be better if it stayed fixed, or at least in a quasi-steady state $U_\mathrm{r} > 20$ [15]. From this description, we infer that the profiles of the $\delta - U_\mathrm{r}$ curves would have in common an ascending phase ($0 < U_\mathrm{r} < 5$), a peak at lock-in ($U_\mathrm{r} \approx 5$), a descending phase ($5 < U_\mathrm{r} < 9$), a detrimental regime below zero ($9 < U_\mathrm{r} < 20$), and a plateau towards zero beyond the quasi-steady state ($U_\mathrm{r} > 20$).

In the following sections we dig into kinematic parameters other than Y_max and X_max that characterise the capture rate.

6.3 Shape of the lemniscate

For a two-degree-of-freedom motion, the limit-cycle trajectory of a cylinder undergoing VIV is a lemniscate (Figure 6.6). In this section, we further our analysis and analyse how the shape of this lemniscate affects the capture rate.

6.3.1 Slenderness

We have seen that the relative capture rate increases with the amplitude responses of the cylinder. Whereas Y_max and X_max give the extension of the lemniscate, in this section we combine them into a single parameter $\gamma = Y_\mathrm{max}/X_\mathrm{max}$ that we name the *slenderness* ratio of the lemniscate.

Figure 6.7 shows that the gain in capture is a decreasing function of the slenderness ratio. A cylinder with a thin lemniscate (high γ) travels the majority of its limit-cycle trajectory normal to the flow and spends only little time in-line. Thereby, the relative speed of particles with respect to the cylinder does not increase much, and the capture rate remains low. A cylinder with an extended lemniscate (low γ), conversely, spends a longer time travelling against the flow, hence it collects more particles.

Lemniscates with the same slenderness do not necessarily travel against the flow in the same way. We will see that the lemniscate has another geometrical property that is also important to consider in the capture process.

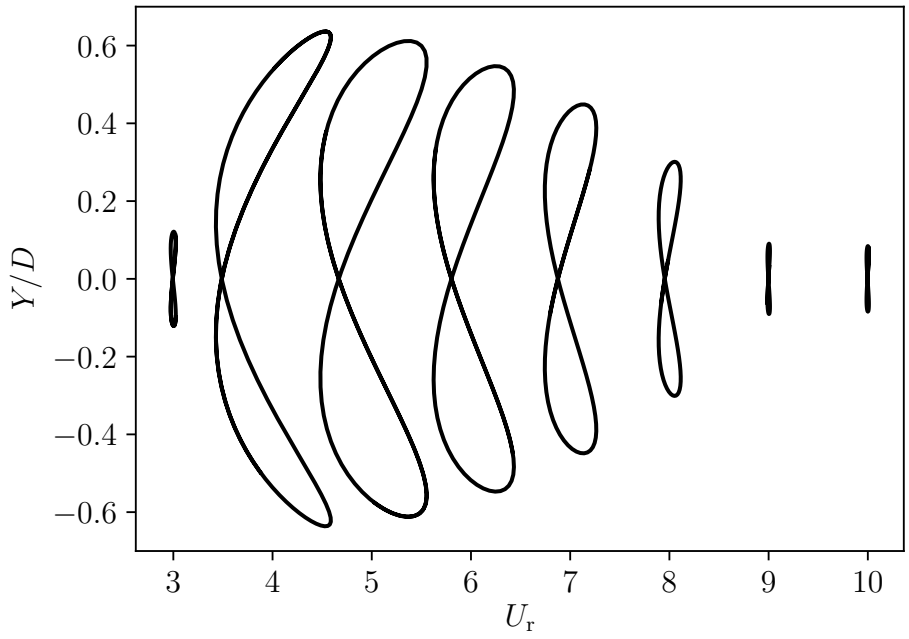

Figure 6.6 Lemniscate trajectories of the cylinder versus reduced velocity at $Re = 100$. The X-span of each lemniscate is magnified ≈ 13 times to elucidate the geometrical properties.

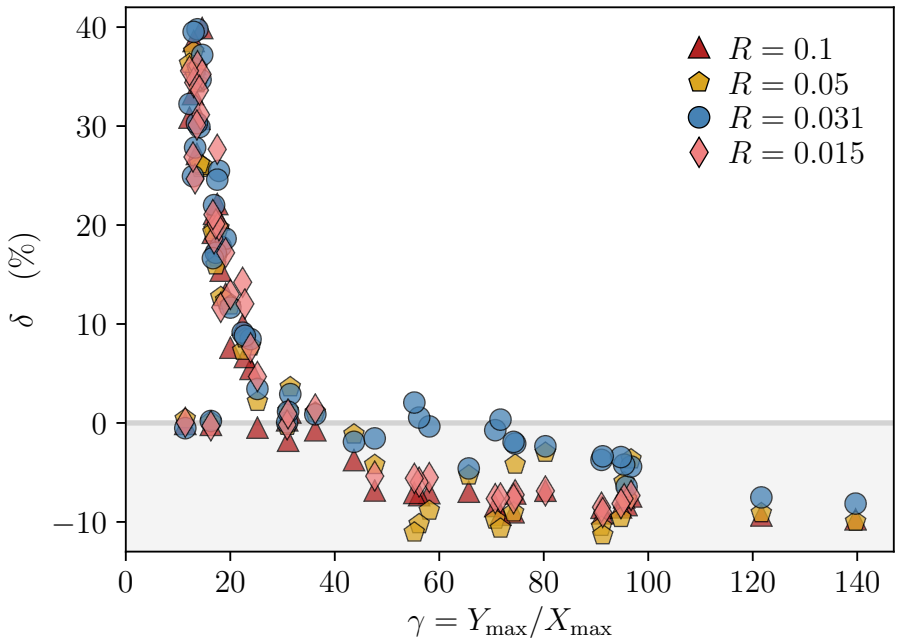

Figure 6.7 Gain in capture versus slenderness of the lemniscate trajectory. Numerical data points collapse well for low slenderness ($\gamma < 0.4$), which is the case at lock-in (see appendix D, Figure D.3).

6.3.2 Distortion

In Figure 6.6 we drew lemniscate limit-cycle trajectories that cylinder describe for various reduced velocities. For low and high U_r, the lemniscate is vertically symmetric, similar to an 'eight'. At lock-in, however, it *distorts* and becomes like a 'boomerang', whose centre shifts towards the left. In this section we study the impact of the lemniscate distortion on the particle capture.

For reduced velocities outside lock-in, for example $U_\mathrm{r} = 8$ in Figure 6.6, the lemniscate is eight-like and has upper and lower branches that are curved. Travelling against the flow, say in the upper loop, the cylinder moves upwards then downwards, and spends little time with a pure stream-wise velocity (at the tip of the loop). A boomerang-like lemniscate, on the other hand, conserves an important stream-wise component of the velocity during the entire upper or lower cycles, hence gets a higher capture rate. Nevertheless, to see the variation of the gain in capture, how can we quantify the degree of distortion of a lemniscate?

Let us write the equation of a lemniscate in a plane. While the cylinder goes up and down once, it moves back and forth twice. Thus, a parametric equation for this trajectory is

$$x(t) = X_\mathrm{max} \cos(4\pi f_\mathrm{n} t), \tag{6.2a}$$

$$y(t) = Y_\mathrm{max}\ \sin(2\pi f_\mathrm{n} t + \beta\pi/2). \tag{6.2b}$$

The coefficient β in the phase of $y(t)$ is what we call the *distortion* coefficient. It takes values between 0 and 1. Figure 6.8 illustrates the shape of lemniscate sharing either the same slenderness or distortion. For instance, a lemniscate with a unique slenderness ratio of $\gamma = 2$ can be either eight-like if it has a distortion coefficient of $\beta = 1/2$, and boomerang-like if $\beta \approx 1$. Also it is worth to mention that $\beta \approx 0$ is also a boomerang-like lemniscate, though distorted in the opposite direction.

To calculate the distortion coefficient, we consider the instants t^+ and t^- when the cylinder is in the downstream-most and upstream-most positions of the lemniscate

$$x(t^+) = +X_\mathrm{max} = X_\mathrm{max} \cos(4\pi f_\mathrm{n} t^+), \tag{6.3a}$$

$$x(t^-) = -X_\mathrm{max} = X_\mathrm{max} \cos(4\pi f_\mathrm{n} t^-). \tag{6.3b}$$

Then we obtain

$$t^+ = 0, \quad t^- = 1/4. \tag{6.4}$$

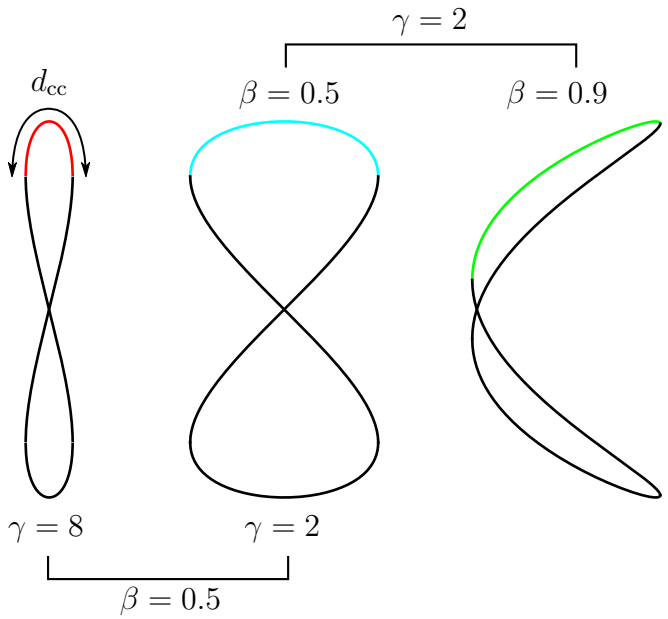

Figure 6.8 The left and middle lemniscates share the same slenderness γ but have different distortion parameters β, and vice versa for the middle and right ones. The upper branch of the lemniscate where the cylinder travels against the stream is highlighted. Its length is the counter-current distance d_{cc}.

Using the normal positions at these instants

$$y(t^+) = Y_{\max} \sin(\beta\pi/2), \tag{6.5a}$$

$$y(t^-) = Y_{\max} \cos(\beta\pi/2), \tag{6.5b}$$

we calculate β through

$$\beta = \frac{2}{\pi} \arctan\left(\frac{y(t^+)}{y(t^-)}\right). \tag{6.6}$$

Figure 6.9 shows the variation of the gain in capture versus the distortion coefficient. We found that δ increases with the distortion of the lemniscate starting from $\beta \approx 0.6$, and reaches the maximum for $\beta \approx 0.75$. Beyond, the lemniscate is too distorted and the cylinder captures less particles. Symmetric lemniscates ($\beta \leq \beta^* \approx 0.62$), on the other hand, are detrimental for capture.

6.4 Counter-current distance

Finally, we elaborate on the above analysis and introduce a new quantity called the *counter-current distance*, denoted d_{cc}. It is the distance that the cylinder travels against the current,

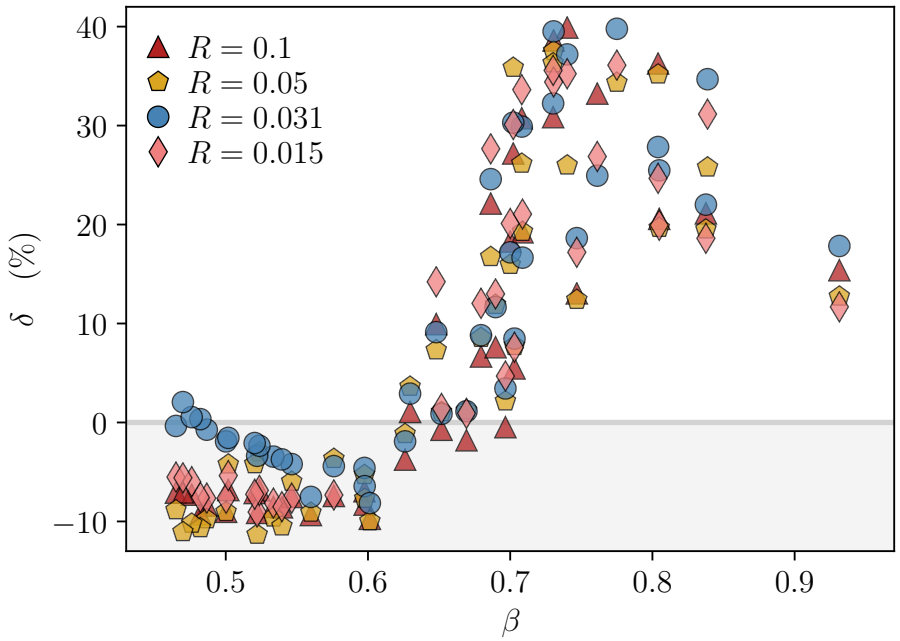

Figure 6.9 Gain in capture rate versus distortion coefficient of the lemniscate

either through the exterior or the interior branches of the lemniscate (highlighted in Figure 6.8 assuming a counter-clockwise motion in the upper loop).

We calculate d_{cc} from the equation of the lemniscate (6.2). We first remove the temporal variable. We have

$$\begin{aligned} x(t)/X_{\max} &= \cos(4\pi f_{\mathrm{n}} t) \\ &= 2\cos^2(2\pi f_{\mathrm{n}} t) - 1 = 1 - 2\sin^2(2\pi f_{\mathrm{n}} t), \end{aligned} \tag{6.7}$$

hence

$$\sin(2\pi f_{\mathrm{n}} t) = \pm\sqrt{(1 - x(t)/X_{\max})/2}, \tag{6.8a}$$

$$\cos(2\pi f_{\mathrm{n}} t) = \pm\sqrt{(1 + x(t)/X_{\max})/2}. \tag{6.8b}$$

We insert (6.8) into

$$\begin{aligned} y(t) &= Y_{\max}\sin(2\pi f_{\mathrm{n}} t + \beta\pi/2) \\ &= Y_{\max}\left[\sin(2\pi f_{\mathrm{n}} t)\cos(\beta\pi/2) + \cos(2\pi f_{\mathrm{n}} t)\sin(\beta\pi/2)\right], \end{aligned} \tag{6.9}$$

and obtain the equations of the four branches forming the lemniscate

$$y_{\pm,\pm} = Y_{\max}\left[\pm\sqrt{\frac{1-x/X_{\max}}{2}}\cos(\beta\pi/2) \pm \sqrt{\frac{1+x/X_{\max}}{2}}\sin(\beta\pi/2)\right]. \tag{6.10}$$

The counter-current distance has the following expression

$$d_{\mathrm{cc}} = \int_{-X_{\max}}^{X_{\max}} \mathrm{d}s(x) \tag{6.11}$$

$$= \int_{-X_{\max}}^{X_{\max}} \sqrt{1+y'^2_{\pm,\pm}(x)}\mathrm{d}x. \tag{6.12}$$

Owing to the horizontal symmetry, the exterior branches $y_{+,+}$ and $y_{-,-}$ and the interior ones $y_{+,-}$ and $y_{-,+}$ have the same distance, respectively $d^{\mathrm{e}}_{\mathrm{cc}}$ and $d^{\mathrm{i}}_{\mathrm{cc}}$, which read

$$d^{\mathrm{e}}_{\mathrm{cc}} = \int_{-X_{\max}}^{X_{\max}} \sqrt{1+y'^2_{+,+}(x)}\mathrm{d}x = X_{\max}\int_{-1}^{1}\sqrt{1+\frac{\gamma^2}{8}\left[\frac{\sin(\beta\pi/2)}{\sqrt{1+\zeta}} - \frac{\cos(\beta\pi/2)}{\sqrt{1-\zeta}}\right]^2}\mathrm{d}\zeta \tag{6.13a}$$

$$d^{\mathrm{i}}_{\mathrm{cc}} = \int_{-X_{\max}}^{X_{\max}} \sqrt{1+y'^2_{+,-}(x)}\mathrm{d}x = X_{\max}\int_{-1}^{1}\sqrt{1+\frac{\gamma^2}{8}\left[\frac{\sin(\beta\pi/2)}{\sqrt{1+\zeta}} + \frac{\cos(\beta\pi/2)}{\sqrt{1-\zeta}}\right]^2}\mathrm{d}\zeta \tag{6.13b}$$

Here we notice the importance of this new parameter: it summarises all the information of the cylinder trajectory through the stream-wise span $X_{\max}$, the slenderness of the lemniscate γ, and its distortion β. In Figure 6.10 we see that the gain in capture increases with the counter-current distance. In support of the interpretation suggested in the above sections, this result means that the larger the distance the cylinder travels against the stream, the higher the number of particles it intercepts. Finally, as it is the case for the previous parameters, there is a critical counter-current distance $\bar{d}^*_{\mathrm{cc}} \approx 0.062$ that the cylinder needs to surpass in order for the vibrations to be beneficial.

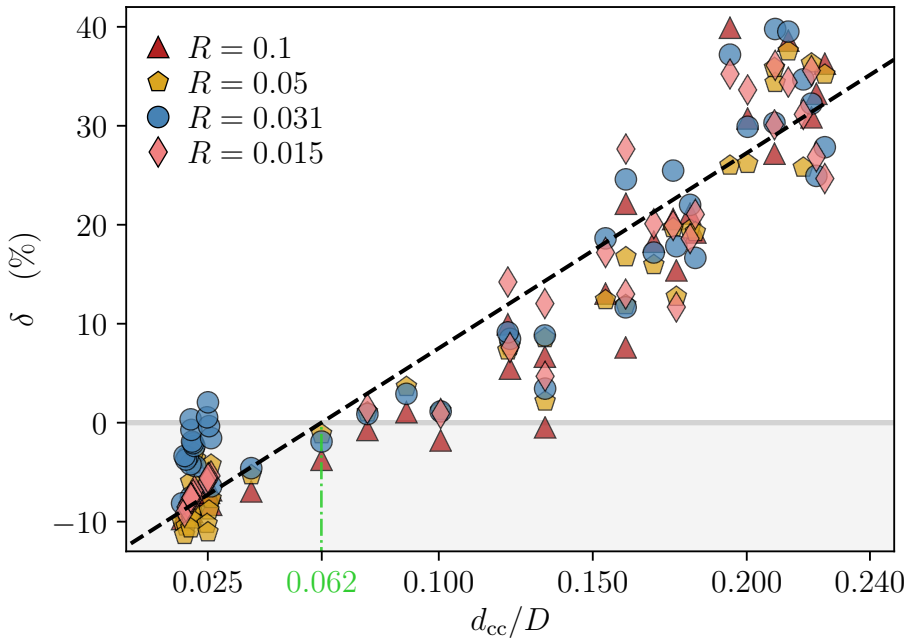

Figure 6.10 Gain in capture rate versus counter-current distance travelled by the cylinder. The dashed line is a linear regression ($r^2 = 0.87$): $\delta = (\bar{d}_{cc} - \bar{d}^*_{cc})/\bar{d}_{cc,0}$, with $\bar{d}^*_{cc} = (6.18 \pm 0.27) \times 10^{-2}$ and $\bar{d}_{cc,0} = (5.07 \pm 0.15) \times 10^{-3}$.

CHAPTER 7 ELASTIC ROD SIMULATIONS

We have simulated, so far, two dimensional flows around a spring-mounted rigid circular cylinder, and calculated the capture rate of advected particles. Although this simplified model depicts the essential mechanisms of particle interception, it has only a single frequency and hides the richer dynamics of an entire slender soft coral branch.

In this chapter, we explore a more realistic image of the soft coral branch by considering the motion of an elastic rod with a clamped end in three-dimensional space. Our goal is to give visual aspects close to the real observations of a vibrating soft coral in ocean. We will not run costly, time-consuming three-dimensional direct numerical flow simulations of a slender cylinder; our strategy, instead, is to tap reduced-order models that reliably transpose the dynamics of vortex-induced vibrations. We base our simulations chiefly on the works of Facchinetti *et al.* [8, 89], which coupled the wake dynamics and rod response. Moreover, we give our simulations a biomechanical feature by including the reconfigured shape of the rod under drag, similar to the dynamics solved by Leclercq and de Langre [14, 85]. Here, we use the FEniCS code, a PYTHON based finite element solver [133].

We start by deriving the Kirchhoff equations for a slender rod, and listing the main forces applying on it. After verifying and validating our code, we present the motion of a rod under fluid-dynamic drag and vortex-induced lift combined.

7.1 Kirchhoff equations

We consider an elastic, straight rod with a clamped end, of a mass per unit length m_l, length L, and cross-section of characteristic length D. The scheme in Figure 7.1 illustrates a circular rod, yet our equations are general for any cross-section. This rod has a flexural rigidity EI and torsional rigidity GJ. For example, a circular cross-section has $I/J = 2$ and $G = E/2(1+\nu)$, where ν is the Poisson ratio. We refer to a position in the rod by the arc length $s \in [0, L]$, and will denote the position vector as $\boldsymbol{w}$.

We build the material frame, along the rod, from the tangential vector $\boldsymbol{t}$ defined as [134]

$$\boldsymbol{t} = \frac{\partial \boldsymbol{w}}{\partial s}. \tag{7.1}$$

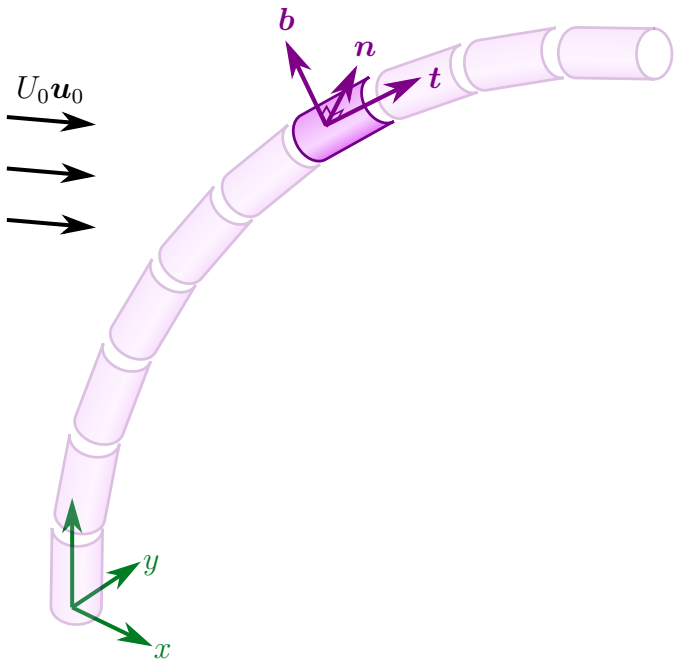

Figure 7.1 Illustration of a rod having a clamped end, within a fluid flow of upstream speed U_0 in the direction $\boldsymbol{u}_0$. The rod is meshed into elements of same length, each of them having a local material frame $(\boldsymbol{t}, \boldsymbol{n}, \boldsymbol{b})$.

The rate of change of the tangential vector along the deformed profile of the rod is [135]

$$\frac{\partial \boldsymbol{t}}{\partial s} = \boldsymbol{\Omega} \times \boldsymbol{t}. \tag{7.2}$$

The vector $\boldsymbol{\Omega}$ is called the Darboux vector, and quantifies the rate of rotation along the rod, or in other words, the curvature of the rod.

The second vector of the material frame is the normal vector, denoted $\boldsymbol{n}$, which also varies as

$$\frac{\partial \boldsymbol{n}}{\partial s} = \boldsymbol{\Omega} \times \boldsymbol{n}. \tag{7.3}$$

Thereby, the vectors $\boldsymbol{t}$ and $\boldsymbol{n}$ remain always orthogonal since

$$\frac{\partial (\boldsymbol{t} \cdot \boldsymbol{n})}{\partial s} = (\boldsymbol{\Omega} \times \boldsymbol{t}) \cdot \boldsymbol{t} + (\boldsymbol{\Omega} \times \boldsymbol{n}) \cdot \boldsymbol{n} = 0. \tag{7.4}$$

We complete the construction of the material frame with the binormal vector $\boldsymbol{b}$ defined as

$$\boldsymbol{b} = \boldsymbol{t} \times \boldsymbol{n}. \tag{7.5}$$

Now we connect kinematic variables with the kinetics through the following constitutive equation [134, 135]

$$\boldsymbol{M} = EI\boldsymbol{\Omega} + (GJ - EI)(\boldsymbol{\Omega} \cdot \boldsymbol{t})\boldsymbol{t}, \tag{7.6}$$

with $\boldsymbol{M}$ the internal moment. This is a general formulation that includes twist, as the product $\boldsymbol{\Omega} \cdot \boldsymbol{t}$ might be non-zero for a given load. In particular, circular cross-sections experience no twist for pure bending ($\boldsymbol{\Omega} \cdot \boldsymbol{t} = 0$) [134].

The internal moment varies proportionally to the internal force $\boldsymbol{F}_{\text{int}}$ (i.e. resultant of internal stresses) via

$$\frac{\partial \boldsymbol{M}}{\partial s} = \boldsymbol{F}_{\text{int}} \times \boldsymbol{t}. \tag{7.7}$$

The variation of the internal force, finally, balances the external force per unit length $\boldsymbol{f}_{\text{ext}}$ acting on the rod

$$\frac{\partial \boldsymbol{F}_{\text{int}}}{\partial s} = m_{\text{l}} \frac{\partial^2 \boldsymbol{w}}{\partial t^2} - \boldsymbol{f}_{\text{ext}}, \tag{7.8}$$

assuming that external moments are absent.

We propose to work with the following dimensionless variables

$$\tilde{t} = \frac{t}{t_{\text{s}}}, \quad \tilde{s} = \frac{s}{L}, \quad \tilde{\boldsymbol{w}} = \frac{1}{L}\boldsymbol{w}, \quad \tilde{\boldsymbol{\Omega}} = L\boldsymbol{\Omega}, \quad \tilde{\boldsymbol{M}} = \frac{L}{EI}\boldsymbol{M}, \quad \tilde{\boldsymbol{F}}_{\text{int}} = \frac{L^2}{EI}\boldsymbol{F}_{\text{int}}, \quad \tilde{\boldsymbol{f}}_{\text{ext}} = \frac{L^3}{EI}\boldsymbol{f}_{\text{ext}}, \tag{7.9}$$

with

$$t_{\text{s}} = L^2\sqrt{\frac{m_{\text{l}}}{EI}} \tag{7.10}$$

being a characteristic time for the structural deformation. The governing equations hence read

$$\begin{aligned} &\frac{\partial \tilde{\boldsymbol{w}}}{\partial \tilde{s}} = \boldsymbol{t}, \quad \frac{\partial \boldsymbol{t}}{\partial \tilde{s}} = \tilde{\boldsymbol{\Omega}} \times \boldsymbol{t}, \quad \frac{\partial \boldsymbol{n}}{\partial \tilde{s}} = \tilde{\boldsymbol{\Omega}} \times \boldsymbol{n}, \\ &\frac{\partial \tilde{\boldsymbol{M}}}{\partial \tilde{s}} = \tilde{\boldsymbol{F}}_{\text{int}} \times \boldsymbol{t}, \quad \frac{\partial \tilde{\boldsymbol{F}}_{\text{int}}}{\partial \tilde{s}} = \frac{\partial^2 \tilde{\boldsymbol{w}}}{\partial \tilde{t}^2} - \tilde{\boldsymbol{f}}_{\text{ext}}, \end{aligned} \tag{7.11}$$

with

$$\tilde{\boldsymbol{M}} = \tilde{\boldsymbol{\Omega}} + \left(\frac{GJ}{EI} - 1\right)(\tilde{\boldsymbol{\Omega}} \cdot \boldsymbol{t})\boldsymbol{t}. \tag{7.12}$$

For a rod having a clamped end, the boundary conditions are

$$\boldsymbol{w}|_{s=0} = \boldsymbol{w}_{\text{root}}, \quad \boldsymbol{t}|_{s=0} = \left.\frac{\partial \boldsymbol{w}}{\partial s}\right|_{s=0} = \boldsymbol{t}_{\text{root}}, \quad \boldsymbol{n}|_{s=0} = (\boldsymbol{t}_{\text{root}} \times \boldsymbol{u}) / \left|\left|\boldsymbol{t}_{\text{root}} \times \boldsymbol{u}\right|\right|,$$
$$\boldsymbol{M}|_{s=L} = \boldsymbol{0}, \quad \boldsymbol{F}_{\text{int}}|_{s=L} = \boldsymbol{0}, \tag{7.13}$$

where we take $\boldsymbol{u}$ as a reference direction, which we choose to be the flow direction when considering fluid-dynamic simulation problems in particular (section 7.2). In the following we assume that the initial rod configuration is rooted at $\boldsymbol{w}_{\text{root}} = \boldsymbol{0}$, and points towards the direction $\boldsymbol{t}_{\text{root}}$. In dimensionless form, we have

$$\tilde{\boldsymbol{w}}|_{\tilde{s}=0} = \boldsymbol{0}, \quad \boldsymbol{t}|_{\tilde{s}=0} = \boldsymbol{t}_{\text{root}}, \quad \boldsymbol{n}|_{\tilde{s}=0} = (\boldsymbol{t}_{\text{root}} \times \boldsymbol{u}) / \left|\left|\boldsymbol{t}_{\text{root}} \times \boldsymbol{u}\right|\right|,$$
$$\tilde{\boldsymbol{\Omega}}|_{\tilde{s}=1} = \boldsymbol{0}, \quad \tilde{\boldsymbol{F}}_{\text{int}}|_{\tilde{s}=1} = \boldsymbol{0}. \tag{7.14}$$

7.2 External forces

The external force $\tilde{\boldsymbol{f}}_{\text{ext}}$ in (7.11) is general. Throughout this study, we will consider four forces. The first force is the uniformly distributed load. It will serve as a benchmark for the verification of our code. Then, the second force is the fluid-dynamic drag, which gives the rod a reconfigured shape like in slender species in nature. The third force is the added mass force, which affects the rod dynamics especially during important accelerations. Finally, the fourth force is the vortex-induced force that brings about VIV along the rod.

7.2.1 Distributed load

The distributed load $\boldsymbol{f}_{\text{dist}}$ points towards a certain unit vector $\boldsymbol{u}$, and has a magnitude (per unit length) of f_0

$$\boldsymbol{f}_{\text{dist}} = f_0 \boldsymbol{u}. \tag{7.15}$$

Therefore, the dimensionless distributed load is

$$\tilde{\boldsymbol{f}}_{\text{dist}} = \tilde{f}_0 \boldsymbol{u}, \tag{7.16}$$

with

$$\tilde{f}_0 = \frac{f_0 L^3}{EI}. \tag{7.17}$$

7.2.2 Drag

Suppose that the rod is within a fluid flow of upstream velocity $\boldsymbol{U}_0 = U_0\boldsymbol{u}_0$. Following the empirical work of Taylor [136], the axial component of the drag is neglected, and only the components of the fluid velocity that are perpendicular to the rod, namely

$$u_{0,n} = \boldsymbol{u}_0 \cdot \boldsymbol{n} \quad \text{and} \quad u_{0,b} = \boldsymbol{u}_0 \cdot \boldsymbol{b}, \tag{7.18}$$

generate load. The force that acts on an infinitesimal length $\mathrm{d}s$ expresses as

$$\mathrm{d}\boldsymbol{F}_\mathrm{D} = \frac{1}{2} C_\mathrm{D} D \rho_\mathrm{f} \left(|\boldsymbol{U}_0 \cdot \boldsymbol{n}| \, (\boldsymbol{U}_0 \cdot \boldsymbol{n}) \boldsymbol{n} + |\boldsymbol{U}_0 \cdot \boldsymbol{b}| \, (\boldsymbol{U}_0 \cdot \boldsymbol{b}) \boldsymbol{b} \right) \mathrm{d}s \tag{7.19}$$

$$= \frac{1}{2} C_\mathrm{D} D \rho_\mathrm{f} U_0^2 \left(|u_{0,n}| \, u_{0,n} \boldsymbol{n} + |u_{0,b}| \, u_{0,b} \boldsymbol{b} \right) \mathrm{d}s, \tag{7.20}$$

where C_D is the drag coefficient of the rod cross-section. We deduce the drag per unit length

$$\boldsymbol{f}_\mathrm{D} = \frac{\partial \boldsymbol{F}_\mathrm{D}}{\partial s} = \frac{1}{2} C_\mathrm{D} D \rho_\mathrm{f} U_0^2 (|u_{0,n}| \, u_{0,n} \boldsymbol{n} + |u_{0,b}| \, u_{0,b} \boldsymbol{b}), \tag{7.21}$$

which reads in dimensionless form

$$\tilde{\boldsymbol{f}}_\mathrm{D} = C_\mathrm{D} C_\mathrm{Y} (|u_{0,n}| \, u_{0,n} \boldsymbol{n} + |u_{0,b}| \, u_{0,b} \boldsymbol{b}). \tag{7.22}$$

The ratio

$$C_\mathrm{Y} = \frac{\rho_\mathrm{f} U_0^2 D L^3}{2EI} \tag{7.23}$$

is the Cauchy number, and compares the fluid-dynamic pressure to the elastic bending rigidity of the rod [137].

We point out that, in transient simulations, we shall replace $\boldsymbol{U}_0$ by the fluid velocity relative to the rod speed

$$\boldsymbol{U}_\mathrm{rel} = U_0 \boldsymbol{u}_0 - \frac{\partial \boldsymbol{w}}{\partial t}, \tag{7.24}$$

hence replace $\boldsymbol{u}_0$ in (7.18) by

$$\boldsymbol{u}_\mathrm{rel} = \boldsymbol{u}_0 - \lambda \frac{\partial \tilde{\boldsymbol{w}}}{\partial \tilde{t}}. \tag{7.25}$$

The constant λ is

$$\lambda = \frac{L}{U_0 t_\mathrm{s}} = \frac{St \Gamma}{U_\mathrm{r}}, \tag{7.26}$$

with St the Strouhal number, $U_\mathrm{r} = St U_0 t_\mathrm{s}/D$ the reduced velocity, and $\Gamma = L/D$ the aspect ratio of the rod. Here λ gives an idea of the magnitude of the rod velocity with respect to the fluid speed: a small λ indicates a slow rod motion, whereas a large λ indicates a fast rod

motion.

We will refer to the relative direction by removing the subscript $(.)_0$ from the variables

$$u_n = \boldsymbol{u}_{\text{rel}} \cdot \boldsymbol{n} \quad \text{and} \quad u_b = \boldsymbol{u}_{\text{rel}} \cdot \boldsymbol{b}, \tag{7.27}$$

so that we have in the dynamic case

$$\tilde{\boldsymbol{f}}_{\text{D}} = C_{\text{D}} C_{\text{Y}} (|u_n|\, u_n \boldsymbol{n} + |u_b|\, u_b \boldsymbol{b}). \tag{7.28}$$

7.2.3 Added mass

Following the work of Leclercq and de Langre [14,85], we use the added mass force expression for slender structures proposed by Candelier *et al.* [138] (notice the sign of the force and the relative velocity definition (7.24))

$$\boldsymbol{f}_{\text{A}} = m_{\text{a}} \left[U_0 \frac{\partial (u_n \boldsymbol{n} + u_b \boldsymbol{b})}{\partial t} + U_0^2 \frac{\partial u_t (u_n \boldsymbol{n} + u_b \boldsymbol{b})}{\partial s} - \frac{U_0^2}{2} \frac{\partial (u_n^2 + u_b^2) \boldsymbol{t}}{\partial s} \right], \tag{7.29}$$

with m_{a} being the added mass per unit length. We define

$$m_{\text{a}} = c_{\text{a}} \pi \rho_{\text{f}} D^2 / 4, \tag{7.30}$$

where c_{a} is a coefficient depending on the shape of the cross-section ($c_{\text{a}} = 1$ for a circular cross-section). The dimensionless form of the added mass force take the following form

$$\tilde{\boldsymbol{f}}_{\text{A}} = \frac{\pi c_{\text{a}} C_{\text{Y}}}{2\Gamma} \left[\lambda \frac{\partial (u_n \boldsymbol{n} + u_b \boldsymbol{b})}{\partial \tilde{t}} + \frac{\partial u_t (u_n \boldsymbol{n} + u_b \boldsymbol{b})}{\partial \tilde{s}} - \frac{1}{2} \frac{\partial (u_n^2 + u_b^2) \boldsymbol{t}}{\partial \tilde{s}} \right]. \tag{7.31}$$

7.2.4 Vortex-induced lift

In the phenomenological wake-oscillator model of Facchinetti *et al.* [89], the lift induced by vortices is perpendicular to the flow stream and rod axis. In our three-dimensional simulations, we fix the direction of the lift $\boldsymbol{u}_0^{\perp}$ as the normal to the plane defined by the flow and initial rod configuration

$$\boldsymbol{u}_0^{\perp} = (\boldsymbol{t}_{\text{root}} \times \boldsymbol{u}_0) / \left| |\boldsymbol{t}_{\text{root}} \times \boldsymbol{u}_0| \right|, \tag{7.32}$$

which is also equal to $\boldsymbol{n}_0$ at the clamped end ($\boldsymbol{u}_0^{\perp} = \boldsymbol{n}_{\text{root}}$). Though, we discarded the choice of the instantaneous $\boldsymbol{n} = \boldsymbol{n}(\tilde{t}, \tilde{s})$ because it varies in time and in space, whereas the lift direction in Facchinetti *et al.* [89] remains constant along the rod.

The lift force can be expressed as

$$\boldsymbol{f}_{\mathrm{VIV}} = \frac{1}{2} C_{\mathrm{L}} D \rho_{\mathrm{f}} U_0^2 u_b^2 \boldsymbol{u}_0^{\perp}, \tag{7.33}$$

where the time-fluctuating lift coefficient is written as [89]

$$C_{\mathrm{L}} = \frac{C_{\mathrm{L}}^0}{2} q. \tag{7.34}$$

The measured lift coefficient of a fixed rod cross-section during vortex shedding is defined as C_{L}^0, and q is the fluctuating variable which is solution of the van der Pol equation

$$\frac{\partial^2 q}{\partial t^2} + \varepsilon \left[\frac{2\pi St U_0 |u_b|}{D} \right] (q^2 - 1) \frac{\partial q}{\partial t} + \left[\frac{2\pi St U_0 |u_b|}{D} \right]^2 q = \frac{A}{D} \frac{\partial^2 \boldsymbol{w}}{\partial t^2} \cdot \boldsymbol{u}_0^{\perp}, \tag{7.35}$$

with $U_0 u_b$ being the binormal component of the upstream flow velocity, perpendicular to the rod. In the ensuing simulations we will take the same coupling constants $A = 12$ and $\varepsilon = 0.3$ as in Facchinetti *et al.* [89], which give correct results even for slender flexible structures.

We non-dimensionalise the expression of the vortex-induced lift

$$\tilde{\boldsymbol{f}}_{\mathrm{VIV}} = \frac{C_{\mathrm{L}}^0 C_{\mathrm{Y}}}{2} u_b^2 q \boldsymbol{u}_0^{\perp}, \tag{7.36}$$

and the van der Pol equation

$$\frac{\partial^2 q}{\partial \tilde{t}^2} + \varepsilon \omega_{\mathrm{f}} |u_b| (q^2 - 1) \frac{\partial q}{\partial \tilde{t}} + \omega_{\mathrm{f}}^2 u_b^2 q = \Gamma A \frac{\partial^2 \tilde{\boldsymbol{w}}}{\partial \tilde{t}^2} \cdot \boldsymbol{u}_0^{\perp}, \tag{7.37}$$

with

$$\omega_{\mathrm{f}} = 2\pi St \frac{U_0 t_{\mathrm{s}}}{D} = 2\pi U_{\mathrm{r}}. \tag{7.38}$$

In the rest of this chapter, we will drop the notation $\tilde{(.)}$ out of dimensionless quantities. Also, we will denote the temporal derivative as $\dot{(.)}$ and the spatial derivative as $(.)'$.

7.3 Variational formulation and solution strategy

7.3.1 Variational formulation

In order to solve the above system of equations in FEniCS, we need to write the variational formulation of the governing system. We consider for each unknown $\boldsymbol{w}, \boldsymbol{t}, \boldsymbol{n}, \boldsymbol{\Omega}$, and $\boldsymbol{F}_{\mathrm{int}}$, its corresponding test function $\hat{(.)}$ that vanishes at both ends of the rod.

For the static case, the variational problem reads

$$F = \int_0^1 \mathscr{L} \mathrm{d}s = 0 \tag{7.39}$$

with

$$\begin{aligned}\mathscr{L} = &(\boldsymbol{w}' - \boldsymbol{t}) \cdot \hat{\boldsymbol{w}} + (\boldsymbol{t}' - \boldsymbol{\Omega} \times \boldsymbol{t}) \cdot \hat{\boldsymbol{t}} + (\boldsymbol{n}' - \boldsymbol{\Omega} \times \boldsymbol{n}) \cdot \hat{\boldsymbol{n}} \\ &+ (\boldsymbol{\Omega}' - \boldsymbol{F}_{\mathrm{int}} \times \boldsymbol{t}) \cdot \hat{\boldsymbol{\Omega}} + (\boldsymbol{F}'_{\mathrm{int}} + \boldsymbol{f}_{\mathrm{ext}}) \cdot \hat{\boldsymbol{F}}_{\mathrm{int}}.\end{aligned} \tag{7.40}$$

For the transient case, we introduce $\boldsymbol{v} = \dot{\boldsymbol{w}}$ and keep only first-order temporal derivatives in (7.11)

$$\dot{\boldsymbol{w}} = \boldsymbol{v}, \tag{7.41}$$

$$\dot{\boldsymbol{v}} = \boldsymbol{F}'_{\mathrm{int}} + \boldsymbol{f}_{\mathrm{ext}}. \tag{7.42}$$

We consider a temporal subdivision with a constant time step Δt, and choose a backward Euler scheme

$$\dot{\boldsymbol{w}}_{k+1} = \frac{\boldsymbol{w}_{k+1} - \boldsymbol{w}_k}{\Delta t} = \boldsymbol{v}_{k+1}, \tag{7.43}$$

$$\dot{\boldsymbol{v}}_{k+1} = \frac{\boldsymbol{v}_{k+1} - \boldsymbol{v}_k}{\Delta t} = \boldsymbol{F}'_{\mathrm{int},k+1} + \boldsymbol{f}_{\mathrm{ext},k+1}. \tag{7.44}$$

Finally, assuming that the solution at $t_k = k\Delta t$ is known, the variational formulation is

$$F_{k+1} = \int_0^1 \mathscr{L}_{k+1} \mathrm{d}s = 0 \tag{7.45}$$

with

$$\begin{aligned}\mathscr{L}_{k+1} = &\left(\boldsymbol{w}'_{k+1} - \boldsymbol{t}_{k+1}\right) \cdot \hat{\boldsymbol{w}} + \left(\boldsymbol{t}'_{k+1} - \boldsymbol{\Omega}_{k+1} \times \boldsymbol{t}_{k+1}\right) \cdot \hat{\boldsymbol{t}} + \left(\boldsymbol{n}'_{k+1} - \boldsymbol{\Omega}_{k+1} \times \boldsymbol{n}_{k+1}\right) \cdot \hat{\boldsymbol{n}} \\ &+ \left(\boldsymbol{M}'_{k+1} - \boldsymbol{F}_{\mathrm{int},k+1} \times \boldsymbol{t}_{k+1}\right) \cdot \hat{\boldsymbol{\Omega}} + \left(\frac{\boldsymbol{w}_{k+1} - \boldsymbol{w}_n}{\Delta t} - \boldsymbol{v}_{k+1}\right) \cdot \hat{\boldsymbol{v}} \\ &+ \left(\frac{\boldsymbol{v}_{k+1} - \boldsymbol{v}_n}{\Delta t} - \boldsymbol{F}'_{\mathrm{int},k+1} - \boldsymbol{f}_{\mathrm{ext},k+1}\right) \cdot \hat{\boldsymbol{F}}_{\mathrm{int}}.\end{aligned} \tag{7.46}$$

Likewise, if we include the vortex-induced lift accompanied with the van der Pol equation,

we introduce $p = \dot{q}$ and apply the same scheme as in (7.44)

$$\dot{q}_{k+1} = \frac{q_{k+1} - q_k}{\Delta t} = p_{k+1}, \tag{7.47}$$

$$\begin{aligned}\dot{p}_{k+1} &= \frac{p_{k+1} - p_k}{\Delta t} \\ &= -\varepsilon\omega_\mathrm{f}|u_{b,k+1}|(q_{k+1}^2 - 1)p_{k+1} - \omega_\mathrm{f}^2 u_{b,k+1}^2 q_{k+1} + \frac{\Gamma A}{\Delta t}(\boldsymbol{v}_{k+1} - \boldsymbol{v}_k)\cdot\boldsymbol{u}_0^\perp.\end{aligned} \tag{7.48}$$

The new variational form to solve is thus

$$F_{k+1} = \int_0^1 \left(\mathscr{L}_{k+1} + \mathscr{L}_{k+1}^{\text{van der Pol}}\right) \mathrm{d}s, \tag{7.49}$$

with $\mathscr{L}_{k+1}$ defined in (7.46) and

$$\begin{aligned}\mathscr{L}_{k+1}^{\text{van der Pol}} = &\left(\frac{q_{k+1} - q_k}{\Delta t} - p_{k+1}\right)\hat{q} \\ &+ \left[\frac{p_{k+1} - p_k}{\Delta t} + \varepsilon\omega_\mathrm{f}|u_{b,k+1}|\left(q_{k+1}^2 - 1\right)p_{k+1} + \omega_\mathrm{f}^2 u_{b,k+1}^2 q_{k+1} - \frac{\Gamma A}{\Delta t}(\boldsymbol{v}_{k+1} - \boldsymbol{v}_k)\cdot\boldsymbol{u}_0^\perp\right]\hat{p}.\end{aligned} \tag{7.50}$$

7.3.2 Initial conditions and solving method

Initially, we assign the node positions of the mesh to the vector $\boldsymbol{w}|_{t=0,s} = \boldsymbol{w}_\mathrm{init}(s)$. In FEniCS we extract directly the tangential vector of the initial configuration $\boldsymbol{t}_0$ of each element, then calculate the normal vector from

$$\boldsymbol{n}_\mathrm{init} = (\boldsymbol{t}_\mathrm{init} \times \boldsymbol{u}) / \left|\left|\boldsymbol{t}_\mathrm{init} \times \boldsymbol{u}\right|\right|. \tag{7.51}$$

To calculate the initial value of the Darboux vector $\boldsymbol{\Omega}_\mathrm{init}$ and internal stress $\boldsymbol{F}\mathrm{int,init}$, we cross-multiply the vector $\boldsymbol{t}_\mathrm{init}$ with the equations (7.1), (7.1), and (7.7)

$$\boldsymbol{\Omega}_\mathrm{init} = \boldsymbol{t}_\mathrm{init} \times \frac{\partial \boldsymbol{t}_\mathrm{init}}{\partial s} + (\boldsymbol{b}_\mathrm{init} \cdot \frac{\partial \boldsymbol{n}_\mathrm{init}}{\partial s})\boldsymbol{t}_\mathrm{init}, \tag{7.52}$$

$$\boldsymbol{F}\mathrm{int,init} = \boldsymbol{t}_\mathrm{init} \times \frac{\partial \boldsymbol{M}_\mathrm{init}}{\partial s}. \tag{7.53}$$

When we consider transient simulations, we always take a zero initial velocity $\boldsymbol{v}_\mathrm{init} = \boldsymbol{0}$, and we assign to q, at each node, a random value of order $\sim 10^{-3}$, with $p = 0$.

We mesh the rod into uniform intervals. These are one-dimensional elements embedded in a three-dimensional space. We choose $\mathcal{P}_1$ Lagrange elements, and solve the nonlinear equations

using the Newton method. An example of a static simulation is shown in Figure 7.2, where a circular rod is subjected to drag.

Details about the FEniCS implementation in PYTHON are provided in appendix E.

7.4 Verification

To verify that our code solves the equations correctly, we consider the problem of a rod subject to a uniformly distributed load.

7.4.1 Static case

We calculate the discretisation error ε_N between a fine grid with N elements and a coarse one with $N/2$ elements [139]

$$\varepsilon_N = \left|\left|w_{0,N} - w_{0,N/2}\right|\right|_2 = \left[\frac{1}{N/2}\sum_{i=1}^{N/2} |w_{0,N}(s_i) - w_{0,N/2}(s_i)|^2\right]^{1/2}, \tag{7.54}$$

where the subscript $(.)_{.,N}$ refers to the solution under a mesh of N elements, and

$$w_0(s_i) = \boldsymbol{u}_0 \cdot \boldsymbol{w}|_{s_i}, \quad s_i = \frac{i}{N/2}. \tag{7.55}$$

We also calculate the observed order of accuracy $\hat{p}_N$ [139]

$$\hat{p}_N = \frac{\log(\varepsilon_{N/2}/\varepsilon_N)}{\log(2)}. \tag{7.56}$$

As expected from the use of $\mathcal{P}_1$ elements, the discretisation error is inversely proportional to the square of the element size, and the observed order of accuracy is close to 2 (Figure 7.3).

7.4.2 Dynamic case

We now fix the mesh ($N = 10$) and look at the dynamic response of a rod under a distributed load from $t_0 = 0$ to the same final instant $t_\mathrm{f} = N_\mathrm{f}\Delta t$. We consider here the temporal discretisation error of the tip displacement

$$\varepsilon_{\Delta t} = ||w_{0,2\Delta t} - w_{0,\Delta t}||_2 = \left[2\Delta t \sum_{i=1}^{N_\mathrm{f}/2} |w^{\mathrm{tip}}_{0,2\Delta t}(t_k) - w^{\mathrm{tip}}_{0,\Delta t}(t_k)|^2\right]^{1/2}, \tag{7.57}$$

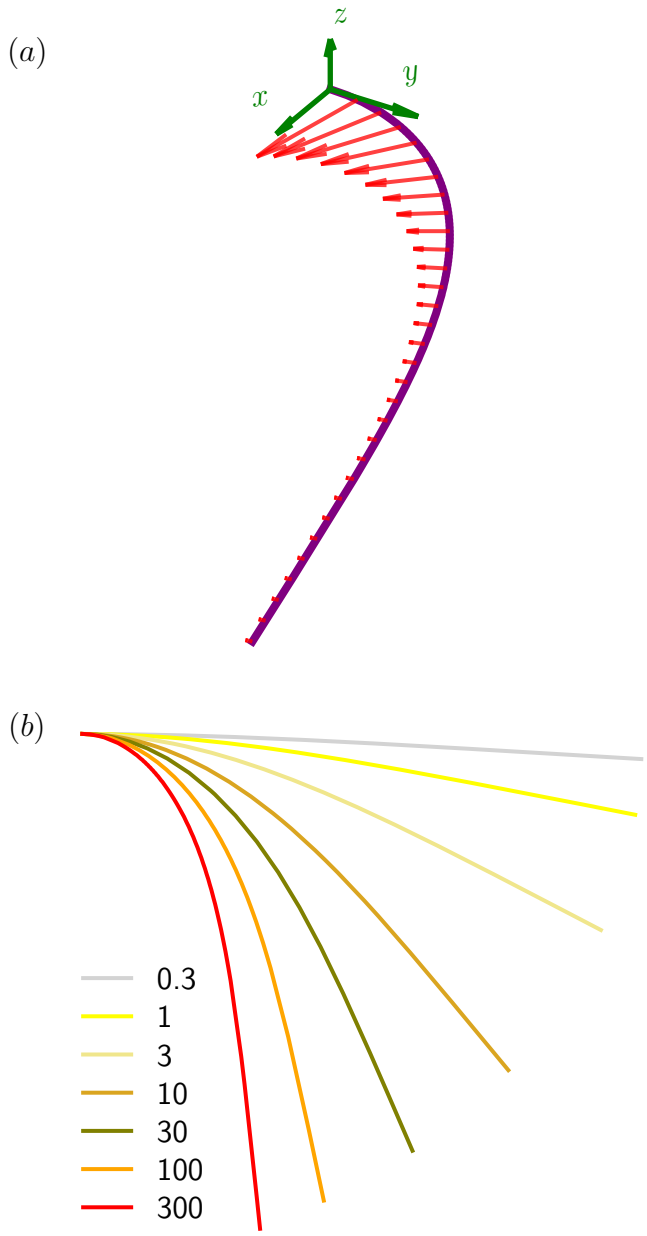

Figure 7.2 Examples of static simulations. (a) Three-dimensional view of an initially straight rod aligned with the y-axis in a flow in the $\boldsymbol{u}_0 = \boldsymbol{e}_x$ direction. This rod has a Cauchy number of $C_{\mathrm{Y}} = 100$. Red arrows represent the drag magnitude. (b) Rod reconfiguration under drag for different Cauchy numbers.

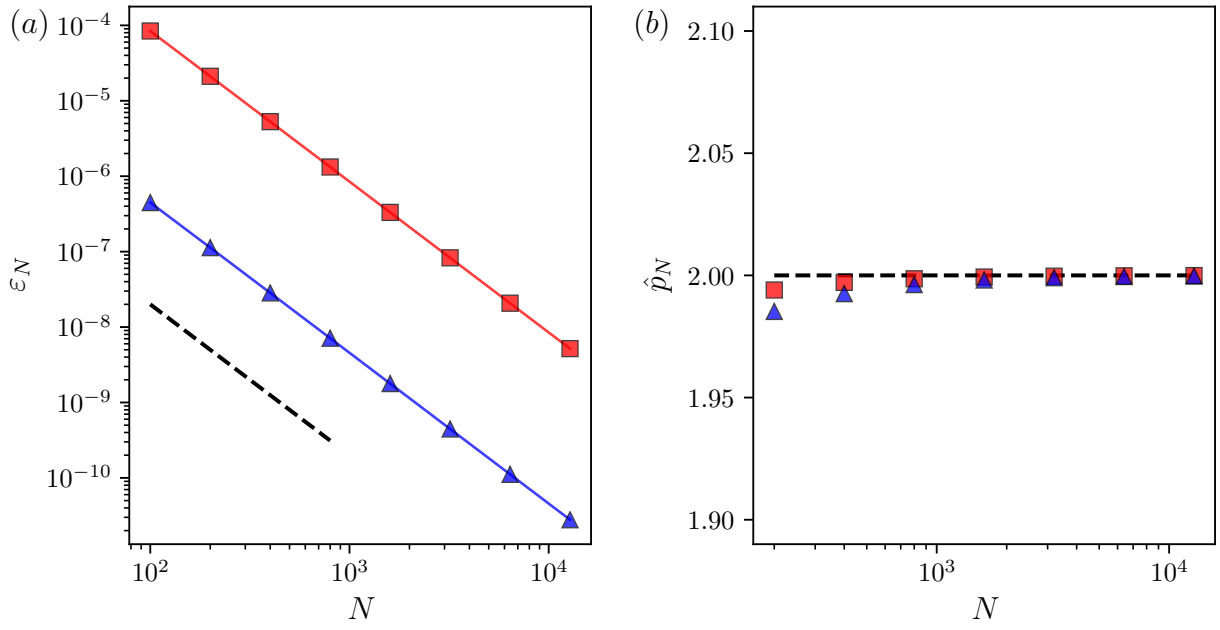

Figure 7.3 Code verification for the rod deflection under distributed load of small magnitude (▲, $\tilde{f}_0 = 0.1$) and a large magnitude (■, $\tilde{f}_0 = 10$). (*a*) Discretisation error using the norm L_2. (*b*) Observed order of accuracy using the Richardson extrapolation. The dashed lines refer to a quadratic variation.

where the subscript $(.)_{.,\Delta t}$ refers to the solution with a time step equal to Δt, and

$$w_0^{\text{tip}}(t_k) = \boldsymbol{u}_0 \cdot \boldsymbol{w}|_{t=t_k, s=1}, \quad t_k = k2\Delta t. \tag{7.58}$$

Likewise, we calculate the observed order of accuracy $\hat{p}_{\Delta t}$

$$\hat{p}_{\Delta} = \frac{\log(\varepsilon_{\Delta}/\varepsilon_{2\Delta t})}{\log(2)}. \tag{7.59}$$

Figure 7.4 shows that the discretisation error varies linearly with the time step and the observed order of accuracy is close to 1, which is consistent with the use of a first order backward Euler scheme.

7.5 Validation

Having verified the numerical solution, we now validate our code to ensure it reliably reflects the physical problem.

7.5.1 Static case

Regarding the static case, we simulate two benchmarks. The first benchmark is the rod under a distributed load. For a range of loads $\tilde{f}_0 \boldsymbol{u}$, Figure 7.5$(a)$ shows the numerical deflection of the rod at the tip

$$\delta_{\text{FEniCS}} = \boldsymbol{w}|_{s=1} \cdot \boldsymbol{u} \tag{7.60}$$

compared with the theoretical formula δ_{th} derived by Rohde [140], which is based on series expansion. Taking the two leading terms in the approximation of δ_{th}, we found that the numerical results match well with the theoretical solution even for considerable loads outside the linear regime $\delta \propto \tilde{f}_0$ ($|\delta_{\text{th}} - \delta_{\text{FEniCS}}| / \delta_{\text{th}} < 1.4\%$).

The second benchmark is a rod under drag. We evaluate the reconfiguration number, denoted $\mathcal{R}$, defined as the total drag F_{D} applied on the elastic rod scaled by the total drag on a rigid one

$$\mathcal{R} = F_{\text{D}} \Big/ \left(\frac{1}{2}\rho_{\text{f}} D L C_{\text{D}} U_0^2\right). \tag{7.61}$$

In our code, we extract $\mathcal{R}$ as follows

$$\mathcal{R} = \int_0^1 \boldsymbol{u}_0 \cdot \boldsymbol{f}_{\text{D}} \mathrm{d}s \Big/ \left(\frac{1}{2}\rho_{\text{f}} D L C_{\text{D}} U_0^2\right). \tag{7.62}$$

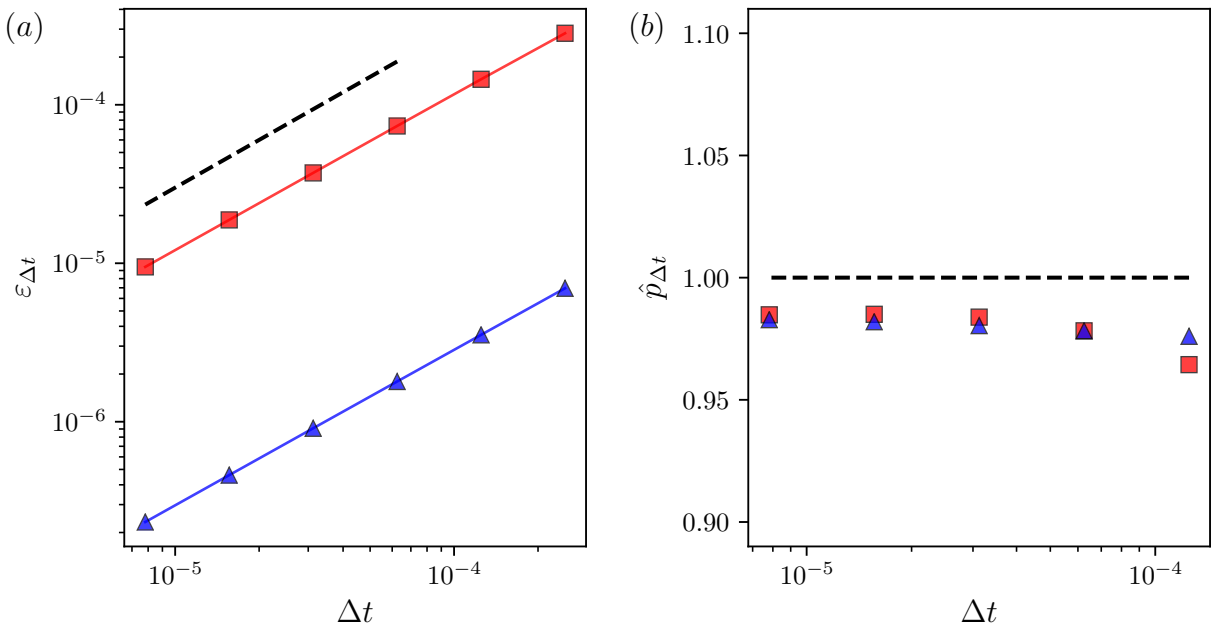

Figure 7.4 Code verification for the distributed load of small magnitude (▲, $\tilde{f}_0 = 0.1$) and a large magnitude (■, $\tilde{f}_0 = 10$). (a) Discretisation error using the norm L_2. (b) Observed order of accuracy using the Richardson extrapolation. The dashed lines refer to a linear variation.

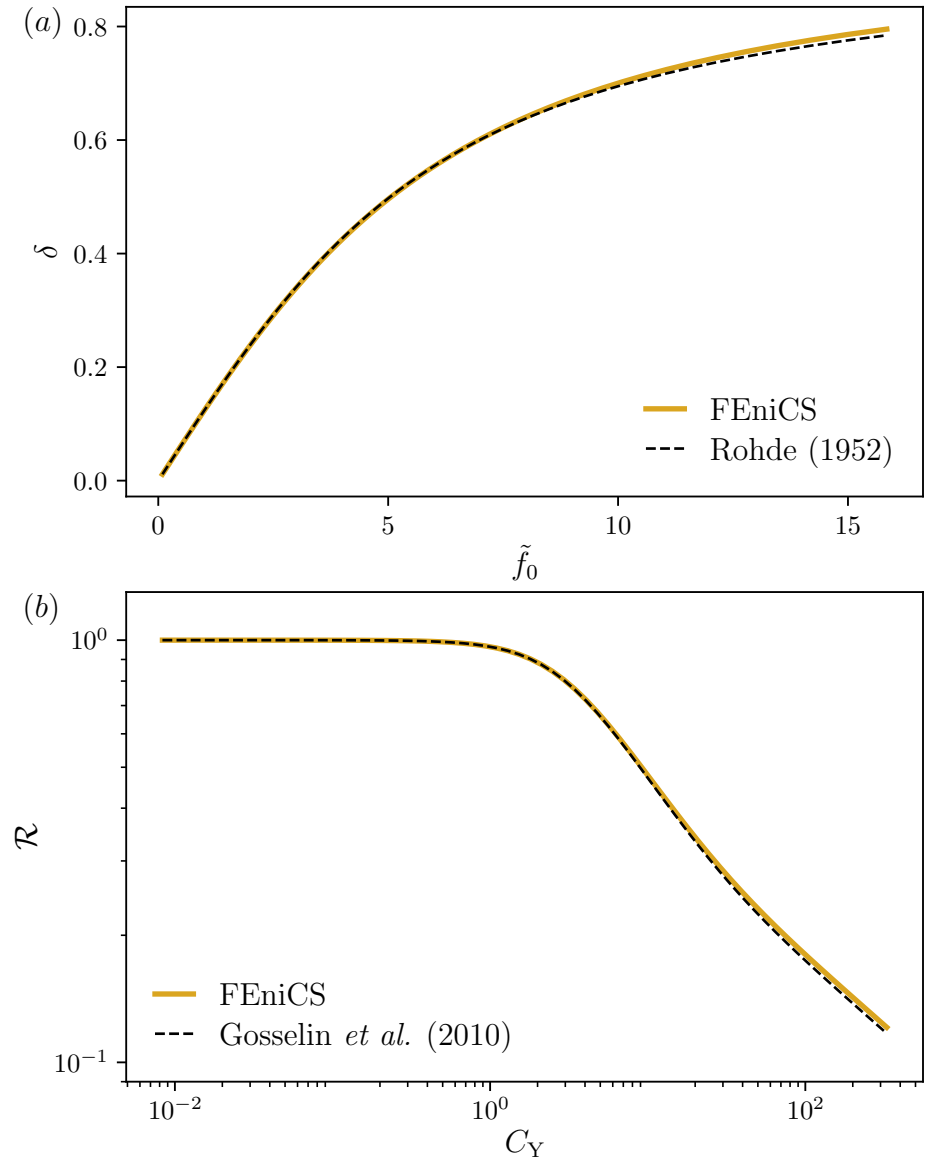

Figure 7.5 Comparison of the FEniCS solution with theoretical (a) maximum deflection of a rod under a distributed load and (b) reconfiguration number of a rod under drag.

Gosselin *et al.* [20] proposed a theoretical model, supported with experiments, that finds the reconfigured shape of a flexible thin, slender plate, and calculates the reconfiguration number for a wide range of Cauchy numbers. Since Kirchhoff equations govern both slender beams and rods, we compare our numerical results with the theoretical $\mathcal{R} - C_{\mathrm{Y}}$ curve of Gosselin *et al.* [20]. The comparison is shown in Figure 7.5(b). Here again, our simulations lay well on the theoretical model ($|\mathcal{R}_{\mathrm{th}} - \mathcal{R}_{\mathrm{FEniCS}}|/\mathcal{R}_{\mathrm{th}} < 3.1\%$).

7.5.2 Dynamic case

Leclercq and de Langre [14] recorded the underwater motion of a thin plate fastened with an actuator that oscillates for different sets of pulsations Ω and displacements A. To transpose these experiments in our code, which fixes the clamped end, we make the rod sway back and forth by applying an oscillating flow

$$U(t) = U_0 \sin(\Omega t), \tag{7.63}$$

and choosing the corresponding velocity as

$$U_0 = \text{actuator displacement} \times \text{actuator pulsation} = A\Omega. \tag{7.64}$$

We consider low, moderate, and high pulsations $\omega = \Omega t_{\mathrm{s}} = 0.38, 1.07, 2.01$, with three different actuator displacements $\alpha = A/L = 0.27, 0.46, 0.65$. We simulate the rod deformation over four periods and save the deformation profiles during the last period. We present experimental and numerical deformation profiles in Figure 7.6. Results match well with the measurements of Leclercq and de Langre [14], especially for low and moderate pulsations. The numerical deformation under high pulsation $\omega = 2.01$ is also comparable. There is a slight inclination in the cases $\alpha = 0.27$, which is absent from the measurements of Leclercq and de Langre [14]. We presume it comes from experimental features, due to important inertia effects that our model of hydrodynamic forces is unable to capture (non-symmetry is also present in experiments for the low pulsation and short displacement, and for high pulsation and moderate and high displacements, see top left, bottom centre, and bottom right in Figure 7.6). This minor discrepancy, nevertheless, does not alter the overall comparison and the shapes remain fairly similar.

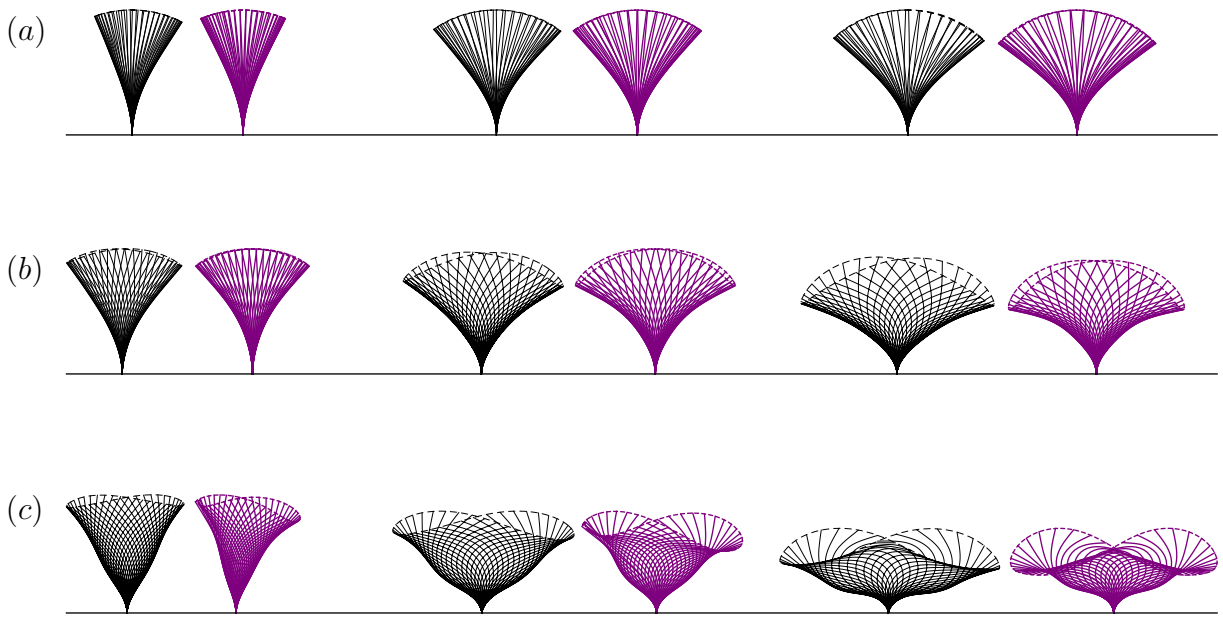

Figure 7.6 Deformation profiles of the plate experiments (black) of Leclercq and de Langre [14] and rod simulations (purple) for the dimensionless flow pulsations $\omega = \Omega t_s$ equal to (a) 0.38, (b) 1.07, and (c) 2.01. In each case, the dimensionless actuator amplitude $\alpha = A/L$ goes from 0.27 (left), to 0.46 (middle), and 0.65 (right). The numerical equivalent case is a rod under an oscillating flow of upstream velocity in equation (7.63). The aspect ratio of the plate and rod is $\Gamma = 10$. The dashed lines represent the trajectory of the plate and rod tips.

7.6 Simulation results

The code being verified and validated, we present simulations of a rod to visualise the deformation in time and see how faithfully it depicts the motion of a living soft coral branch.

7.6.1 Problem statement

In a first set of simulations, we subjected the rod to an upstream flow that ascends linearly from $t = 0$ to $t = t_\mathrm{s}$ and plateaus afterwards, as shown in Figure 7.7(a)

$$U(t) = U_0 \min\left(1, \frac{t}{t_\mathrm{s}}\right), \tag{7.65}$$

recalling that $t_\mathrm{s} = L^2\sqrt{m_\mathrm{l}/EI}$ is the characteristic time for the structural deformation. This preliminary case illustrates how a soft coral branch would reconfigure and vibrate if it stands in a continuous, unidirectional water flow, such as in water flume experiments.

A second set of simulations considers the action of a gentle wave during one period $T_\mathrm{wave} = 20t_\mathrm{s}$, shown in Figure 7.7($b$)

$$U(t) = U_0 \sin\left(\frac{2\pi t}{T_\mathrm{wave}}\right). \tag{7.66}$$

This case is closer to the reality as the seawater speed descends back right after the complete reconfiguration of the coral.

We varied the Cauchy number C_Y from 1 to 500. Provided the expression in equation (7.23), a small C_Y physically reflects the case of either a low water flow speed (deep waters), a stiff coral, or a short branch, whereas a large C_Y reflects the case of either a high water flow speed (shallow waters), a bendy coral, or a long branch. The reduced velocity varies accordingly as

$$U_\mathrm{r} = \frac{StU_0t_\mathrm{s}}{D} = \frac{StU_0L^2}{D}\sqrt{\frac{m_\mathrm{l}}{EI}} = St\sqrt{\frac{\pi\Gamma C_\mathrm{Y}}{4}\chi}, \tag{7.67}$$

where

$$\chi = \frac{m_\mathrm{l}L}{\pi\rho_\mathrm{f}LD^2/4} \tag{7.68}$$

is the ratio of the structural mass to the added mass. Without further investigation about the coral composition and its density, we consider here the simple case $\chi \sim 1$. Besides, based on an online video of a vibrating soft coral [17], we took a rod having an aspect ratio of $\Gamma = 25$.

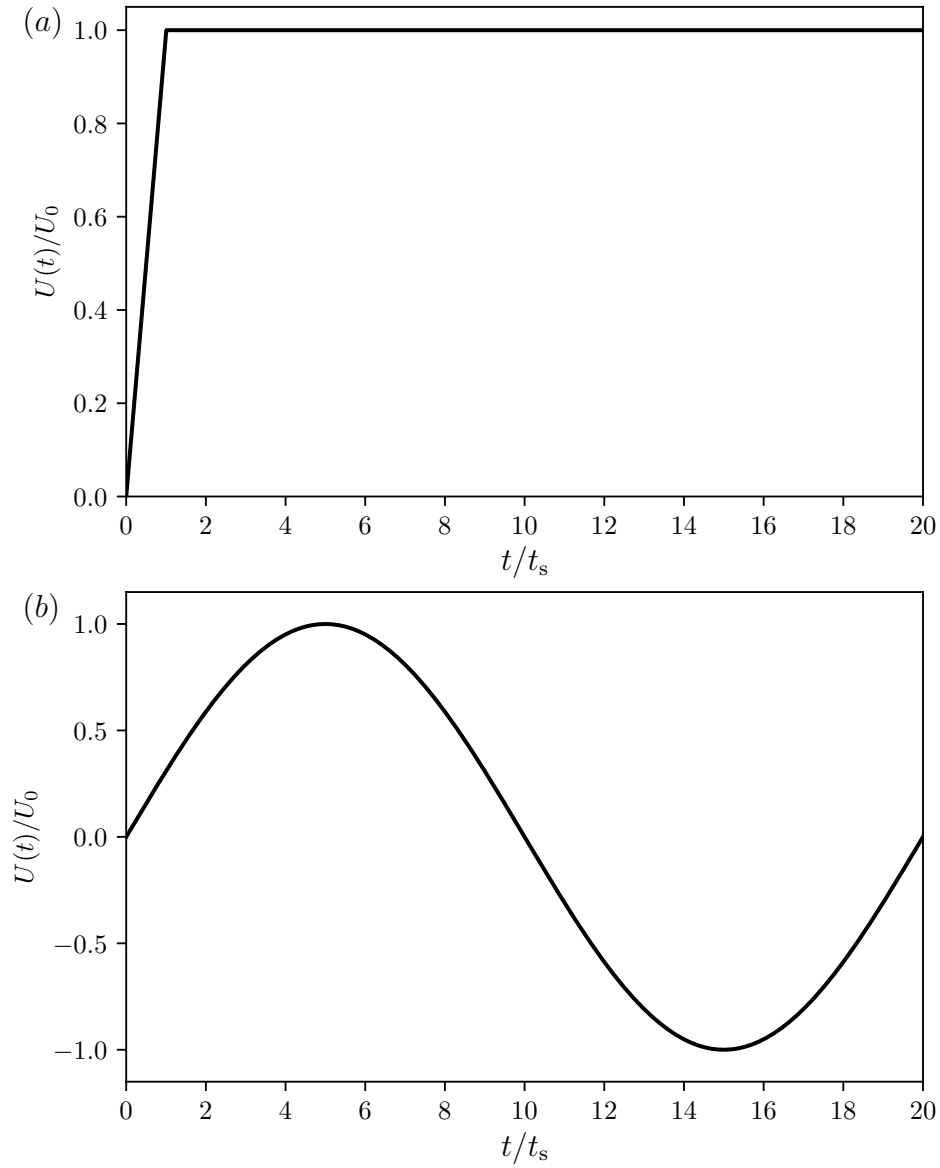

Figure 7.7 Time profile of the flow speed for the simulation cases: (a) unidirectional flow and (b) wave surge.

7.6.2 Unidirectional flow

We present first, in Figure 7.8, the stream-wise and transverse tip displacements of a rod under a unidirectional flow stream. We note that the rod dynamics go through two stages. The first stage is the *reconfiguration* process, where the rod bends without transverse motion as a response to the flow stream. Once it totally reconfigures, the vortex-induced lift takes over, excites the rod and reaches the limit-cycle. This is the *vortex-induced vibration* stage. Although VIV affect also the stream-wise displacement (small oscillations in the plateau), this latter remains negligible compared to the transverse displacement. This two-phase dynamics (reconfiguration + vortex-induced vibrations) is also seen in the real vibrating soft coral [17].

On the other hand, VIV lead to different transverse displacement modes depending on the Cauchy number. In Figure 7.9, we present the frontal and lateral deformation of the rod for $1 \leq C_{\mathrm{Y}} \leq 500$. When the flow speed is moderate, the Cauchy number is low, the rod resists the drag and does not bend much. In this case, the frontal profile of the rod resembles the first modal shape of a cantilever. When the flow speed gets stronger, however, the Cauchy number increases, and the rod curves more with the flow. We can notice in Figure 7.9, for Cauchy numbers $5 \leq C_{\mathrm{Y}} \leq 50$, that the important displacements are located at the tip and the middle of the rod, like the second modal shape of a cantilever. If the coral had longer branches, for instance, they would streamline even more with the flow since the Cauchy number would take higher values. In Figure 7.9 we can distinguish the formation of a second zero-displacement node for $75 \leq C_{\mathrm{Y}} \leq 250$, and barely a third one for $C_{\mathrm{Y}} \geq 300$, meaning that the rod transitions into high order modal shapes. It appears from the online video [17] that the deformation of bipinnate sea plume branches looks more like the simulation cases of Cauchy numbers $1 \leq C_{\mathrm{Y}} \lesssim 50$. In fact, branches are not extremely bent, and the transverse displacements have either none or only one zero-displacement node, i.e. first and second modal deformations.

Regarding the area facing the stream, rods under moderate and high Cauchy numbers have relatively small transverse amplitudes with multiple nodes. In addition, we notice that they bend considerably. As a consequence, the frontal exposure area shrinks: the rod covers a small effective area of capture, and is less likely to intercept particles. The rod with low Cauchy number is no more likely to intercept particles, because even if the transverse span is important and the exposure area is larger, the motion is slow, which would let many particles escape and lead to a loss in capture. Thus, a trade-off is imposed, indicating the existence of an optimal combination of fluid and structural properties that verifies the best capture rate.

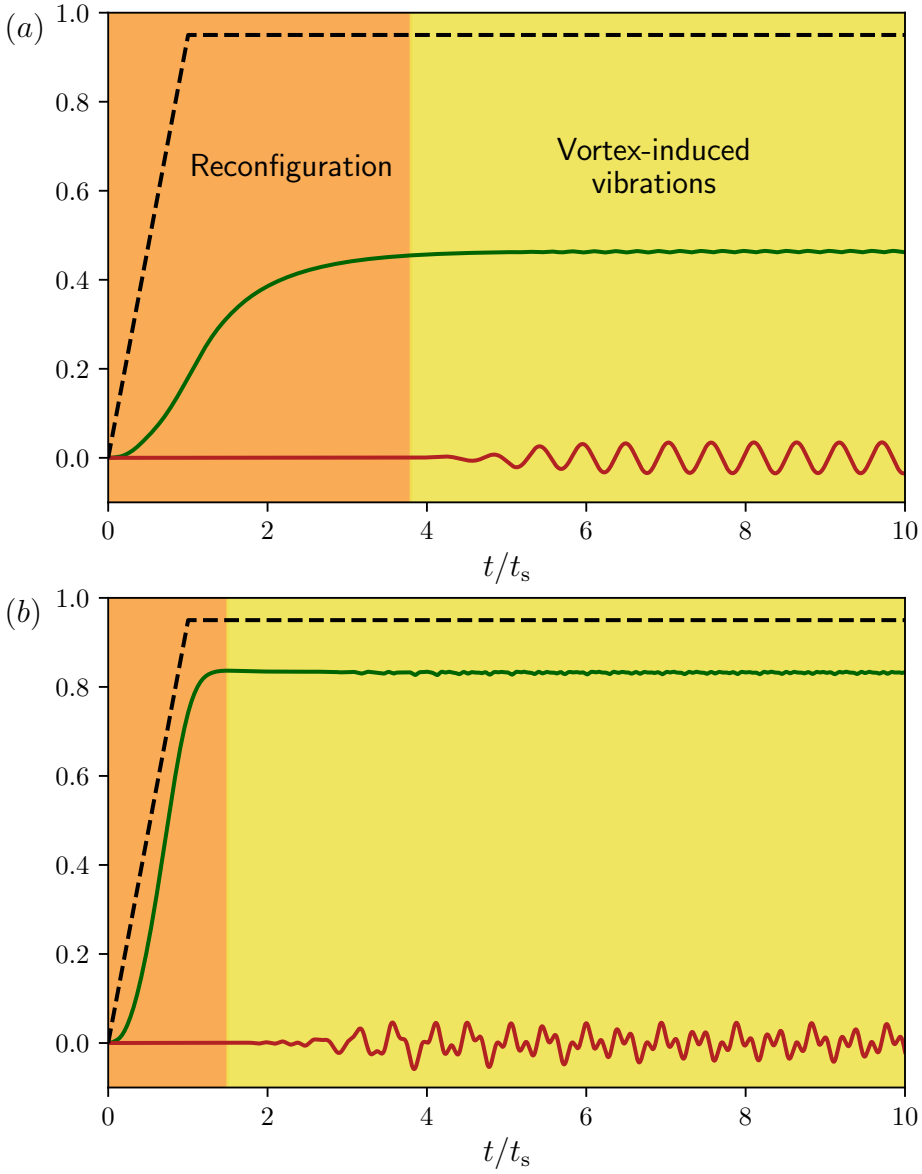

Figure 7.8 Time plot of the stream-wise $w_0 = \boldsymbol{w} \cdot \boldsymbol{u}_0$ (——) and transverse $w^{\perp} = \boldsymbol{w} \cdot \boldsymbol{u}_0^{\perp}$ (——) displacements of the tip at (*a*) $C_{\mathrm{Y}} = 5$ and (*b*) $C_{\mathrm{Y}} = 100$, in the case of a unidirectional current. The dashed line (- - - - -) corresponds to the variation of the flow speed $U(t)$ (not to scale). After that the rod streamlines with the flow and reaches a final reconfigured shape (orange area), vortex-induced vibrations arise (yellow area). We see that increasing the Cauchy number bends the rod and triggers VIV more rapidly.

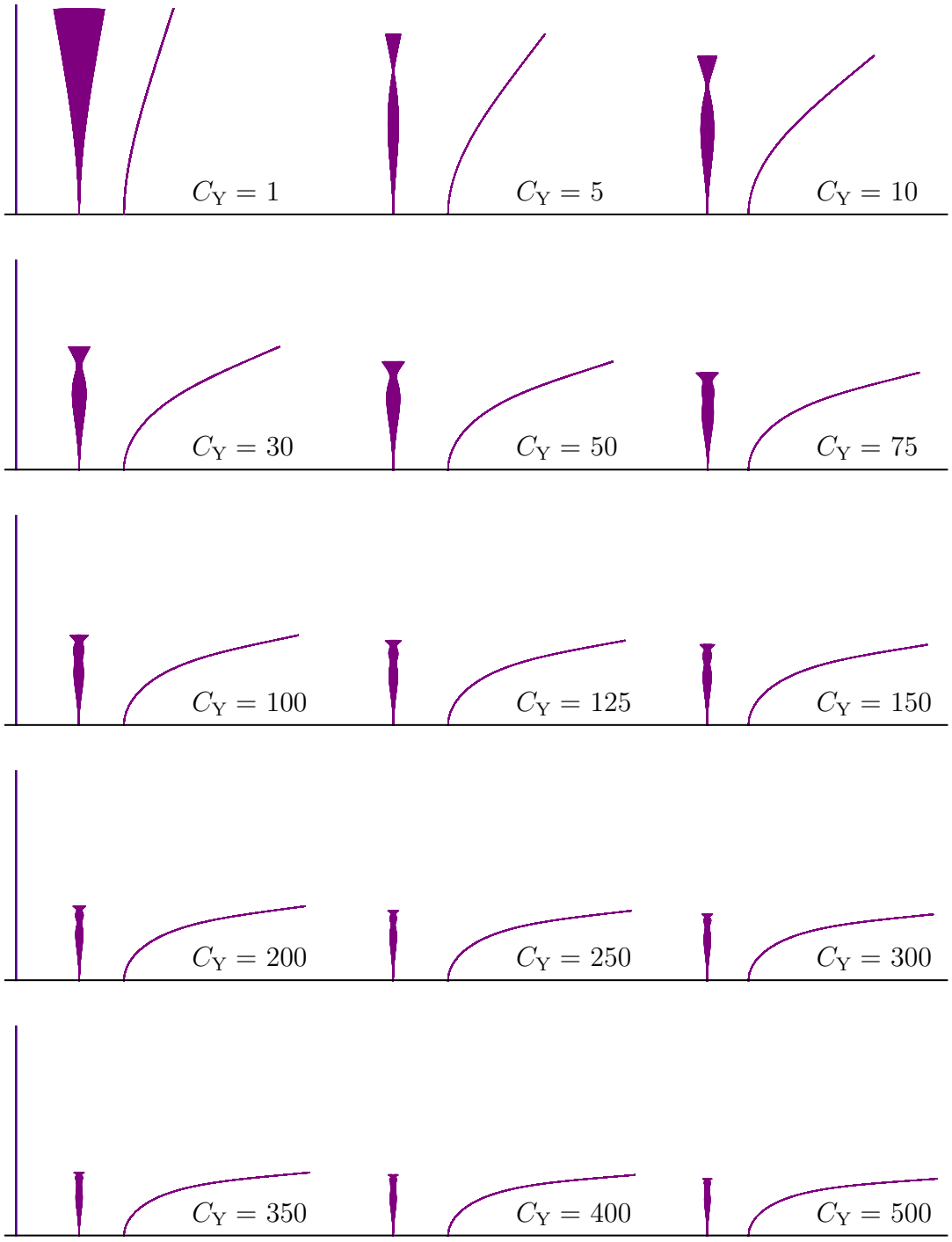

Figure 7.9 Frontal and lateral profiles of the rod in the case of a unidirectional flow. The vertical line in the left is a scale referring to the initial position of the rod.

7.6.3 Wave surge

Here we tackle the more natural case of a rod under a wave surge during a period. Figure 7.10 compares the transverse and stream-wise tip displacements of a rod under unidirectional and oscillatory flows. In this latter case also, the onset of the VIV synchronises with the complete bending of the rod. The difference is that the rod stays at this reconfiguration state only during the peak of the wave surge. As soon as the flow speed starts to drop, the hydrodynamic drag relaxes and the rod returns back, progressively, to its initial state. The result that we found interesting during this phase is that the VIV do not fade away and the rod keeps vibrating while returning to its initial state. Subsequently, the rod sweeps a more expanded area, and the effective area of capture is larger than in the unidirectional flow case. The presence of waves in the flow is thence important, from a nutritional point of view, in the life of a soft coral, suggesting that the outcome of particle capture experiments in water flume should be taken with reserve. Also it makes sense why it is recommended to ensure a wave generator in aquarium before one purchases soft corals...

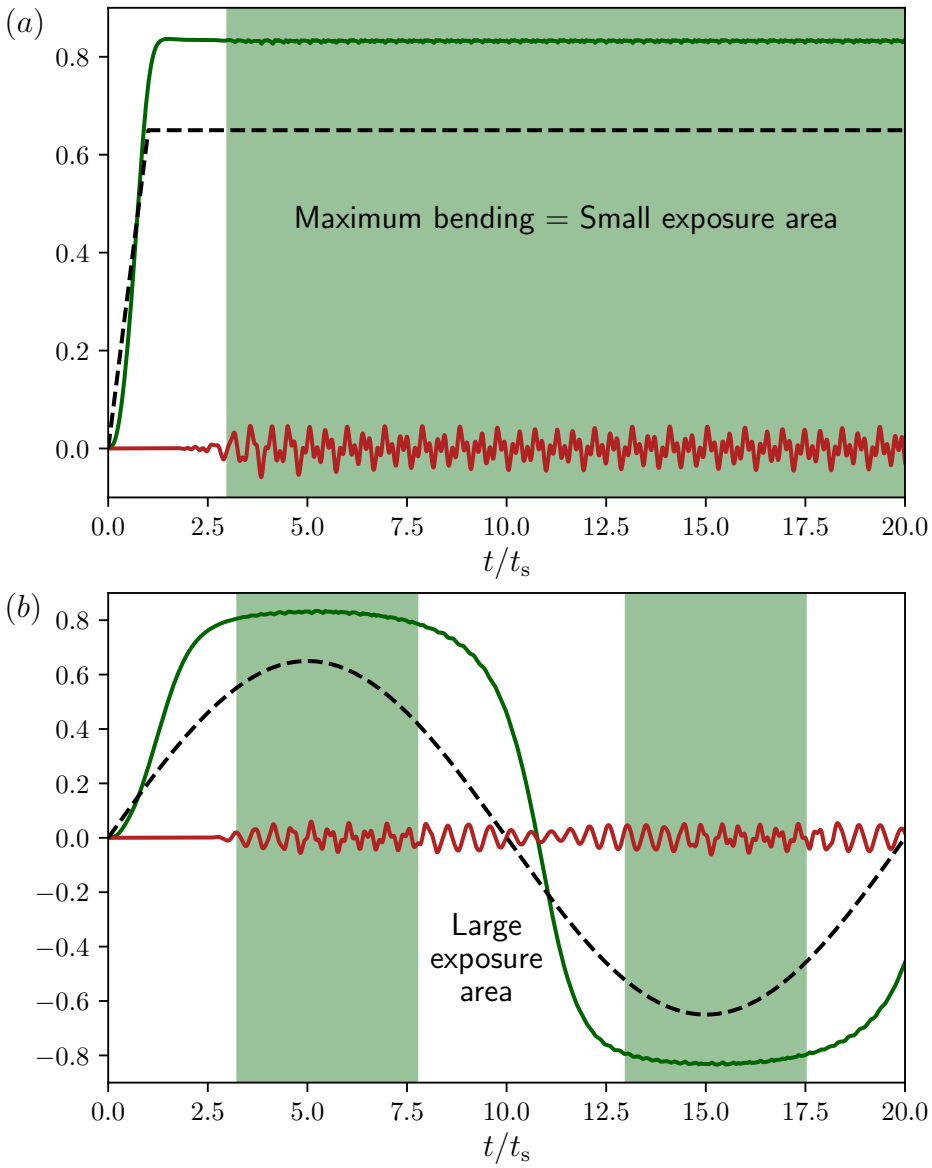

Figure 7.10 Time plot of the stream-wise $w_0 = \boldsymbol{w} \cdot \boldsymbol{u}_0$ (——) and transverse $w^{\perp} = \boldsymbol{w} \cdot \boldsymbol{u}_0^{\perp}$ (——) displacements of the tip in the case of (a) a unidirectional flow and (b) a wave surge, with the dashed line (- - - - -) showing the variation of the flow speed $U(t)$ (not to scale). Both cases have a Cauchy number of $C_{\mathrm{Y}} = 100$. The coloured area refers to the phase where the rod is completely bent, in which case VIV are present and the frontal area facing the stream is small.

CHAPTER 8 DISCUSSION AND CONCLUSION

8.1 General summary of the particle capture model

The main take-home message from chapters 5 and 6 is that vortex-induced vibrations are beneficial for particle interception at the synchronisation range of reduced velocities. We showed that a two-degree-of-freedom oscillating cylinder can capture up to 40% more particles under VIV at lock-in than in the absence of vibration.

We found that the mean capture efficiency (also dimensionless capture rate in our case) is the product of two independent functions

$$\langle \eta \rangle = \langle \eta \rangle_{\text{fixed}} \, (1 + \delta) \, . \tag{8.1}$$

The factor $\langle \eta \rangle_{\text{fixed}}$ is the *scale* of $\langle \eta \rangle$ that gives the order of magnitude of the capture rate, and depends on the properties of the flow through the Reynolds number Re and the advected particles through the diameter ratio R. We can describe the role of the boundary layer as a 'shield' that protects the cylinder from incident particles, which weakens with increasing Reynolds number due to its thinning. For small particles, or bigger ones in viscous flows, the mean capture rate of a fixed cylinder scales as $\langle \eta \rangle_{\text{fixed}} \sim R^2 Re^{1/2}$.

Once the magnitude of the efficiency is determined, δ quantifies the *gain* in particle capture due to VIV. As a function of the reduced velocity U_{r}, it has a bell-shaped variation, with a peak at the synchronisation range of frequencies. Accordingly, δ depends on the geometrical characteristics of the lemniscate limit-cycle trajectory of the cylinder, such as the amplitudes Y_{max} and X_{max}, the slenderness ratio γ, and the distortion factor β. In particular, the gain δ increases with the distance the cylinder travels against the stream, namely the counter-current distance d_{cc}. Indeed, incident particles boost their relative momentum with respect to the cylinder frame of reference and penetrate easily into the boundary layer. This explanation of the capture efficiency by the counter-current distance is kinematic and encompasses, therefore, the idea of 'additional momentum' of Krick and Ackerman [109], which is based on the cylinder momentum in the transverse direction only.

It is worth to mention that δ is well correlated with the kinematic parameters of the cylinder at lock-in (large Y_{max} and X_{max}, low γ), yet we still miss a clear trend in the range where the capture is detrimental (low Y_{max} and X_{max}, large γ). Therefore, instead of shortly saying that capture increases or decreases with the cylinder amplitudes, we cautiously emphasise that this statement is true only beyond certain critical amplitudes ($Y_{\text{max}}, X_{\text{max}} > Y^*_{\text{max}}, X^*_{\text{max}}$,

$\gamma < \gamma^*$). We point out, though, that the existence of a detrimental regime might be peculiar to the rigid cylinder which has a single frequency, and becomes irrelevant in the case of a flexible slender structure which has multiple natural frequencies. Indeed, if two lock-in frequencies are relatively close to each other, the gain in capture would not find any gap to drop below zero. Thus, once it decreases after the first peak, it shall increase again and reach the following peak, and so forth for each lock-in range corresponding to each mode of vibration of the flexible slender structure. For this reason, a real flexible cylinder may not have any detrimental regime at all, and VIV would be beneficial irrespective of the reduced velocity.

8.2 Limitations

Regarding the motion of the cylinder, we decided, for the sake of simplicity, to keep the mass number constant at $M = 1$, and neglect the structural damping $\zeta = 0$. Since the amplitude response of the cylinder decreases with the product $M\zeta$ [78], we expect that the capture rate would also decrease as a consequence of the correlation $\delta = \delta(Y_{\max})$ we obtained in Figure 6.5(a).

Concerning the particles, we simulated trajectories using a single density value ρ_{p}. For denser particles, the capture rate would increase because they would carry more inertia, deviate less, and be more likely to hit the cylinder. In the Reynolds number range we considered in our project ($Re \sim 100$), the simulations of Espinosa-Gayosso *et al.* [141] showed that heavy particles ($\rho^+ = 2.6$) score a higher capture rate than neutrally buoyant ones ($\rho^+ = 1$). How does the capture rate increase with density? We let the door open for a parametric study to determine a potential power law scaling.

Even though it was ignored in previous works, we deemed the added mass force on particles relevant to be included in the present project. Yet, we took an always constant mass coefficient C_{m}, which is an assumption that becomes invalid when the particle gets close to the cylinder wall. The confinement effects would become important and prevent the particle from hitting the wall, which also means that C_{m} would increase considerably during the approach. Future simulations might consider C_{m} as a function of the distance to the wall, or model the subsequent repulsive force and include it in the momentum equation [142].

Lastly, the purpose of the elastic rod simulations in chapter 7 was mainly qualitative and we did not have the opportunity to dig into quantitative aspects. We encourage forthcoming projects to take over these simulations and investigate, for instance, how the Cauchy number, or equivalently the reduced velocity, influences the deformation profile, the amplitude

responses, or the effective capture area. Besides, given that soft corals grow within the seabed boundary layer, it would be fruitful to consider a non-uniform water speed, which is more reasonable for corals that have branches emerging non-perpendicular, inclined upwards from the main stem (like in Figure 3.2). Another possible improvement of the model would be to add a stream-wise component in the vortex-induced load, so that the rod may exhibit a lemniscate limit-cycle trajectory.

8.3 Into a realistic soft coral branch

8.3.1 Motility and Brownian motion

Medium and large size food particles are usually motile, and can actively change their trajectories, for example by swimming. One way to include the motility in the particle trajectory integration is to add a random displacement at each time step

$$\boldsymbol{x}_{\mathrm{p},n+1} = \boldsymbol{x}_{\mathrm{p},n} + \Delta t \boldsymbol{u}_{\mathrm{p},n} + \delta \boldsymbol{x}^{\mathrm{random}}. \tag{8.2}$$

The magnitude $\left|\left|\delta \boldsymbol{x}^{\mathrm{random}}\right|\right|$ shall be proportional to, or positively correlated with, the mobility coefficient μ, the ambient temperature T, as well as decreasing with the upstream flow velocity U_0. A possible multiplicative factor could be the dimensionless index N_{M} proposed by Rubenstein and Koehl [100]

$$N_{\mathrm{M}} = \frac{\mu k T}{U_0 D}, \tag{8.3}$$

where k is the Boltzmann constant.

On the other hand, the time cost was a major limitation in simulating trajectories of very small particles (e.g. organic debris), because the upper bound of the time step decreases as the square of the particle size. Since these types of particles might be subjected to Brownian motion, one can circumvent this hurdle by solving transient advection-diffusion equations for scalar transport. The capture rate can then be extracted from the distribution of the scalar concentration around the cylinder edge.

8.3.2 Capture criterion

To describe the capture process, we assumed that a particle is retained as soon as it encounters the cylinder edge (i.e. capture = encounter + retention). A possible improvement of the capture criterion is to model a retention duration τ_{ret} for each particle that depends on the momentum at the position of the encounter. We think, for example, that a particle hitting

the cylinder straight at the front with high momentum would stay firmly implanted for a longer duration (long τ_{ret}) than one landing slowly on its edge (short τ_{ret}). The value of τ_{ret} might wax and wane whether the soft coral is slimy and secretes continuous mucus (extend τ_{ret}) or the particle is motile and strives to detach quickly from the branch (e.g. zooplankton, reduce τ_{ret}). Finally, setting a critical retention duration T_{ret}, the particles verifying $\tau_{\text{ret}} \geq T_{\text{ret}}$ would be counted as captured.

In reality, polyp tentacles activate and stretch when prey are near, and capture them before hitting the soft coral branch. Instead of a solid contact, an elaborate criterion of capture would consider 'danger zones' having areas related to the tentacle reach. Because motile particles can dodge between tentacles and escape capture, each danger zone would have a specific probability of a successful catch. This probability would depend on the polyp angular position relative to the flow as well, since polyps in the front and the sides are more likely to capture particles than those in the rear [32].

8.3.3 Third dimension

The capture rate $\dot{N}$ and the amplitudes $Y_{\max}$ and $X_{\max}$ have the same frequency response. We infer that this result remains valid even if the cylinder has multiple natural frequencies. Thus, we may extend our two-dimensional correlation between the capture rate $\dot{N}$ and the transverse amplitude $Y_{\max}$ into a three-dimensional capture rate. Suppose we find the transverse vibration envelope $Y_{\max}(s)$, $s \in [0, L]$, of a rod of length L with a clamped end, such as the results presented in Figure 7.9. Then we can decompose the structure into small elements of length ds, and calculate the total rate as

$$\dot{N}_{\text{3D}} = \int_0^L \dot{N}_{\text{2D}}(Y_{\max})\mathrm{d}s. \tag{8.4}$$

This idea is possible to implement with a finite element analysis as in chapter 7, or a reduced-order model like the one proposed by Leclercq and de Langre [85]. If the real arborescent morphology of soft corals is taken into account, then it is worth importing a whole 3D scan (e.g. computed tomography scan). A prospective work might extract its principal spatial and temporal modes [22–24], and apply the formula (8.4). Another option is to compute three-dimensional DNS of the fluid-particle problem. This procedure has the advantage to delineate the fluid flow around morphological details, and has been used in biomedical simulations [143].

The 3D scan also gives the possibility to 3D-print a whole soft coral for experiments. If desired, the size of the branch can be magnified (for example to facilitate particle counting)

while rescaling the flow variables. Rather than conducting experiments on real corals, this technique is non-invasive, and permits the repetition of experiments several times, for long durations, without caring about the living conditions of species such as light exposure, water cleaning, etc. It also has the benefit of experimenting particle interception over different species, and analyse the role of each branch morphology in the capture process. This idea was already tested for some marine organisms [144].

8.4 Biological implications

One of the main outcomes of our simulations is the existence of an optimal reduced velocity $U_{\mathrm{r}}^{\mathrm{opt}}$ that ensures the maximum capture rate, which corresponds to the lock-in frequency $U_{\mathrm{r}}^{\mathrm{opt}} \approx 5$. Since the reduced velocity, in our harmonic oscillator model, is inversely proportional to the square root of the spring stiffness, a cylinder which is too stiff or too soft would bring U_{r} into low or high values, then without any noticeable gain in capture. Therefore, assuming that the same conclusions persist for a cross-section of a real soft coral, this latter must have an optimal stiffness that guarantees the best capture rate.

Because the soft coral branches are attached into the main vertical stem, they structurally resemble an elastic rod. In this case, the reduced velocity reads as in equation (7.67)

$$U_{\mathrm{r}} = St\frac{U_0}{D}\sqrt{\frac{mL^4}{EI}}, \tag{8.5}$$

where St is the Strouhal number, L the length of the branch, m the mass per unit length (including the added mass), E the Young's modulus, and I the moment of inertia. Given that $I \sim D^4$, and writing $m \sim \rho D^2$, we see that the optimal properties of the soft coral branch have to verify

$$StU_0\left(\frac{\rho}{E}\right)^{1/2}\frac{L^2}{D^2} \sim U_{\mathrm{r}}^{\mathrm{opt}}(= \text{constant} \approx 5). \tag{8.6}$$

Introducing the speed (of sound) $c_{\mathrm{s}} = \sqrt{E/\rho}$ and the aspect ratio $\Gamma = L/D$, we obtain

$$\frac{\Gamma^2 U_0}{c_{\mathrm{s}}} = \text{constant}, \tag{8.7}$$

or equivalently

$$\frac{c_{\mathrm{s}}}{\Gamma^2} \propto U_0. \tag{8.8}$$

This equation links the morphological properties of the soft coral (Γ and c_{s}) on the left-hand

side with the ambient water speed (U_0) on the right-hand side.

Does this relation mean that soft corals exhibit morphological plasticity according to the local predominant currents? If so, which mechanical property is the most appropriate for soft corals to tune? A basic reasoning based on the relation (8.8) reveals that in deep waters where the flow is globally calm (small U_0), soft corals would need either thin branches (slender phenotype, large Γ), or a soft skeleton (small c_s). Conversely, in shallow waters where the flow is turbid (high U_0), they would need either thick branches (stout, bushy phenotype, small Γ), or a stiff skeleton (large c_s). Here a physiological compromise is necessary between choosing to tune the aspect ratio Γ or the stiffness represented by c_s. Indeed, a deep-water soft coral with both thin branches and soft skeleton is probably too weak to resist external endeavours (predators for instance). Similarly, a shallow-water soft coral with both thick branches and stiff skeleton would require too much energy to maintain a proper metabolism. We hypothesise that tuning the aspect ratio Γ is the preferred solution. This fact is supported by the measurements of Jeyasuria and Lewis [53] and Sanchez *et al.* [49], and can also be inferred if we notice that the aspect ratio is squared in equation (8.8).

Then, is geographical distribution of soft coral species linked with the turbidity? Biologists might set up in-field expeditions to collect data and inquire into this issue. From a mechanical viewpoint, equation (8.8) may be refined since the capture depends also on the degree of reconfiguration of the branch as well as the effect of buoyancy, among other factors. Hence, combining biological evidence and mechanical calculations will provide exciting models for predicting soft coral distribution in ocean.

8.5 Bioinpiration

Studying soft coral vibrations led us to give results on the efficiency of a vibrating collector. These results might be worth to consider in projects dealing with dust and pollutant filtering, especially in industries where hygiene measures are high and strict (e.g. food, pharmaceutical industries).

As we dealt with flexible structures under VIV, the present research can be intended to design bioinspired energy harvesters in the sea. At the time when VIV represent a major threat to offshore energy production, introducing a marine energy harvester will be a rewarding incentive for engineers to seek – instead of suppress – VIV and use them as a principal supplier to harness clean and renewable energy.

Last but not least, the vibrating soft coral might serve as a paradigm in biomimetics. We thought about crafting smart scarecrows in farms to actively prevent birds from picking

crops and seeds. Smart scarecrows shall be placed against the ambient wind direction, and fabricated with materials such that the lock-in reduced velocity corresponds to the local wind speed. A breeze will then shake the scarecrow arms up, and create an impression of a real human chasing birds!

REFERENCES

[1] E. Naudascher and D. Rockwell, *Flow-induced vibrations: an engineering guide*. Courier Corporation, 2009.

[2] Nova Southeastern University, "South Florida Octocorals: A Guide to Identification," Aug. 2016. [Online]. Available: http://nsuworks.nova.edu/octocoral_guide/

[3] F. H. Martín, "Muricea elongata." Aug. 2005. [Online]. Available: https://commons.wikimedia.org/wiki/File:Muricea_elongata.jpg

[4] T. K. bin Sultan Living Oceans Foundation, "Living Oceans Foundation." [Online]. Available: https://www.livingoceansfoundation.org/

[5] M. Kieffer, "Sea fan coral in key largo, florida." Nov. 2004. [Online]. Available: https://tinyurl.com/y56dugfr

[6] M. Slattery, M. S. Pankey, and M. P. Lesser, "Annual Thermal Stress Increases a Soft Coral's Susceptibility to Bleaching," *Scientific Reports*, vol. 9, no. 1, pp. 1–10, May 2019, number: 1 Publisher: Nature Publishing Group. [Online]. Available: https://www.nature.com/articles/s41598-019-44566-9

[7] J. Wagner, "Visualisation of the von kármán vortex sheet behind a circlular cylinder in air flow." Oct. 2014. [Online]. Available: https://commons.wikimedia.org/wiki/File:Karmansche_Wirbelstr_kleine_Re.JPG

[8] M. L. Facchinetti, E. de Langre, and F. Biolley, "Vortex-induced travelling waves along a cable," *European Journal of Mechanics - B/Fluids*, vol. 23, no. 1, pp. 199–208, Jan. 2004. [Online]. Available: http://www.sciencedirect.com/science/article/pii/S099775460300102X

[9] Y. Tamura, "Wake-oscillator model of vortex-induced oscillation of circular cylinder," *Journal of Wind Engineering*, vol. 1981, no. 10, pp. 13–24, 1981, publisher: Japan Association for Wind Engineering.

[10] N. E. L. Haugen and S. Kragset, "Particle impaction on a cylinder in a crossflow as function of Stokes and Reynolds numbers," *Journal of Fluid Mechanics*, vol. 661, pp. 239–261, Oct. 2010. [Online]. Available: https://doi.org/10.1017/S0022112010002946

[11] A. Espinosa-Gayosso *et al.*, "Particle capture and low-Reynolds-number flow around a circular cylinder," *Journal of Fluid Mechanics*, vol. 710, pp. 362–378, Nov. 2012. [Online]. Available: https://doi.org/10.1017/jfm.2012.367

[12] ——, "Particle capture by a circular cylinder in the vortex-shedding regime," *Journal of Fluid Mechanics*, vol. 733, pp. 171–188, Oct. 2013. [Online]. Available: https://doi.org/10.1017/jfm.2013.407

[13] M. E. Weber and D. Paddock, "Interceptional and gravitational collision efficiencies for single collectors at intermediate Reynolds numbers," *Journal of Colloid and Interface Science*, vol. 94, no. 2, pp. 328–335, Aug. 1983. [Online]. Available: http://www.sciencedirect.com/science/article/pii/0021979783902709

[14] T. Leclercq and E. de Langre, "Reconfiguration of elastic blades in oscillatory flow," *Journal of Fluid Mechanics*, vol. 838, pp. 606–630, Mar. 2018. [Online]. Available: https://doi.org/10.1017/jfm.2017.910

[15] R. Blevins, *Flow-induced vibration.* Van Nostrand Reinhold, 1990.

[16] T. Sarpkaya, "A critical review of the intrinsic nature of vortex-induced vibrations," *Journal of Fluids and Structures*, vol. 19, no. 4, pp. 389–447, May 2004. [Online]. Available: http://www.sciencedirect.com/science/article/pii/S0889974604000350

[17] Youtube, "Caribbean Spiny Lobster and a Bipinnate Sea Plume coral," 2013. [Online]. Available: https://youtu.be/1mgAyFgYfYw

[18] E. de Langre, "Effects of Wind on Plants," *Annual Review of Fluid Mechanics*, vol. 40, no. 1, pp. 141–168, 2008. [Online]. Available: https://doi.org/10.1146/annurev.fluid.40.111406.102135

[19] F. P. Gosselin, "Mechanics of a plant in fluid flow," *Journal of Experimental Botany*, vol. 70, no. 14, pp. 3533–3548, Jul. 2019. [Online]. Available: https://academic.oup.com/jxb/article/70/14/3533/5518960

[20] F. Gosselin, E. de Langre, and B. A. Machado-Almeida, "Drag reduction of flexible plates by reconfiguration," *Journal of Fluid Mechanics*, vol. 650, p. 319, May 2010. [Online]. Available: http://www.journals.cambridge.org/abstract_S0022112009993673

[21] J. Lei and H. Nepf, "Blade dynamics in combined waves and current," *Journal of Fluids and Structures*, vol. 87, pp. 137–149, May 2019. [Online]. Available: http://www.sciencedirect.com/science/article/pii/S0889974618306996

[22] M. Rodriguez, E. de Langre, and B. Moulia, "A scaling law for the effects of architecture and allometry on tree vibration modes suggests a biological tuning to modal compartmentalization," *American Journal of Botany*, vol. 95, no. 12, pp. 1523–1537, Dec. 2008. [Online]. Available: https://onlinelibrary.wiley.com/doi/abs/10.3732/ajb.0800161

[23] M. Rodriguez *et al.*, "The multimodal dynamics of a walnut tree: experiments and models," *Journal of Applied Mechanics*, vol. 79, no. 4, p. 044505, 2012. [Online]. Available: https://manufacturingscience.asmedigitalcollection.asme.org/data/Journals/JAMCAV/26820/044505_1.pdf

[24] C. Der Loughian *et al.*, "Measuring local and global vibration modes in model plants," *Comptes Rendus Mécanique*, vol. 342, no. 1, pp. 1–7, Jan. 2014. [Online]. Available: https://linkinghub.elsevier.com/retrieve/pii/S1631072113001319

[25] H. J. Lugt, *Vortex Flow in Nature and Technology*, 1995th ed. Malabar, Fla: Krieger Pub Co, Jun. 1995.

[26] C. Truesdell, *The Kinematics of Vorticity*. Courier Dover Publications, Oct. 2018.

[27] J.-Z. Wu, H.-y. Ma, and M.-D. Zhou, *Vorticity and Vortex Dynamics*. Springer Science & Business Media, Apr. 2007.

[28] M. M. Chance and D. A. Craig, "Hydrodynamics and behaviour of Simuliidae larvae (Diptera)," *Canadian Journal of Zoology*, vol. 64, no. 6, pp. 1295–1309, Jun. 1986, publisher: NRC Research Press. [Online]. Available: https://www.nrcresearchpress.com/doi/abs/10.1139/z86-193

[29] L.-E. Widahl, "Flow Patterns around Suspension-Feeding Mosquito Larvae (Diptera: Culicidae)," *Annals of the Entomological Society of America*, vol. 85, no. 1, pp. 91–95, Jan. 1992, publisher: Oxford Academic. [Online]. Available: https://academic.oup.com/aesa/article/85/1/91/93739

[30] S. Kim *et al.*, "Vortex-induced dispersal of a plant pathogen by raindrop impact," *Proceedings of the National Academy of Sciences*, vol. 116, no. 11, pp. 4917–4922, Mar. 2019, publisher: National Academy of Sciences Section: Biological Sciences. [Online]. Available: https://www.pnas.org/content/116/11/4917

[31] S. A. Wainwright and J. R. Dillon, "On the orientation of sea fans (Genus Gorgonia)," *Biol Bull*, vol. 136, 1969. [Online]. Available: https://doi.org/10.2307/1539674

[32] G. J. Leversee, "Flow and feeding in fan-shaped colonies of the gorgonian coral, leptogorgia," *The Biological Bulletin*, vol. 151, no. 2, pp. 344–356, Oct. 1976. [Online]. Available: https://www.journals.uchicago.edu/doi/abs/10.2307/1540667

[33] M. P. Paidoussis, *Fluid-Structure Interactions: Slender Structures and Axial Flow*. Academic Press, Oct. 1998.

[34] C. Grouthier *et al.*, "On the efficiency of energy harvesting using vortex-induced vibrations of cables," *Journal of Fluids and Structures*, vol. 49, pp. 427–440, 2014.

[35] M. M. Bernitsas *et al.*, "VIVACE (Vortex Induced Vibration Aquatic Clean Energy): A New Concept in Generation of Clean and Renewable Energy From Fluid Flow," *Journal of Offshore Mechanics and Arctic Engineering*, vol. 130, no. 4, pp. 041 101–041 101, Sep. 2008. [Online]. Available: http://dx.doi.org/10.1115/1.2957913

[36] D. J. Y. Villarreal, "Vortex resonance wind turbine," U.S. Patent 13/811,788, Aug., 2011.

[37] W. B. Hobbs and D. L. Hu, "Tree-inspired piezoelectric energy harvesting," *Journal of fluids and Structures*, vol. 28, pp. 103–114, 2012.

[38] S. Michelin and O. Doaré, "Energy harvesting efficiency of piezoelectric flags in axial flows," *Journal of Fluid Mechanics*, vol. 714, pp. 489–504, Jan. 2013, publisher: Cambridge University Press. [Online]. Available: https://doi.org/10.1017/jfm.2012.494

[39] V. Cognet *et al.*, "Bioinspired turbine blades offer new perspectives for wind energy," *Proceedings of the Royal Society A: Mathematical, Physical and Engineering Sciences*, vol. 473, no. 2198, p. 20160726, Feb. 2017. [Online]. Available: https://royalsocietypublishing.org/doi/full/10.1098/rspa.2016.0726

[40] P. Valdivia y Alvarado and K. Youcef-Toumi, "Design of Machines With Compliant Bodies for Biomimetic Locomotion in Liquid Environments," *Journal of Dynamic Systems, Measurement, and Control*, vol. 128, no. 1, pp. 3–13, Mar. 2006, publisher: American Society of Mechanical Engineers Digital Collection. [Online]. Available: https://asmedigitalcollection.asme.org/dynamicsystems/article/128/1/3/465199/Design-of-Machines-With-Compliant-Bodies-for

[41] F. M. Bayer, "The shallow-water Octocorallia of the West Indian region," *Studies on the Fauna of Curaçao and other Caribbean Islands*, vol. 12, no. 1, pp. 1–373, 1961.

[42] K. E. Fabricius, "Octocorallia," in *Encyclopedia of Modern Coral Reefs*. Springer Science & Business Media, 2011, pp. 740–745.

[43] T. T. Done, "Corals: environmental controls on growth," in *Encyclopedia of Modern Coral Reefs*. Springer Science & Business Media, 2011.

[44] T. Horton *et al.*, *World Register of Marine Species (WoRMS)*. WoRMS Editorial Board, Mar. 2020. [Online]. Available: https://www.marinespecies.org

[45] F. M. Bayer, "Key to the genera of Octocorallia exclusive of Pennatulacea (Coelenterata: Anthozoa), with diagnosis of new taxa," *Proceedings of the Biological Society of Washington*, 1981.

[46] M. Ribes, R. Coma, and J.-M. Gili, "Heterotrophic feeding by gorgonian corals with symbiotic zooxanthella," *Limnology and Oceanography*, vol. 43, no. 6, pp. 1170–1179, Sep. 1998, publisher: John Wiley & Sons, Ltd. [Online]. Available: https://aslopubs.onlinelibrary.wiley.com/doi/abs/10.4319/lo.1998.43.6.1170

[47] J. Shimeta and M. A. R. Koehl, "Mechanisms of particle selection by tentaculate suspension feeders during encounter, retention, and handling," *Journal of Experimental Marine Biology and Ecology*, vol. 209, no. 1, pp. 47–73, Feb. 1997. [Online]. Available: http://www.sciencedirect.com/science/article/pii/S0022098196026846

[48] A. C. Baker, "Reef corals bleach to survive change," *Nature*, vol. 411, no. 6839, pp. 765–766, Jun. 2001, number: 6839 Publisher: Nature Publishing Group. [Online]. Available: https://www.nature.com/articles/35081151

[49] J. A. Sánchez *et al.*, "Phenotypic plasticity and morphological integration in a marine modular invertebrate," *BMC Evolutionary Biology*, vol. 7, no. 1, p. 122, Jul. 2007. [Online]. Available: https://doi.org/10.1186/1471-2148-7-122

[50] N. J. Cadena and J. A. Sánchez, "Colony growth in the harvested octocoral Pseudopterogorgia acerosa in a Caribbean coral reef," *Marine Ecology*, vol. 31, no. 4, pp. 566–573, Dec. 2010. [Online]. Available: http://dx.doi.org/10.1111/j.1439-0485.2010.00397.x

[51] D. W. Whitman, A. A. Agrawal, and others, "What is phenotypic plasticity and why is it important," *Phenotypic plasticity of insects: Mechanisms and consequences*, pp. 1–63, 2009. [Online]. Available: http://www.eeb.cornell.edu/Agrawal/pdfs/whitman-and-agrawal-2009-Ch_1-Phenotypic-Plasticity-of-Insects.pdf

[52] D. Obura, "Adaptation," in *Encyclopedia of Modern Coral Reefs.* Springer Science & Business Media, 2011, pp. 9–13.

[53] P. Jeyasuria and J. Lewis, "Mechanical properties of the axial skeleton in gorgonians," *Coral reefs*, vol. 5, no. 4, pp. 213–219, 1987.

[54] S. Vogel, "Drag and flexibility in sessile organisms," *American Zoologist*, vol. 24, no. 1, pp. 37–44, 1984.

[55] I. Calixto-Botía and J. A. Sánchez, "A case of modular phenotypic plasticity in the depth gradient for the gorgonian coral Antillogorgia bipinnata (Cnidaria: Octocorallia)," *BMC Evolutionary Biology*, vol. 17, no. 1, Dec. 2017. [Online]. Available: http://bmcevolbiol.biomedcentral.com/articles/10.1186/s12862-017-0900-8

[56] NOAA, "How does pollution threaten coral reefs?" [Online]. Available: https://oceanservice.noaa.gov/facts/coral-pollution.html

[57] P. Enos, "Bahamas," in *Encyclopedia of Modern Coral Reefs.* Springer Science & Business Media, 2011, pp. 85–93.

[58] P. Kench, "Tsunami," in *Encyclopedia of Modern Coral Reefs.* Springer Science & Business Media, 2011, pp. 1096–1110.

[59] H. Cesar, L. Burke, and L. Pet-Soede, "The economics of worldwide coral reef degradation," 2003, publisher: International Coral Reef Action Network. [Online]. Available: http://agris.fao.org/agris-search/search.do?recordID=GB2013202743

[60] T. Spencer, "Temperature change: bleaching," in *Encyclopedia of Modern Coral Reefs.* Springer Science & Business Media, 2011, pp. 1079–1084.

[61] B. E. Brown, "Coral bleaching: causes and consequences," *Coral Reefs*, vol. 16, no. 1, pp. S129–S138, Jun. 1997. [Online]. Available: https://doi.org/10.1007/s003380050249

[62] I. G. Macintyre, "Demise, Regeneration, and Survival of Some Western Atlantic Reefs During the Holocene Transgression," in *Geological Approaches to Coral Reef Ecology*, R. B. Aronson, Ed. New York, NY: Springer, 2007, pp. 181–200. [Online]. Available: https://doi.org/10.1007/978-0-387-33537-7_7

[63] J. M. Guinotte and V. J. Fabry, "Ocean acidification and its potential effects on marine ecosystems," *Annals of the New York Academy of Sciences*, vol. 1134, no. 1, pp. 320–342, 2008, publisher: Citeseer.

[64] J. S. Madin and S. R. Connolly, "Ecological consequences of major hydrodynamic disturbances on coral reefs," *Nature*, vol. 444, no. 7118, pp. 477–480, Nov. 2006, number: 7118 Publisher: Nature Publishing Group. [Online]. Available: https://www.nature.com/articles/nature05328

[65] L. Burke *et al.*, "Reefs at risk," *World Resources Institute (WRI), Washington, DC*, vol. 124, 2011.

[66] Z. H. Forsman *et al.*, "Coral farming: effects of light, water motion and artificial foods," *Journal of the Marine Biological Association of the United Kingdom*, vol. 92, no. 4, pp. 721–729, Jun. 2012. [Online]. Available: https://doi.org/10.1017/S0025315411001500

[67] M. Païdoussis, S. Price, and E. de Langre, *Fluid-Structure Interactions: Cross-Flow-Induced Instabilities*. Cambridge University Press, 2010.

[68] J. Fredsøe and M. B. Sumer, *Hydrodynamics Around Cylindrical Structures (Revised Edition)*. World Scientific, Sep. 2006.

[69] W. J. Pierson and L. Moskowitz, "A proposed spectral form for fully developed wind seas based on the similarity theory of S. A. Kitaigorodskii," *Journal of Geophysical Research (1896-1977)*, vol. 69, no. 24, pp. 5181–5190, 1964. [Online]. Available: https://agupubs.onlinelibrary.wiley.com/doi/abs/10.1029/JZ069i024p05181

[70] K. Hasselmann *et al.*, "Measurements of wind-wave growth and swell decay during the Joint North Sea Wave Project (JONSWAP)," *Ergänzungsheft 8-12*, 1973, publisher: Deutches Hydrographisches Institut. [Online]. Available: https://repository.tudelft.nl/islandora/object/uuid%3Af204e188-13b9-49d8-a6dc-4fb7c20562fc

[71] B. Esquivel-Trava, F. J. Ocampo-Torres, and P. Osuna, "Spatial structure of directional wave spectra in hurricanes," *Ocean Dynamics*, vol. 65, no. 1, pp. 65–76, Jan. 2015. [Online]. Available: https://doi.org/10.1007/s10236-014-0791-9

[72] F. J. Huera-Huarte and M. Gharib, "Flow-induced vibrations of a side-by-side arrangement of two flexible circular cylinders," *Journal of Fluids and Structures*, vol. 27, no. 3, pp. 354–366, Apr. 2011. [Online]. Available: http://www.sciencedirect.com/science/article/pii/S0889974611000041

[73] C. H. K. Williamson, "Vortex Dynamics in the Cylinder Wake," *Annual Review of Fluid Mechanics*, vol. 28, no. 1, pp. 477–539, 1996. [Online]. Available: https://doi.org/10.1146/annurev.fl.28.010196.002401

[74] S. Étienne and D. Pelletier, "The low Reynolds number limit of vortex-induced vibrations," *Journal of Fluids and Structures*, vol. 31, pp. 18–29, May 2012. [Online]. Available: http://www.sciencedirect.com/science/article/pii/S0889974612000485

[75] C. H. K. Williamson, "Three-dimensional wake transition," *Journal of Fluid Mechanics*, vol. 328, pp. 345–407, Dec. 1996. [Online]. Available: https://doi.org/10.1017/S0022112096008750

[76] R. E. D. Bishop and A. Y. Hassan, "The lift and drag forces on a circular cylinder oscillating in a flowing fluid," *Proc. R. Soc. Lond. A*, vol. 277, no. 1368, pp. 51–75, Jan. 1964. [Online]. Available: http://rspa.royalsocietypublishing.org/content/277/1368/51

[77] C. C. Feng, "The measurement of vortex induced effects in flow past stationary and oscillating circular and D-section cylinders," Ph.D. dissertation, University of British Columbia, 1968. [Online]. Available: https://open.library.ubc.ca/cIRcle/collections/ubctheses/831/items/1.0104049

[78] A. Khalak and C. H. K. Williamson, "Motions, Forces and Mode Transitions in Vortex-Induced Vibrations at Low Mass-Damping," *Journal of Fluids and Structures*, vol. 13, no. 7, pp. 813–851, Oct. 1999. [Online]. Available: http://www.sciencedirect.com/science/article/pii/S0889974699902360

[79] J. H. Lienhard, *Synopsis of lift, drag, and vortex frequency data for rigid circular cylinders*. Technical Extension Service, Washington State University Pullman, WA, 1966, vol. 300.

[80] J. R. Chaplin *et al.*, "Laboratory measurements of vortex-induced vibrations of a vertical tension riser in a stepped current," *Journal of Fluids and Structures*, vol. 21, no. 1, pp. 3–24, Nov. 2005. [Online]. Available: http://www.sciencedirect.com/science/article/pii/S0889974605001465

[81] D. J. Newman and G. E. Karniadakis, "A direct numerical simulation study of flow past a freely vibrating cable," *Journal of Fluid Mechanics*, vol. 344, pp. 95–136, 1997.

[82] C. Evangelinos and G. E. Karniadakis, "Dynamics and flow structures in the turbulent wake of rigid and flexible cylinders subject to vortex-induced vibrations," *Journal of Fluid Mechanics*, vol. 400, pp. 91–124, Dec. 1999, publisher: Cambridge University Press. [Online]. Available: https://doi.org/10.1017/S0022112099006606

[83] D. Lucor, H. Mukundan, and M. S. Triantafyllou, "Riser modal identification in CFD and full-scale experiments," *Journal of Fluids and Structures*, vol. 22, no. 6,

pp. 905–917, Aug. 2006. [Online]. Available: http://www.sciencedirect.com/science/article/pii/S0889974606000569

[84] A. L. C. Fujarra *et al.*, "Vortex-Induced Vibration of a Flexible Cantilever," *Journal of Fluids and Structures*, vol. 15, no. 3, pp. 651–658, Apr. 2001. [Online]. Available: http://www.sciencedirect.com/science/article/pii/S0889974600903682

[85] T. Leclercq and E. de Langre, "Vortex-induced vibrations of cylinders bent by the flow," *Journal of Fluids and Structures*, vol. 80, pp. 77–93, Jul. 2018. [Online]. Available: http://www.sciencedirect.com/science/article/pii/S0889974617307764

[86] A. H. Nayfeh, F. Owis, and M. R. Hajj, "A Model for the Coupled Lift and Drag on a Circular Cylinder." American Society of Mechanical Engineers Digital Collection, 2003, pp. 1289–1296. [Online]. Available: https://asmedigitalcollection.asme.org/IDETC-CIE/proceedings/IDETC-CIE2003/37033/1289/358964

[87] A. H. Nayfeh and D. T. Mook, *Nonlinear oscillations*. John Wiley & Sons, 1995.

[88] R. T. Hartlen and I. G. Currie, "Lift-Oscillator Model of Vortex-Induced Vibration," *Journal of the Engineering Mechanics Division*, vol. 96, no. 5, pp. 577–591, 1970, publisher: ASCE. [Online]. Available: https://cedb.asce.org/CEDBsearch/record.jsp?dockey=0016651

[89] M. L. Facchinetti, E. de Langre, and F. Biolley, "Coupling of structure and wake oscillators in vortex-induced vibrations," *Journal of Fluids and Structures*, vol. 19, no. 2, pp. 123–140, Feb. 2004. [Online]. Available: http://www.sciencedirect.com/science/article/pii/S0889974603001853

[90] L. Mathelin and E. de Langre, "Vortex-induced vibrations and waves under shear flow with a wake oscillator model," *European Journal of Mechanics-B/Fluids*, vol. 24, no. 4, pp. 478–490, 2005, publisher: Elsevier Masson.

[91] R. Violette, E. de Langre, and J. Szydlowski, "Computation of vortex-induced vibrations of long structures using a wake oscillator model: Comparison with DNS and experiments," *Computers & Structures*, vol. 85, no. 11, pp. 1134–1141, Jun. 2007. [Online]. Available: http://www.sciencedirect.com/science/article/pii/S004579490600229X

[92] G. Birkhoff, "Formation of Vortex Streets," *Journal of Applied Physics*, vol. 24, no. 1, pp. 98–103, Jan. 1953. [Online]. Available: https://aip.scitation.org/doi/abs/10.1063/1.1721143

[93] A.-M. E. Allison, "Analytical investigation of a semi-empirical flow-induced vibration model," Ph.D., The University of Western Ontario (Canada), Canada, 1998. [Online]. Available: https://search.proquest.com/docview/304504227/abstract/85711AB28C34476FPQ/1

[94] Y. Nakamura, "Vortex excitation of a circular cylinder treated as a binary flutter," *Kyushu University, Research Institute for Applied Mechanics, Reports*, vol. 17, no. 59, pp. 217–234, 1969.

[95] O. Ahmad, "Nonlinear structural response in vortex -induced vibrations," Ph.D., Stevens Institute of Technology, United States – New Jersey, 2004. [Online]. Available: https://search.proquest.com/docview/305090475/abstract/42658C085B5849E8PQ/1

[96] G. Parkinson, "Phenomena and modelling of flow-induced vibrations of bluff bodies," *Progress in Aerospace Sciences*, vol. 26, no. 2, pp. 169–224, Jan. 1989. [Online]. Available: http://www.sciencedirect.com/science/article/pii/0376042189900080

[97] Y. Tamura and K. Shimada, "A mathematical model for the transverse oscillations of square cylinders," in *Proc. of International Conference on Flow Induced Vibrations, Bowness-Windermere, England*, 1987, pp. 12–14.

[98] Y. Tamura and A. Amano, "Mathematical model for vortex-induced oscillations of continuous systems with circular cross section," *Journal of Wind Engineering and Industrial Aerodynamics*, vol. 14, no. 1, pp. 431–442, Dec. 1983. [Online]. Available: http://www.sciencedirect.com/science/article/pii/0167610583900442

[99] W. Hanke *et al.*, "Harbor seal vibrissa morphology suppresses vortex-induced vibrations," *Journal of Experimental Biology*, vol. 213, no. 15, pp. 2665–2672, Jul. 2010. [Online]. Available: http://jeb.biologists.org/content/213/15/2665.abstract

[100] D. I. Rubenstein and M. Koehl, "The mechanisms of filter feeding: some theoretical considerations," *American Naturalist*, pp. 981–994, 1977.

[101] M. R. Palmer *et al.*, "Observations of particle capture on a cylindrical collector: Implications for particle accumulation and removal in aquatic systems," *Limnology and Oceanography*, vol. 49, no. 1, pp. 76–85, Jan. 2004. [Online]. Available: https://aslopubs.onlinelibrary.wiley.com/doi/abs/10.4319/lo.2004.49.1.0076

[102] "The Pencil Code." [Online]. Available: http://pencil-code.nordita.org/

[103] R. Clift, J. R. Grace, and M. E. Weber, "Bubbles, drops, and particles–Academic Press," *New York*, vol. 510, p. 147, 1978.

[104] "OpenFOAM | The OpenFOAM Foundation." [Online]. Available: https://openfoam.org/

[105] L. A. Skinner, "Generalized expansions for slow flow past a cylinder," *The Quarterly Journal of Mechanics and Applied Mathematics*, vol. 28, no. 3, pp. 333–340, 1975, publisher: Oxford University Press.

[106] S. Kaplun, "Low Reynolds number flow past a circular cylinder," *Journal of Mathematics and Mechanics*, pp. 595–603, 1957, publisher: JSTOR.

[107] M. Van Dyke, *Perturbation Methods in Fluid Mechanics*. Stanford, California: The Parabolic Press, 1975.

[108] D. McCombe and J. D. Ackerman, "Collector Motion Affects Particle Capture in Physical Models and in Wind Pollination," *The American Naturalist*, vol. 192, no. 1, pp. 81–93, Jul. 2018. [Online]. Available: https://www.journals.uchicago.edu/doi/10.1086/697551

[109] J. Krick and J. D. Ackerman, "Adding ecology to particle capture models: Numerical simulations of capture on a moving cylinder in crossflow," *Journal of Theoretical Biology*, vol. 368, pp. 13–26, Mar. 2015. [Online]. Available: http://www.sciencedirect.com/science/article/pii/S0022519314006924

[110] "ANSYS, ANSYS-CFX-Solver Theory Guide. Release 13.0."

[111] H. R. Lasker, "A comparison of the particulate feeding abilities of three species of gorgonian soft coral," *Mar Ecol Prog Ser*, vol. 5, no. 6, pp. 61–67, 1981.

[112] M. LaBarbera, "Feeding Currents and Particle Capture Mechanisms in Suspension Feeding Animals," *American Zoologist*, vol. 24, no. 1, pp. 71–84, Feb. 1984. [Online]. Available: http://az.oxfordjournals.org/content/24/1/71.abstract

[113] M. R. Patterson, "The Effects of Flow on Polyp-Level Prey Capture in an Octocoral, Alcyonium siderium," *The Biological Bulletin*, vol. 180, no. 1, pp. 93–102, Feb. 1991. [Online]. Available: https://www.journals.uchicago.edu/doi/abs/10.2307/1542432

[114] S. Étienne, A. Garon, and D. Pelletier, "Perspective on the geometric conservation law and finite element methods for ALE simulations of incompressible flow," *Journal of*

Computational Physics, vol. 228, no. 7, pp. 2313–2333, Apr. 2009. [Online]. Available: http://www.sciencedirect.com/science/article/pii/S0021999108006165

[115] M. Boudina, "PARADVECT (PARticle ADVECTion): a Python code to simulate the trajectory of particles advected by a fluid flow," Jun. 2020. [Online]. Available: https://doi.org/10.5281/zenodo.3981610

[116] P. A. Sackinger, P. R. Schunk, and R. R. Rao, "A Newton–Raphson Pseudo-Solid Domain Mapping Technique for Free and Moving Boundary Problems: A Finite Element Implementation," *Journal of Computational Physics*, vol. 125, no. 1, pp. 83–103, Apr. 1996. [Online]. Available: http://www.sciencedirect.com/science/article/pii/S0021999196900819

[117] A. Hay *et al.*, "hp-Adaptive time integration based on the BDF for viscous flows," *Journal of Computational Physics*, vol. 291, pp. 151–176, Jun. 2015. [Online]. Available: http://www.sciencedirect.com/science/article/pii/S0021999115001692

[118] H. Persillon and M. Braza, "Physical analysis of the transition to turbulence in the wake of a circular cylinder by three-dimensional Navier–Stokes simulation," *Journal of Fluid Mechanics*, vol. 365, pp. 23–88, Jun. 1998. [Online]. Available: https://doi.org/10.1017/S0022112098001116

[119] C. Taylor and P. Hood, "A numerical solution of the Navier-Stokes equations using the finite element technique," *Computers & Fluids*, vol. 1, no. 1, pp. 73–100, Jan. 1973. [Online]. Available: http://www.sciencedirect.com/science/article/pii/0045793073900273

[120] J. Schindelin *et al.*, "Fiji: an open-source platform for biological-image analysis," *Nature Methods*, vol. 9, no. 7, pp. 676–682, Jul. 2012. [Online]. Available: https://www.nature.com/articles/nmeth.2019

[121] S. D. Cairns, "A checklist of the ahermatypic Scleractinia of the Gulf of Mexico, with the description of a new species," *Gulf and Caribbean Research*, vol. 6, no. 1, pp. 9–15, 1977.

[122] N. D. B. Center, "National Data Buoy Center." [Online]. Available: https://www.ndbc.noaa.gov/

[123] Y. Nakamura, K. Hirata, and K. Kashima, "Galloping of a Circular Cylinder in the Presence of a Splitter Plate," *Journal of Fluids and Structures*, vol. 8, no. 4,

pp. 355–365, May 1994. [Online]. Available: http://www.sciencedirect.com/science/article/pii/S0889974684710176

[124] H. Glauert, "The rotation of an airfoil about a fixed axis. R. & m. No. 595," *British ACA*, 1919.

[125] J. P. den Hartog, "Transmission Line Vibration Due to Sleet," *Transactions of the American Institute of Electrical Engineers*, vol. 51, no. 4, pp. 1074–1076, Dec. 1932, conference Name: Transactions of the American Institute of Electrical Engineers.

[126] C. E. Brennen, "A Review of Added Mass and Fluid Inertial Forces." Naval Civil Engineering Laboratory, Port Hueneme, California, Tech. Rep., Jan. 1982. [Online]. Available: https://apps.dtic.mil/docs/citations/ADA110190

[127] R. Löhner and J. Ambrosiano, "A vectorized particle tracer for unstructured grids," *Journal of Computational Physics*, vol. 91, no. 1, pp. 22–31, Nov. 1990. [Online]. Available: http://www.sciencedirect.com/science/article/pii/002199919090002I

[128] R. Löhner, *Applied Computational Fluid Dynamics Techniques: An Introduction Based on Finite Element Methods*. John Wiley & Sons, Apr. 2008.

[129] E. Buckingham, "On Physically Similar Systems; Illustrations of the Use of Dimensional Equations," *Physical Review*, vol. 4, no. 4, pp. 345–376, Oct. 1914, publisher: American Physical Society. [Online]. Available: https://link.aps.org/doi/10.1103/PhysRev.4.345

[130] H. Schlichting (Deceased) and K. Gersten, *Boundary-Layer Theory*, 9th ed. Berlin Heidelberg: Springer-Verlag, 2017. [Online]. Available: https://www.springer.com/gp/book/9783662529171

[131] S. Kaplun, "The role of coordinate systems in boundary layer theory," PhD, California Institute of Technology, 1954. [Online]. Available: https://resolver.caltech.edu/CaltechETD:etd-12032003-111930

[132] L. M. Milne-Thomson, *Theoretical hydrodynamics*. Macmillan & Co., 1962.

[133] M. Alnæs *et al.*, "The FEniCS Project Version 1.5," *Archive of Numerical Software*, vol. 3, no. 100, Dec. 2015, number: 100. [Online]. Available: https://journals.ub.uni-heidelberg.de/index.php/ans/article/view/20553

[134] L. D. Landau and E. M. Lifshitz, *Theory of Elasticity*. Pergamon Press, Jan. 1970.

[135] B. Audoly and Y. Pomeau, *Elasticity and Geometry: From hair curls to the nonlinear response of shells*. Oxford ; New York: Oxford University Press, Aug. 2010.

[136] G. I. Taylor, "Analysis of the swimming of long and narrow animals," *Proceedings of the Royal Society of London. Series A. Mathematical and Physical Sciences*, vol. 214, no. 1117, pp. 158–183, Aug. 1952, publisher: Royal Society. [Online]. Available: https://royalsocietypublishing.org/doi/abs/10.1098/rspa.1952.0159

[137] E. de Langre, *Fluides et solides*. Editions Ecole Polytechnique, 2001.

[138] F. Candelier, F. Boyer, and A. Leroyer, "Three-dimensional extension of Lighthill's large-amplitude elongated-body theory of fish locomotion," *Journal of Fluid Mechanics*, vol. 674, pp. 196–226, May 2011, publisher: Cambridge University Press. [Online]. Available: https://doi.org/10.1017/S002211201000649X

[139] W. L. Oberkampf and C. J. Roy, *Verification and Validation in Scientific Computing*. Cambridge University Press, Oct. 2010.

[140] F. Rohde, "Large deflections of a cantilever beam with uniformly distributed load," *Quarterly of Applied Mathematics*, vol. 11, no. 3, pp. 337–338, 1952.

[141] A. Espinosa-Gayosso *et al.*, "Density-ratio effects on the capture of suspended particles in aquatic systems," *Journal of Fluid Mechanics*, vol. 783, pp. 191–210, Nov. 2015. [Online]. Available: https://doi.org/10.1017/jfm.2015.557

[142] C. Béguin, E. Pelletier, and S. Étienne, "Void fraction influence on added mass in a bubbly flow," *European Journal of Mechanics - B/Fluids*, vol. 56, pp. 28–45, Mar. 2016. [Online]. Available: https://linkinghub.elsevier.com/retrieve/pii/S0997754615001272

[143] E. Lecarpentier *et al.*, "Computational Fluid Dynamic Simulations of Maternal Circulation: Wall Shear Stress in the Human Placenta and Its Biological Implications," *PLoS ONE*, vol. 11, no. 1, Jan. 2016. [Online]. Available: https://www.ncbi.nlm.nih.gov/pmc/articles/PMC4729471/

[144] X. Tang and D. Staack, "Bioinspired mechanical device generates plasma in water via cavitation," *Science Advances*, vol. 5, no. 3, p. eaau7765, Mar. 2019, publisher: American Association for the Advancement of Science Section: Research Article. [Online]. Available: https://advances.sciencemag.org/content/5/3/eaau7765

[145] M. Boudina, "RodiCS," Jul. 2020. [Online]. Available: https://github.com/lm2-poly/RodiCS

[146] J. Bleyer, "Numerical Tours of Computational Mechanics with FEniCS," 2018, publisher: Zenodo.

APPENDIX A NEIGHBOUR-TO-NEIGHBOUR ALGORITHM

In this appendix we present the neighbour-to-neighbour algorithm for interpolation in unstructured grids [127,128]. It is the most suitable interpolation, easy-to-implement technique for *particle-in-cell* codes, such ours, in which physical particles do not jump over many elements in a single time step. Instead of dividing the entire domain into bins or tree structures, the neighbour-to-neighbour algorithm searches the new element starting from the vicinity of the prior known one.

Let P_n and P_{n+1} be the particle positions at time steps n and $n+1$ as shown in Figure A.1. We first feed the algorithm with an initial guess, which we always choose to be the host element of P_n, denoted E_n (expect for the first time step $n = 0$ where a loop over the entire domain finds the host element of the initial position P_0 of the particle). Then, if P_{n+1} is in E_n, there is no need to continue and E_{n+1} is exactly E_n. If not, we look at the edge s_n^- from which the particle has left E_n. The next most probable guess we choose is the element E'_n that shares the edge s_n^- with E_n. We verify again if P_{n+1} is in E'_n, and repeat this recursive process until we find the new host element. Algorithm A.1 summarises the neighbour-to-neighbour algorithm as we implemented it in PYTHON.

Now, how do we check if a point P is in a certain element E? As schematised in Figure A.2, we simply calculate the shape functions of the element E at P, denoted N_1, N_2, and N_3. If $0 \leq N_1, N_2, N_3 \leq 1$, then $P \in E$. Otherwise, $P \notin E$ and there is at least one negative shape function since $N_1 + N_2 + N_3 = 1$. In this case, s^- is the edge of E facing the node with the most negative shape function.

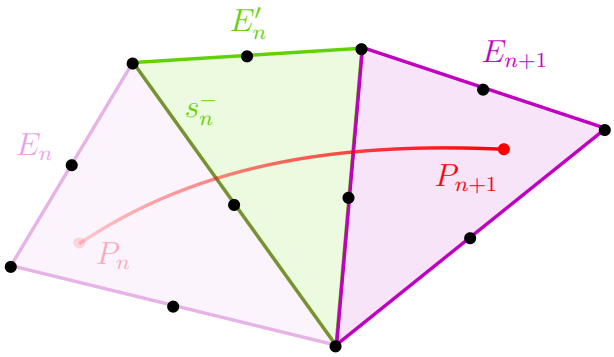

Figure A.1 Schematics of a particle crossing an element between two time steps

Algorithm A.1 Neighbour-to-neighbour algorithm, at time step $n > 0$

Initial guess: $E^* \leftarrow E_n$, with E_n being the host element of P_n

while $P_{n+1} \notin E^*$ **do**
  Find the element E'_n that shares s_n^- with E^*
  $E^* \leftarrow E'_n$
end while

$E_{n+1} \leftarrow E^*$.

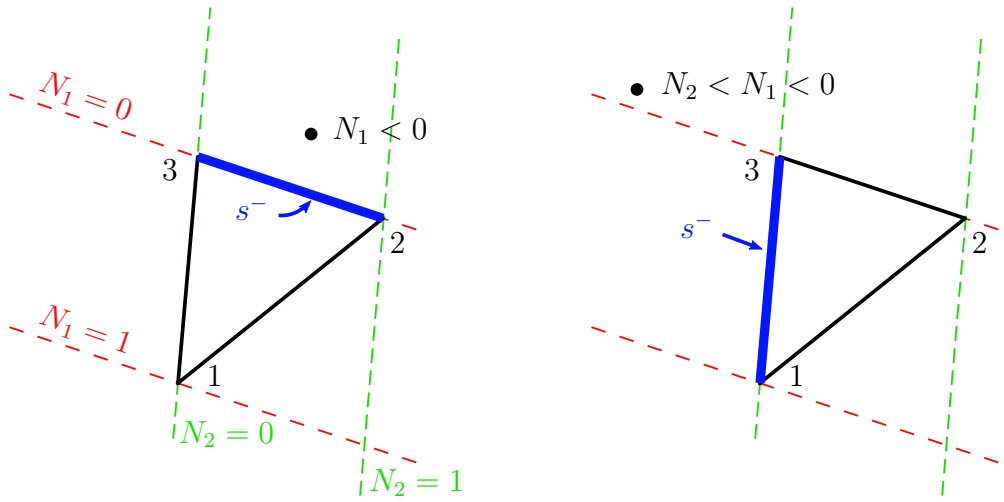

(a) (b)

Figure A.2 Examples highlighting the edge s^- of an element E regarding the position of the point P (●). In the case (a), only the shape function N_1 is negative, hence s^- is the edge $2-3$. In the case (b), both N_1 and N_2 are negative, but N_2 has the smallest values, hence s^- is the edge $1-3$.

APPENDIX B SOLID CONTACT CRITERION

In this project, the body intercepting spherical particles was always a circular cylinder. The criterion of solid contact in this case is straightforward: if d_p and D are respectively the particle and the cylinder diameters, and $\boldsymbol{x}_\mathrm{p}$ and $\boldsymbol{X}_\mathrm{cyl}$ the position of their centres, then the contact occurs when $||\boldsymbol{x}_\mathrm{p} - \boldsymbol{X}_\mathrm{cyl}|| \leq (d_\mathrm{p} + D)/2$. For a general shape, however, the above method is not viable anymore. This appendix presents a geometrical method to detect the solid contact of a particle with a body of any shape.

Let us consider a closed, simply connected geometry ($\mathscr{G}$) with edges oriented counter-clockwise, as illustrated in Figure B.1(a). A particle with a non-zero size touches ($\mathscr{G}$) once its centre enters the shaded region ($\mathscr{S}$) with rounded corners. This region is the extension of ($\mathscr{G}$): edges are translated away with the distance $d_\mathrm{p}/2$ in the direction of their outward normal, and connected with arcs of circle, whose centres are the vertices and having the same radius $d_\mathrm{p}/2$. The blue particle in Figure B.1(a) is an example of a captured particle that have a centre inside ($\mathscr{S}$).

Now let P_i be the vertices of ($\mathscr{G}$), and P the particle centre. We begin by calculating the projection h_i of P on each edge P_iP_{i+1}

$$h_i = \boldsymbol{P}_i\boldsymbol{P} \cdot \boldsymbol{n}_i, \tag{B.1}$$

with

$$\boldsymbol{n}_i = \frac{\boldsymbol{P}_i\boldsymbol{P}_{i+1}}{||\boldsymbol{P}_i\boldsymbol{P}_{i+1}||} \times \boldsymbol{e}_z. \tag{B.2}$$

Here h_i is algebraic, i.e. can be either positive or negative. A necessary condition for a solid contact is then

$$h_i \leq d_\mathrm{p}/2 \quad \text{for all vertices } P_i. \tag{B.3}$$

The red particle in Figure B.1(a) verifies this condition, but it is not captured because it stands in a region, near the corner P_4, that is not included in ($\mathscr{S}$). In other words, the condition (B.3) is only necessary since it does not exclude the sharp corners of the extended geometry (this case is more apparent for bodies with sharp angles, like the vertex P_2 in Figure B.1(a)). One way to circumvent these regions is to consider each vertex P_i, and take the normals of the two edges to which it belongs, namely $\boldsymbol{n}_{i-1}$ and $\boldsymbol{n}_i$. If P lays within the surface defined between $\boldsymbol{n}_{i-1}$ and $\boldsymbol{n}_i$, then it is close to the vertex P_i and we should check its type as sketched in Figure B.1(b). If it is convex, there is no need to round the corner

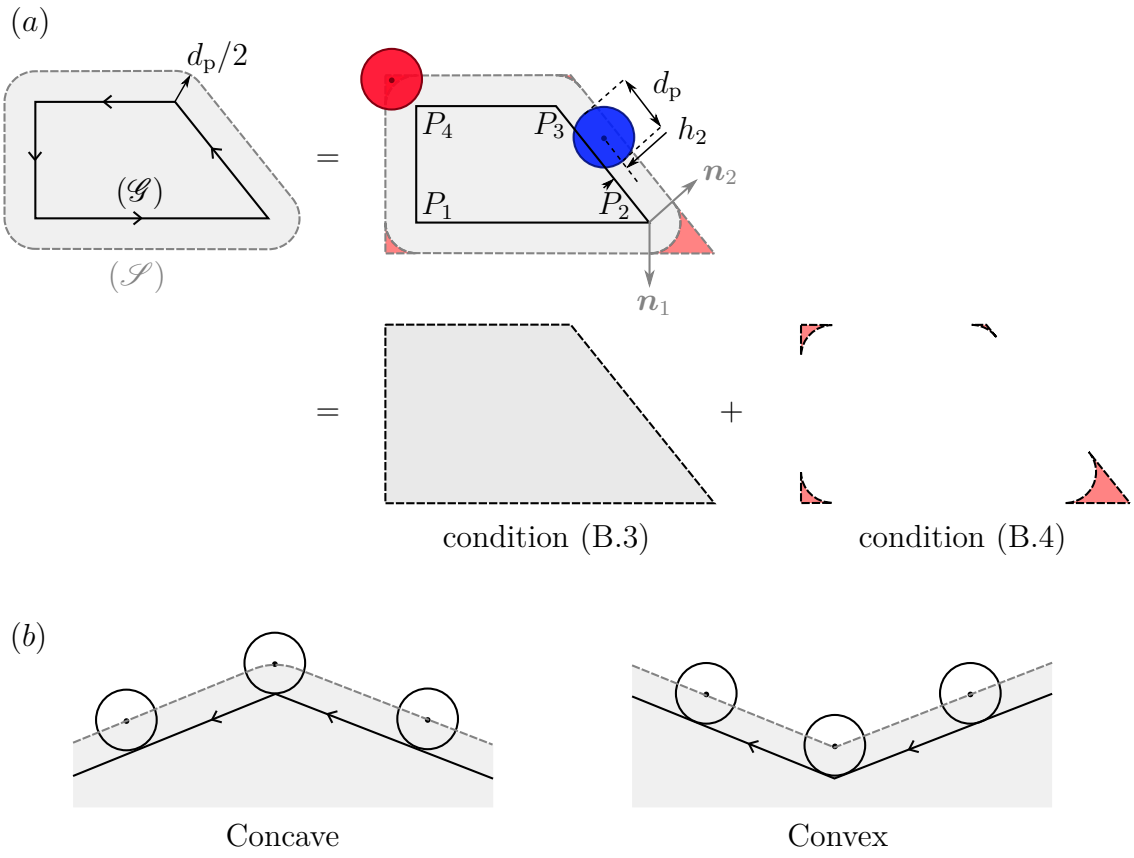

Figure B.1 (a) Schematics of the solid contact criterion for a right trapezoid ($\mathscr{G}$). All vertices are concave. The shaded area with rounded corners ($\mathscr{S}$) is the indicator of the solid contact (dashed line). It is obtained by translating each edge of the trapezoid with the distance $d_p/2$ outwards, and connecting them with arcs of circle. Notice that the centre of the red particle is still outside ($\mathscr{S}$), even though it verifies the condition (B.3), hence no contact is detected. Conversely, the centre of blue particle has entered ($\mathscr{S}$), thus the solid contact occurs. (b) The boundary of the shaded area is rounded at the concave vertex, and sharp at the convex one.

and condition (B.3) is also sufficient. If it is concave, then P is inside the rounded corner if it stands at a distance less or equal than $d_\mathrm{p}/2$ from P_i. We can merge these statements into the following condition

$$\begin{aligned} &\text{If, for a certain vertex } P_i, \quad (\boldsymbol{n}_{i-1} \times \boldsymbol{P}_i\boldsymbol{P}) \cdot \boldsymbol{e}_z > 0 \text{ and } (\boldsymbol{P}_i\boldsymbol{P} \times \boldsymbol{n}_i) \cdot \boldsymbol{e}_z > 0, \\ &\text{then} \quad ||\boldsymbol{P}_i\boldsymbol{P}|| \leq d_\mathrm{p}/2. \end{aligned} \tag{B.4}$$

The clause $(\boldsymbol{n}_{i-1} \times \boldsymbol{n}_i) \cdot \boldsymbol{e}_z > 0$ means that we go through concave vertices only.

To recapitulate, we have

$$\text{solid contact} \iff P \in (\mathscr{S}) \iff \begin{cases} \text{condition (B.3)}, \\ \text{condition (B.4)}. \end{cases} \tag{B.5}$$

Finally, worth to notice that for a punctual particle, $(\mathscr{S})$ shrinks into $(\mathscr{G})$ and the vicinity of the vertices vanishes, thereby the solid contact criterion reduces to the condition (B.3) with $d_\mathrm{p} = 0$.

Here is the solid contact detection algorithm as we implemented it in PYTHON (the single loop in our code is divided in two parts here for the sake of clarity):

Algorithm B.1 Solid contact criterion for a body of general shape

for P_iP_{i+1} in edges **do**
  $\boldsymbol{t}_i \leftarrow \boldsymbol{P}_i\boldsymbol{P}_{i+1} / \left|\left|\boldsymbol{P}_i\boldsymbol{P}_{i+1}\right|\right|$
  $\boldsymbol{n}_i \leftarrow \boldsymbol{t}_i \times \boldsymbol{e}_z$
  $h_i \leftarrow \boldsymbol{P}_i\boldsymbol{P} \cdot \boldsymbol{n}_i$

  if $h_i > d_\mathrm{p}/2$ **then**
    return particle is outside ($\mathscr{S}$)
  end if

end for
 # Condition (B.3) *is fulfilled.*

for P_i in vertices **do**
  if $(\boldsymbol{n}_{i-1} \times \boldsymbol{P}_i\boldsymbol{P}) \cdot \boldsymbol{e}_z > 0$ and $(\boldsymbol{P}_i\boldsymbol{P} \times \boldsymbol{n}_i) \cdot \boldsymbol{e}_z > 0$ **then**
    # P is within two normals
    if $\left|\left|\boldsymbol{P}_i\boldsymbol{P}\right|\right| \leq d_\mathrm{p}/2$ **then**
      # Condition (B.4) *is fulfilled.*
      return particle is inside ($\mathscr{S}$)
    else
      return particle is outside ($\mathscr{S}$)
    end if

  end if
end for
 # There is no vertex P_i that fulfills the first clause of the condition (B.4)*. Condition* (B.3) *alone is hence sufficient.*

return particle is inside ($\mathscr{S}$)

APPENDIX C ALTERNATIVE TRAJECTORY CALCULATION

In this appendix we provide an alternative method to compute the trajectories of particles. We thought about this approach when we found that the particle-based Reynolds number Re_p for a particle with a diameter ratio $R = 0.031$ was always less than 6×10^{-2} (see Figure 4.6). We assume, throughout the ensuing derivation, that we solve trajectories of particles keeping Re_p so small, during the whole simulation, that we can simplify the factor $1+Re_\mathrm{p}^{0.687} \approx 1$ in the expression of the drag in equation (4.10). The governing equations of particle advection (4.9) become

$$\frac{\mathrm{d}\bar{\boldsymbol{x}}_\mathrm{p}}{\mathrm{d}\bar{t}} = \bar{\boldsymbol{u}}_\mathrm{p}, \tag{C.1a}$$

$$\frac{\mathrm{d}\bar{\boldsymbol{u}}_\mathrm{p}}{\mathrm{d}\bar{t}} = -\frac{18}{\rho^+ R^2 Re}\left(\bar{\boldsymbol{u}}_\mathrm{p} - \bar{\boldsymbol{U}}_\mathrm{f}\right) - \frac{1}{\rho^+}\bar{\boldsymbol{\nabla}}\bar{p} - \frac{C_\mathrm{m}}{\rho^+}\left(\frac{\mathrm{d}\bar{\boldsymbol{u}}_\mathrm{p}}{\mathrm{d}\bar{t}} - \frac{\mathrm{d}\bar{\boldsymbol{U}}_\mathrm{f}}{\mathrm{d}\bar{t}}\right). \tag{C.1b}$$

We will drop out the dimensionless notation $\bar{(.)}$ for the sake of convenience.

The system of equations (C.1) has the form of an ordinary differential equation with a right-hand side forcing term

$$\frac{\mathrm{d}\boldsymbol{x}_\mathrm{p}}{\mathrm{d}t} = \boldsymbol{u}_\mathrm{p}, \tag{C.2a}$$

$$\frac{\mathrm{d}\boldsymbol{u}_\mathrm{p}}{\mathrm{d}t} + \frac{1}{\tau}\boldsymbol{u}_\mathrm{p} = \boldsymbol{F}. \tag{C.2b}$$

Here

$$\tau = \frac{1}{18}(\rho^+ + C_\mathrm{m})R^2 Re \tag{C.3}$$

is the characteristic time, and

$$\boldsymbol{F} = \frac{1}{\tau}\boldsymbol{U}_\mathrm{f} - \frac{1}{\rho^+ + C_\mathrm{m}}\boldsymbol{\nabla}p + \frac{C_\mathrm{m}}{\rho^+ + C_\mathrm{m}}\frac{\mathrm{d}\boldsymbol{U}_\mathrm{f}}{\mathrm{d}t} \tag{C.4}$$

the forcing term, which depends implicitly on time through the particle position

$$\boldsymbol{F}(t) = \boldsymbol{F}(\boldsymbol{x}_\mathrm{p}(t)). \tag{C.5}$$

If we use the combined variable $z = (\boldsymbol{x}_\mathrm{p}, \boldsymbol{u}_\mathrm{p})$, we can rewrite the system of equations (C.2) as

$$\frac{\mathrm{d}z}{\mathrm{d}t} + \mathcal{A}z = f, \tag{C.6}$$

where

$$f = (\mathbf{0}, \boldsymbol{F}), \tag{C.7}$$

and

$$\mathcal{A} = \begin{pmatrix} 0 & -1 \\ 0 & 1/\tau \end{pmatrix}. \tag{C.8}$$

The solution of equation (C.6) is the sum of the homogeneous solution and a particular solution

$$z = z_0 \exp(-t\mathcal{A}) + \int_0^t \exp((s-t)\mathcal{A}) f(s) \mathrm{d}s, \tag{C.9}$$

with $z_0 = (\boldsymbol{x}_{\mathrm{p}0}, \boldsymbol{u}_{\mathrm{p}0})$.

Noticing that

$$\tau\mathcal{A} = (\tau\mathcal{A})^2 = \cdots = (\tau\mathcal{A})^n, \quad n \geq 1, \tag{C.10}$$

we have

$$\exp(-t\mathcal{A}) = \mathcal{I} + (e^{-t/\tau} - 1)\tau\mathcal{A} = \begin{pmatrix} 1 & \tau(1 - e^{-t/\tau}) \\ 0 & e^{-t/\tau} \end{pmatrix}. \tag{C.11}$$

Recall that f is a function of the position of the particle, i.e. $f(s) = f(z(s))$. At a certain time step $t_n = n\Delta t$, we have

$$z_n = z_0 \exp(-t_n\mathcal{A}) + \int_0^{n\Delta t} \exp((s - n\Delta t)) f(z(s)) \mathrm{d}s. \tag{C.12}$$

Then we rewrite the integral as a discrete sum

$$z_n = z_0 \exp(-t_n\mathcal{A}) + \sum_{i=0}^{n-1} \int_{i\Delta t}^{(i+1)\Delta t} \exp((s - n\Delta t)\mathcal{A}) f(z(s)) \mathrm{d}s, n \geq 1. \tag{C.13}$$

Our idea is to approximate each integral on the interval $[i\Delta t, (i+1)\Delta t]$ using the trapezoidal rule

$$\begin{aligned} \int_{i\Delta t}^{(i+1)\Delta t} \exp((s - n\Delta t)\mathcal{A}) f(z(s)) \mathrm{d}s &\approx \Delta t \frac{\exp((i-n)\Delta t\mathcal{A}) f(z_i) + \exp((i-n+1)\Delta t\mathcal{A}) f(z_{i+1})}{2} \\ &\approx \Delta t \frac{\exp(-t_{n-i}\mathcal{A}) f(z_i) + \exp(-t_{n-i-1}\mathcal{A}) f(z_{i+1})}{2}, \end{aligned} \tag{C.14}$$

denoting $t_{n-i} = (n-i)\Delta t$ and $z_i = z(i\Delta t)$.

We insert (C.14) into (C.13) and obtain

$$z_n \approx z_0 \exp(-t_n\mathcal{A}) + \frac{\Delta t}{2}\left[\sum_{i=0}^{n-1}\exp(-t_{n-i}\mathcal{A})f(z_i) + \sum_{i=1}^{n}\exp(-t_{n-i}\mathcal{A})f(z_i)\right] \tag{C.15}$$

Taking apart the first term in the first summation and the last term in the second summation, we get

$$z_n \approx z_0 \exp(-t_n\mathcal{A}) + \Delta t\left[\frac{\exp(-t_n\mathcal{A})f(z_0) + \exp(-t_0\mathcal{A})f(z_n)}{2} + \sum_{i=1}^{n-1}\exp(-t_{n-i}\mathcal{A})f(z_i)\right]. \tag{C.16}$$

Finally, because $t_0 = 0$, the final approximate of z_n is

$$z_n \approx z_0 \exp(-t_n\mathcal{A}) + \Delta t\left[\frac{\exp(-t_n\mathcal{A})f(z_0) + f(z_n)}{2} + \sum_{i=1}^{n-1}\exp(-t_{n-i}\mathcal{A})f(z_i)\right]. \tag{C.17}$$

Now we are at a stage where we have the unknown z_n is both sides. Fortunately, $f(z_n)$ has a null first component $f(z_n) = (\mathbf{0}, \boldsymbol{F}(\boldsymbol{x}_{\mathrm{p}n}))$, and is not multiplied by any matrix in equation (C.17). Therefore, the first component of z_n, namely the particle position $\boldsymbol{x}_{\mathrm{p}n}$, depends only on the history of the trajectory strictly prior to the instant t_n. Using the expression of $\exp(-t\mathcal{A})$ in equation (C.11), we find

$$\boldsymbol{x}_{\mathrm{p}n} \approx \boldsymbol{x}_{\mathrm{p}0} + \tau(1 - e^{-t_n/\tau})\boldsymbol{u}_{\mathrm{p}0} + \Delta t\left[\frac{\tau(1 - e^{-t_n/\tau})}{2}\boldsymbol{F}(\boldsymbol{x}_{\mathrm{p}0}) + \sum_{i=1}^{n-1}\tau(1 - e^{-t_{n-i}/\tau})\boldsymbol{F}(\boldsymbol{x}_{\mathrm{p}i})\right]. \tag{C.18}$$

Having calculated $\boldsymbol{x}_{\mathrm{p}n}$, we insert it in the second component of z_n, namely the particle velocity $\boldsymbol{u}_{\mathrm{p}n}$

$$\boldsymbol{u}_{\mathrm{p}n} \approx e^{-t_n/\tau}\boldsymbol{u}_{\mathrm{p}0} + \Delta t\left[\frac{e^{-t_n/\tau}}{2}\boldsymbol{F}(\boldsymbol{x}_{\mathrm{p}0}) + \frac{1}{2}\boldsymbol{F}(\boldsymbol{x}_{\mathrm{p}n}) + \sum_{i=1}^{n-1}e^{-t_{n-i}/\tau}\boldsymbol{F}(\boldsymbol{x}_{\mathrm{p}i})\right]. \tag{C.19}$$

In the PYTHON code which integrates particle trajectories, explained in chapter 4, the function that lasts the most during a time step is the particle tracer function. Then we gain nothing if we keep equations (C.18) and (C.19) as they are, since we will still need to find the flow solution at each particle position. Yet, these formulae are worth to implement when the user interpolates the flow solution in the whole domain into continuous functions (using cubic interpolation, Lagrange, Tchebytchev polynomials, etc.) In this way, the calculation of the particle trajectory is as simple as a straightforward evaluation of the terms of a sequence.

APPENDIX D CYLINDER RESPONSES

In this appendix, we present the numerical responses of the cylinder obtained from the DNS in CaDyF. These include the responses of the transverse and stream-wise amplitudes $Y_{\max}$ and $X_{\max}$, the slenderness ratio $\gamma = Y_{\max}/X_{\max}$, the distortion coefficient β, and the counter-current distance d_{cc}. After extracting $Y_{\max}$ and $X_{\max}$, β is calculated from equation (6.6), and d_{cc} from equation (6.13). We also plotted the phase diagrams of these parameters in order to see their variation irrespective of the reduced velocity. The last two figures show the vortex shedding frequency response and the Strouhal number against the Reynolds number.

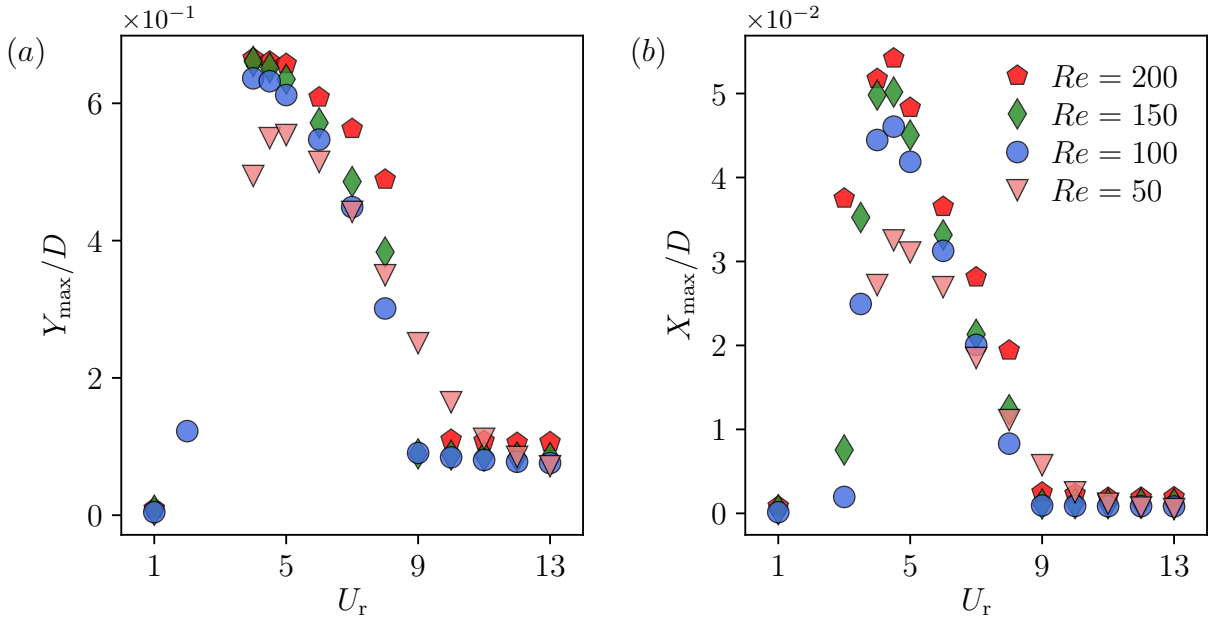

Figure D.1 Response of (a) transverse and (b) stream-wise amplitudes

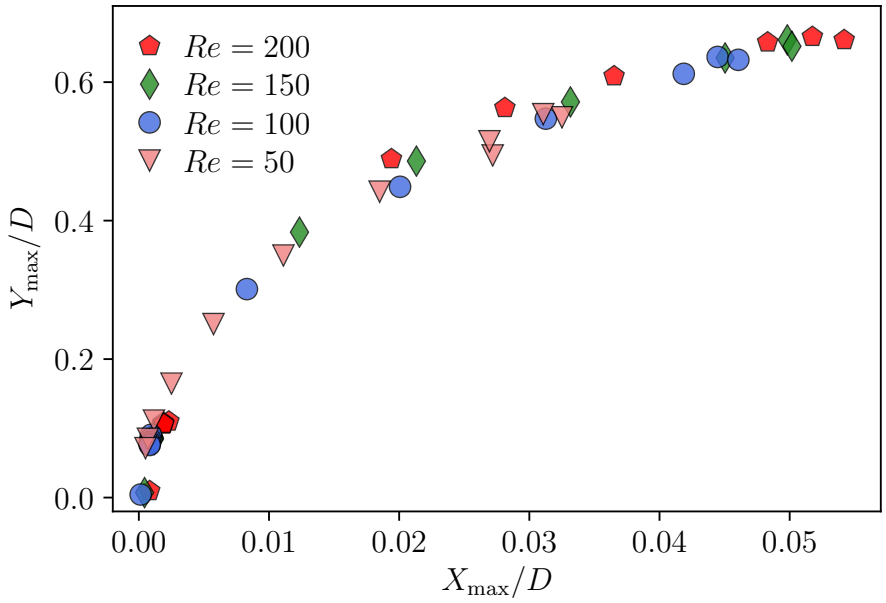

Figure D.2 Transverse amplitude versus stream-wise amplitude

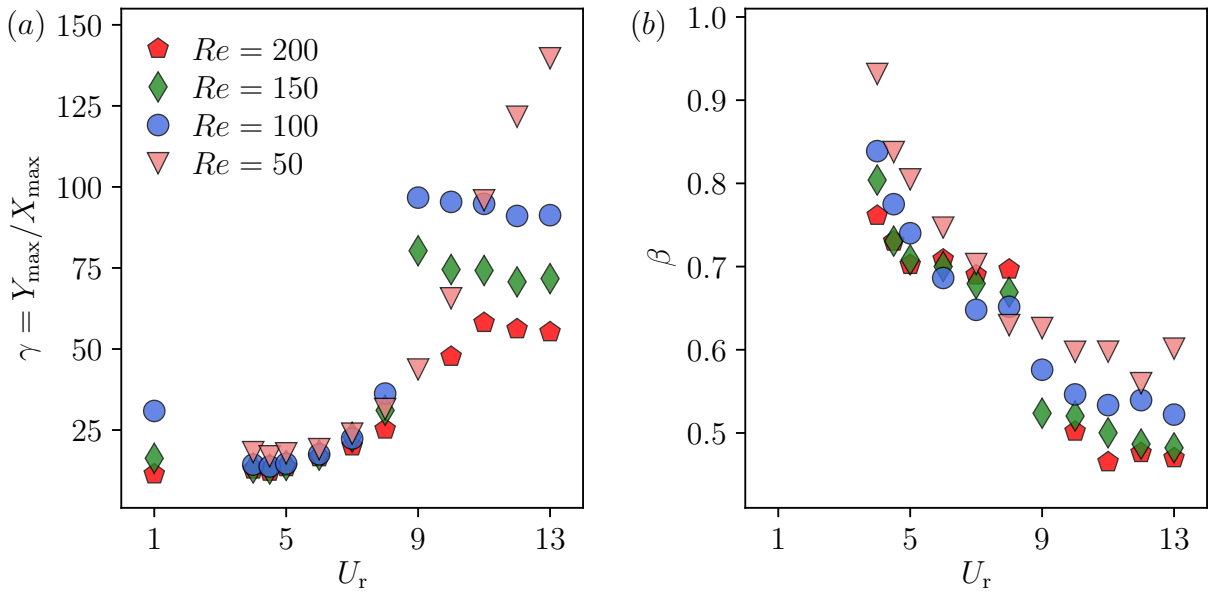

Figure D.3 Response of (a) the slenderness ratio and (b) the distortion coefficient of the lemniscate limit-cycle trajectory. We should mention that we were unable to extract the distortion coefficient for reduced velocities $U_r \leq 3.5$ because the cylinder trajectory did not reach a closed limit cycle.

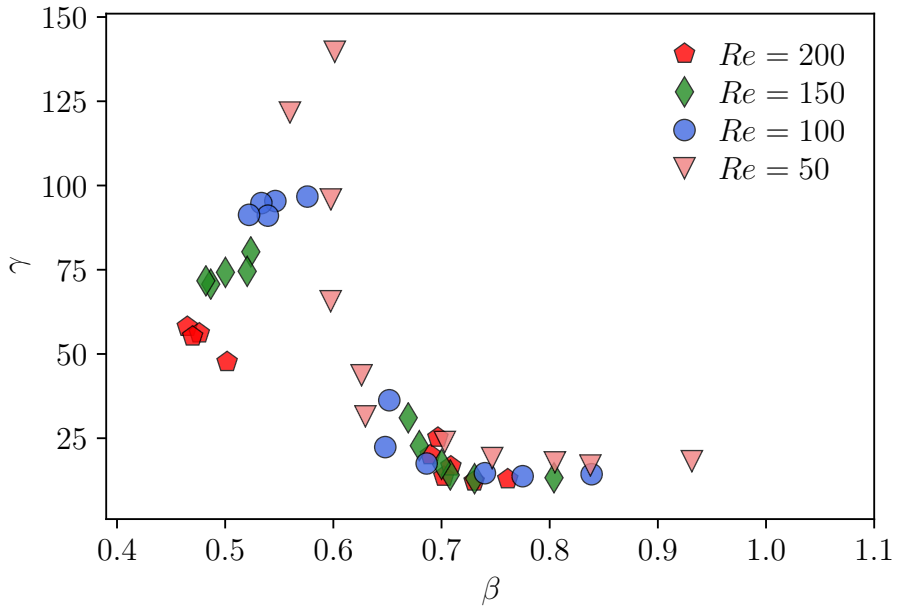

Figure D.4 Slenderness ratio versus distortion coefficient of the lemniscate limit-cycle trajectory.

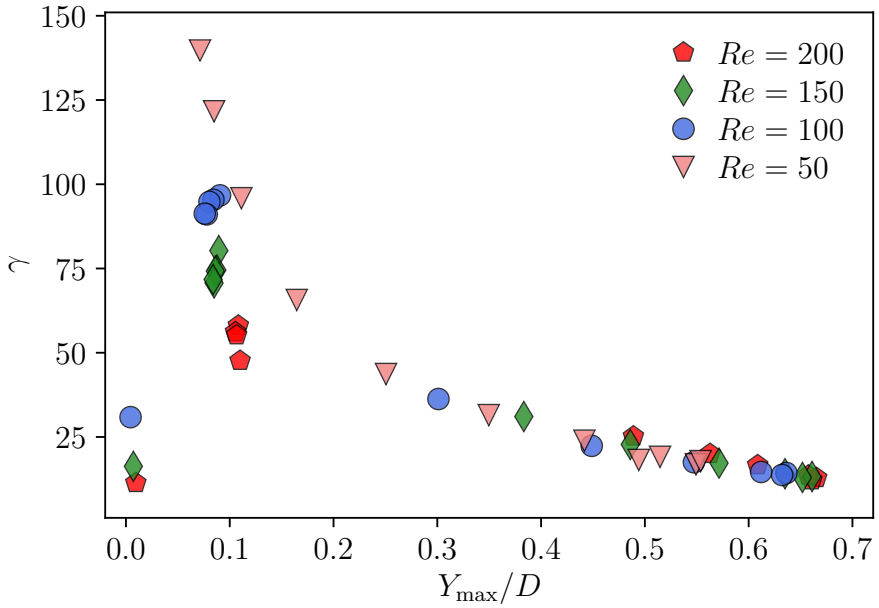

Figure D.5 Slenderness ratio versus transverse amplitude

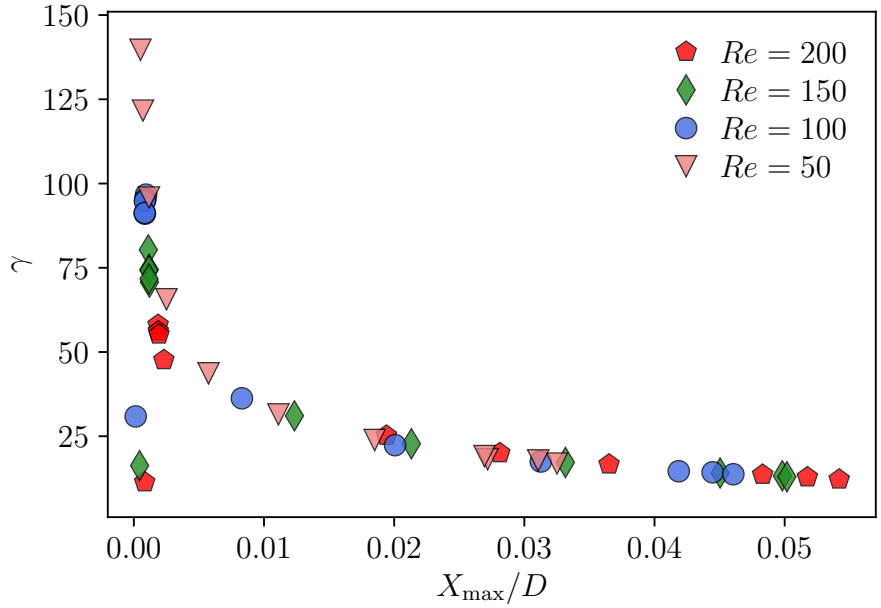

Figure D.6 Slenderness ratio versus stream-wise amplitude

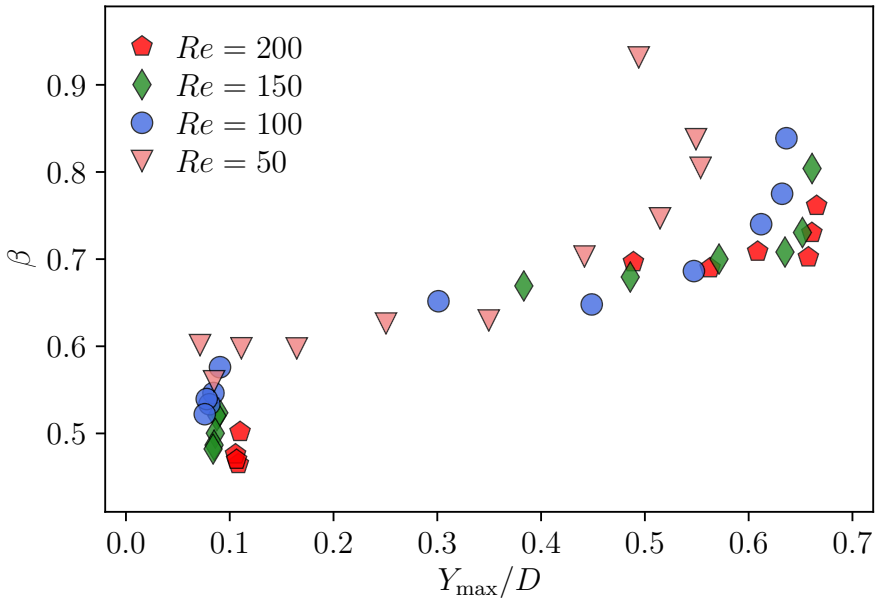

Figure D.7 Distortion coefficient versus transverse amplitude

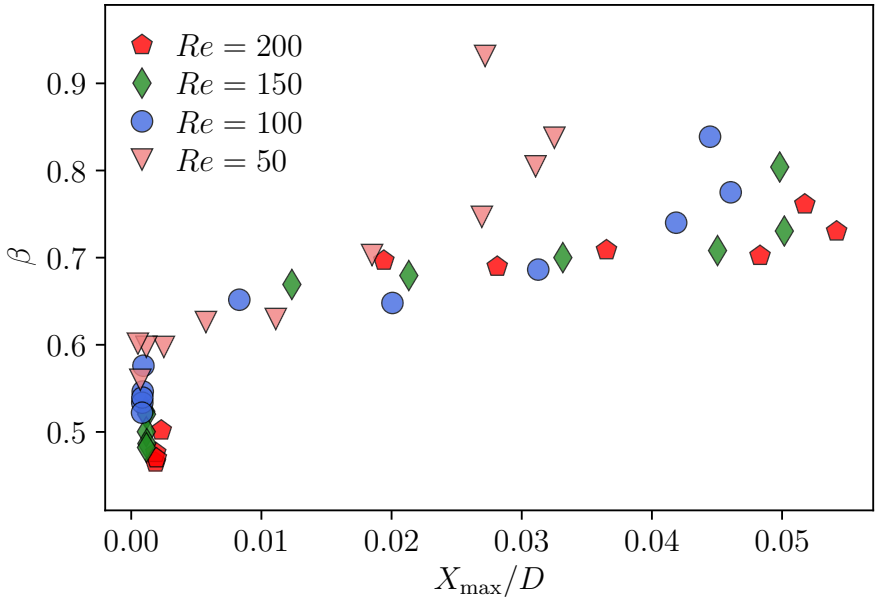

Figure D.8 Distortion coefficient versus stream-wise amplitude

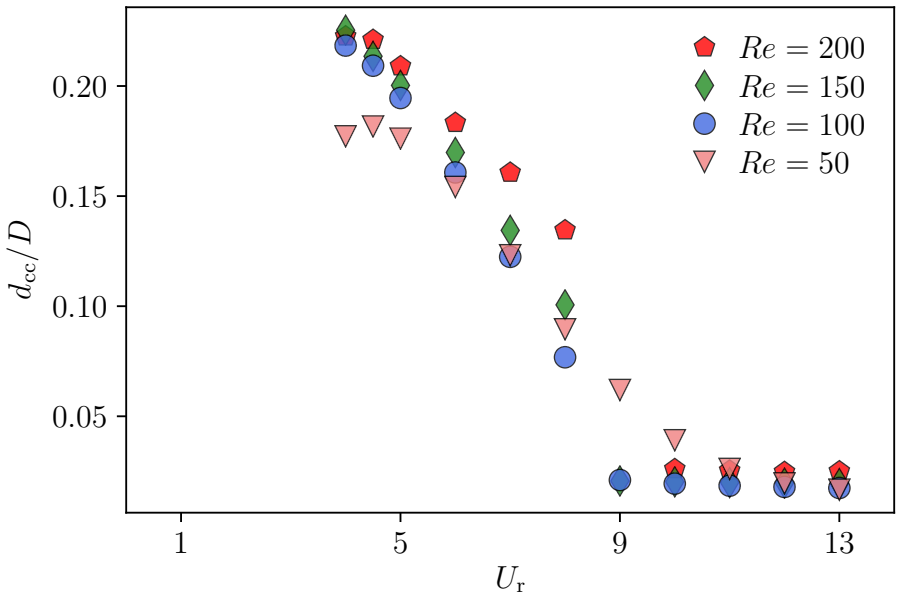

Figure D.9 Response of the counter-current distance response. Here again, since d_{cc} depends on the distortion coefficient, we cannot provide data for $U_r \leq 3.5$.

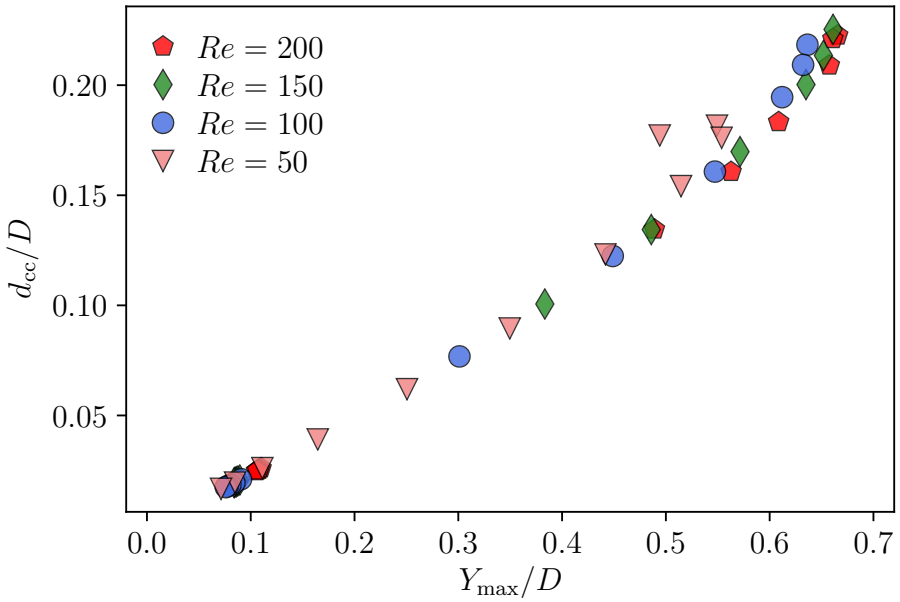

Figure D.10 Counter-current distance versus transverse amplitude

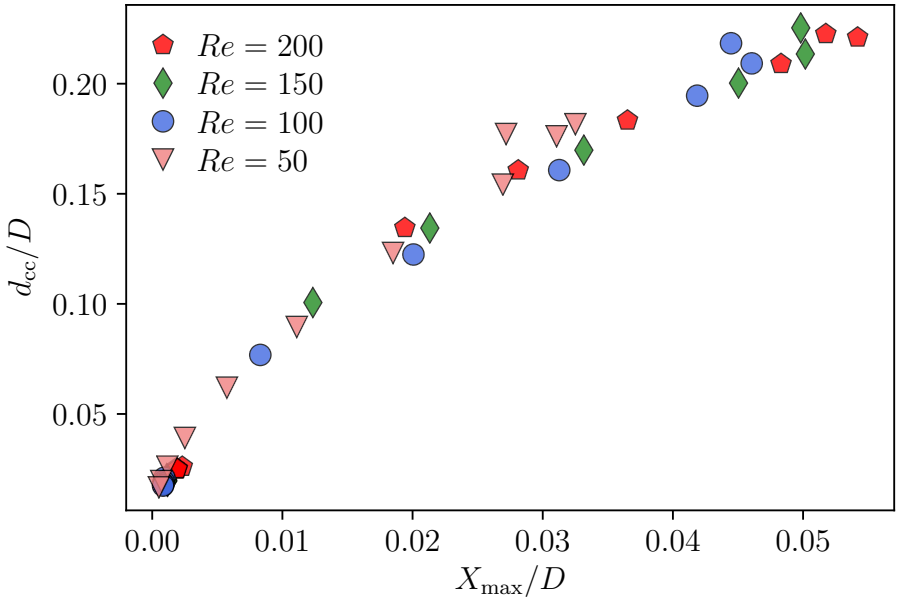

Figure D.11 Counter-current distance versus stream-wise amplitude

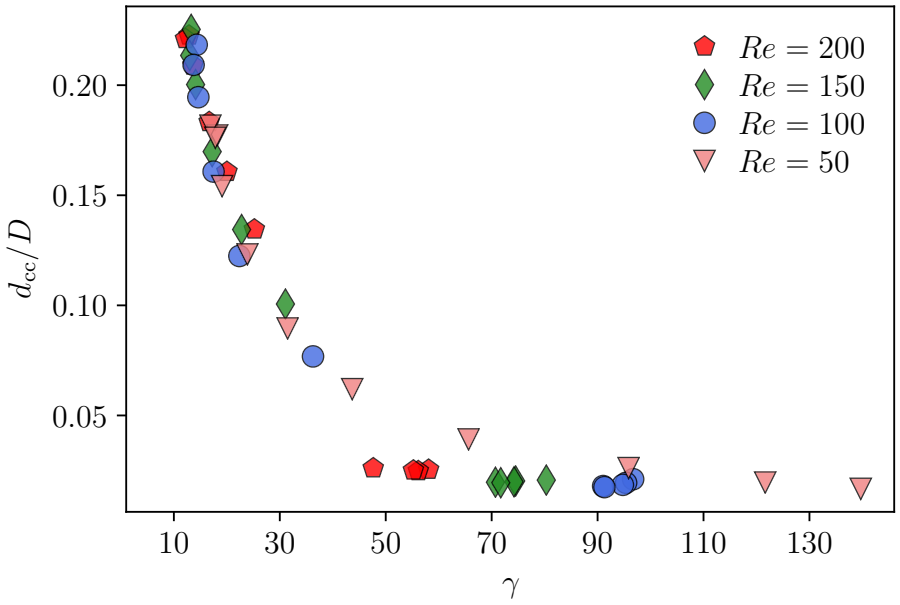

Figure D.12 Counter-current distance versus slenderness ratio

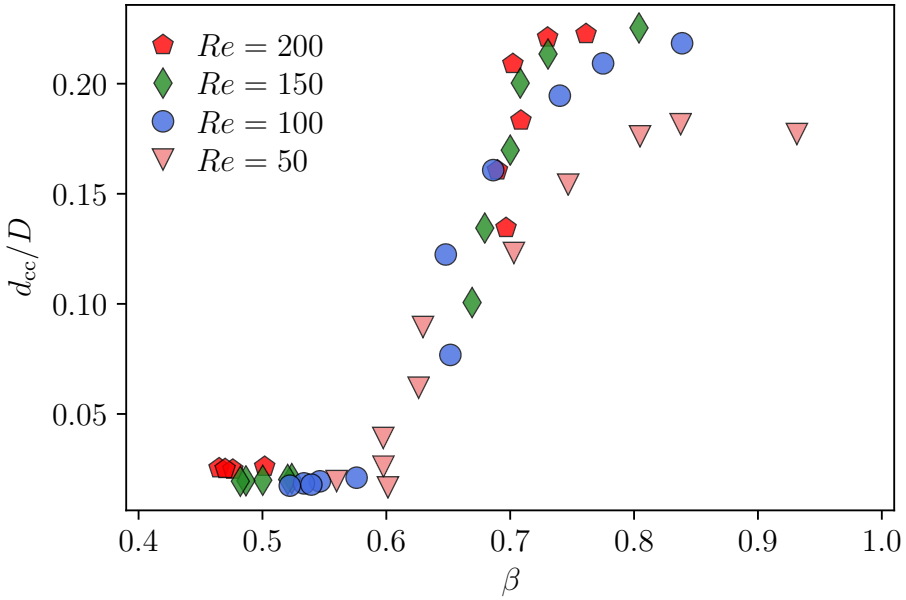

Figure D.13 Counter-current distance versus distortion coefficient

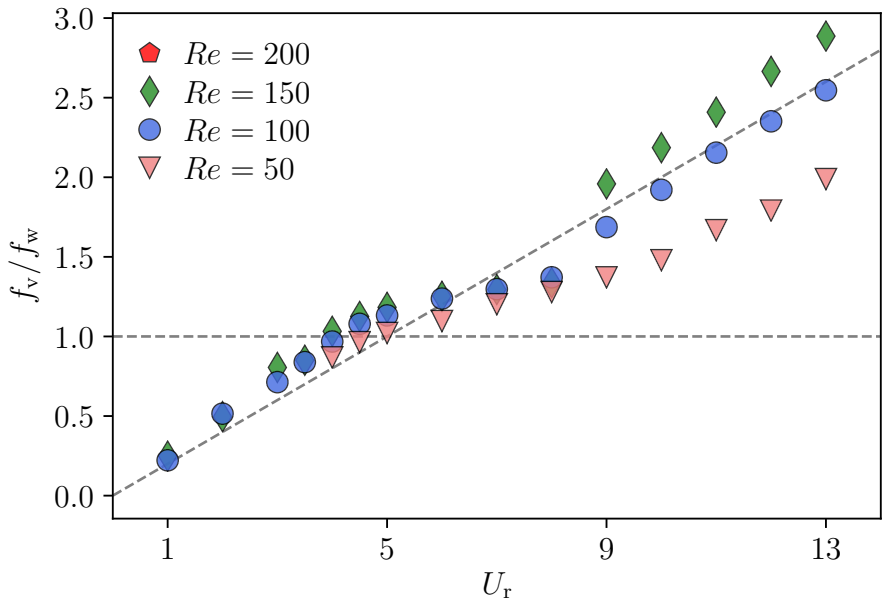

Figure D.14 Response of the vortex shedding frequency f_v normalised by the cylinder vibration frequency in water f_w (i.e. including the added mass $f_w = f_n/\sqrt{1+\pi/4}$).

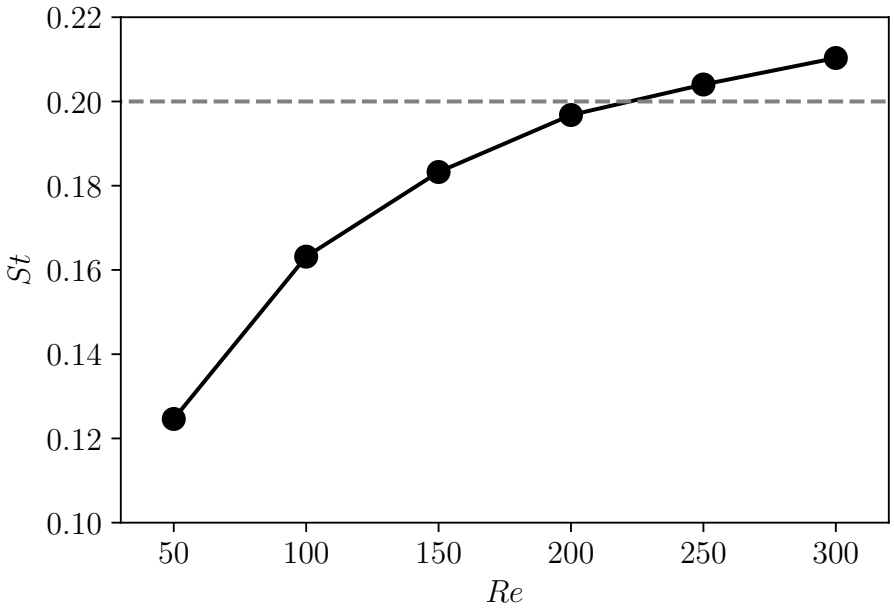

Figure D.15 Strouhal number $St = f_v D/U_0$ versus Reynolds number

APPENDIX E FENICS IMPLEMENTATION

This appendix describes the implementation of the rod simulations in FEniCS. We cover only the major steps of the code, and let the interested reader check the entire scripts at the Github page of the code [145]. Although this code is intended to solve the Kirchhoff equations, it might serve as a starting point for extended rod theories. Furthermore, the code formalism might be adapted, with the necessary modifications, for plate simulations using shell elements. We would like to acknowledge the demo of 'Elastic 3D beam structures' by Bleyer [146] which triggered the idea of simulating 1D structures in a 3D space.

Minimum working example for static simulations

Mesh

The first step in every FEniCS simulation is to create the model and generate the mesh. There are many ways to generate a meshed geometry in FEniCS, but the only way we found to create a geometry inside a domain of dimension strictly smaller than the space dimension (e.g. rods, shells in 3D space) is to generate an `.xml` file. The mesh stored in an `.xml` file has the following syntax

```
<dolfin xmlns:dolfin="http://www.fenicsproject.org">
  <mesh celltype="interval" dim="3">
    <vertices size="n_{v}">
      <vertex index="0" x="x0" y="y0" z="z0"/>
      <vertex index="1" x="x1" y="y1" z="z1"/>
      <vertex index="2" x="x2" y="y2" z="z2"/>
       ...
    </vertices>
    <cells size="n_{c}">
      <line index="0" v0="0" v1="1"/>
      <line index="1" v0="1" v1="2"/>
       ...
    </cells>
  </mesh>
</dolfin>
```

We create the mesh using

```
mesh = Mesh('filename')

coords   = mesh.coordinates()
n_coords = mesh.num_vertices()
```

Here `n_coords` is the number of vertices of the mesh, and `coords` is the (`n_coords`, 3) array of their coordinates.

Spaces

The solution space is composed of five unknowns, each of them being a vector. In FEniCS such a space is called a *mixed space*. We start by defining a vector finite element ($\mathcal{P}_1$ Lagrange element in this case)

```
cell = mesh.ufl_cell()

Ve = VectorElement('Lagrange', cell, degree=1)
```

then the solution space `V` is created through

```
element = MixedElement(Ve, Ve, Ve, Ve, Ve)
V = FunctionSpace(mesh, element)
```

We will also create a vectorial function space with a single vector finite element. It will serve us to create independent vectorial functions

```
Vt = FunctionSpace(mesh, Ve)
```

Material frame

In terms of the mesh, the tangential vector $\boldsymbol{t}_0$ of the initial configuration represents the normal facet of each interval element. First we save the facets into an array

```
facets = []
for k in range(n_coords):
    facets.append([Facet(mesh,k).normal(i) for i in range(3)])
facets = np.array(facets)
facets[0] *= -1
```

We flip the direction of the first facet because it points towards the exterior of the rod. The next step is to create a vectorial function, and assign it the values of the facets in each vertex

```
t0 = Function(Vt)

v2dt = vertex_to_dof_map(Vt)

T0 = t0.vector()[:]
for v in vertices(mesh):
    i = v.index()
    T0[v2dt[i*3:(i+1)*3]] = facets[i]
t0.vector()[:] = T0
```

Because the $\texttt{i}^{\text{th}}$ coordinate of the array `T0` does not correspond to its value at the vertex of index `i`, we need to map the vertices with the right degrees of freedom using `vertex_to_dof_map(Vt)`.

There is another alternative to assign a function. Taking the vector $\boldsymbol{n}_0$ as an example, we write

```
n0 = Function(Vt)

n0_ufl  = cross(t0, as_vector(u0))
n0_ufl /= sqrt(dot(n0_ufl, n0_ufl))

n0.assign(project(n0_ufl,Vt))
```

Here we used directly the definition of $\boldsymbol{n}_0$ in equation (7.13). One should notice that `n0_ufl` is a UFL expression, and requires the UFL representation of the force direction $\boldsymbol{u}_0$ using the function `as_vector`. We assign the values of the function `n0` by projecting its UFL representation on the space `Vt`.

Function declaration and initial conditions

Now we define the unknown vector `sol` with its test function `sol_`. Since the equilibrium equation involves the components of `sol` apart, we split it using the function `split` (not to confuse with the UFL method `.split()`)

```
t  , n  , Omega  , Fint  , w  = split(sol)
t_, n_, Omega_, Fint_, w_ = split(sol_)
```

We also define the binormal vector

```
b = cross(t, n)
```

Variational formulation

The derivative with respect to the curvilinear coordinate s equals the product of the gradient and the direction of the tangent $\partial/\partial s = \boldsymbol{t} \cdot \boldsymbol{\nabla}$. In FEniCS we define it as follows [146]

```
def tgrad(u):
    return dot(t0,grad(u))
```

Now we write each term of the lagrangian (7.40)

```
dwds = tgrad(w)
L_dwds = dot(dwds - t, w_)

dtds = tgrad(t)
L_dtds = dot(dtds - cross(Omega, t), t_)

dnds = tgrad(n)
L_dnds = dot(dnds - cross(Omega, n), n_)

M = Omega + (GJ/EI - 1)*dot(Omega, t)*t

dMds = tgrad(M)
L_dMds = dot(dMds - cross(Fint, t), Omega_)

dFds = tgrad(Fint)
L_dFds = dot(dFds + fext, Fint_)
```

The external force `fext` should be defined along the whole rod except at the root, where we let it free from any effort constraint. For this, we define an `Expression` through subclassing. We write

```
class ForceMagnitude(UserExpression):
        def __init__(self, magnitude, **kwargs):
            self.magnitude = magnitude
            super().__init__(**kwargs)
```

```
        def eval(self, values, x):
            if not(np.array_equal(x,coords[0])):
                values[0] = self.magnitude
            else:
                # i.e. don't apply at the root
                values[0] = 0

# Distributed load
distr_mag = ForceMagnitude(magnitude=f0, degree=3)
f_distr = distr_mag*u0_ufl

# Drag
un = np.dot(n, ufl_u0)
ub = np.dot(b, ufl_u0)

drag_mag = DragMagnitude(magnitude=Cd*Cy, degree=3)
f_drag = drag_mag*(un*abs(un)*n + ub*abs(ub)*b)
```

The interpolation degree in `distr_mag` and `drag_mag` is set to 3, but can be any order greater than the finite element order.

Finally, we obtain the variational form

```
F = (L_dtds + L_dnds + L_dMds + L_dFds + L_dwds)*dx(degree=1)
```

When the element is embedded in a space of a different dimension, it is important to specify the element order in the integral `dx(degree=1)`.

Boundary conditions

After defining the boundary domains in the geometry (which are points in our case, more precisely)

```
def root(x, on_boundary):
        return near(x[0], coords[0,0]) \
           and near(x[1], coords[0,1]) \
           and near(x[2], coords[0,2])
```

```
def tip(x, on_boundary):
    return near(x[0], coords[-1,0]) \
       and near(x[1], coords[-1,1]) \
       and near(x[2], coords[-1,2])
```

we apply the boundary conditions on variables in their respective subspaces

```
t_root = t0(coords[0])
n_root = n0(coords[0])

bc_t = DirichletBC(V.sub(0),
                   Constant((t_root[0], t_root[1], t_root[2])),
                   root)
bc_n = DirichletBC(V.sub(0),
                   Constant((n_root[0], n_root[1], n_root[2])),
                   root)

bc_Omega = DirichletBC(V.sub(2), Constant((0., 0., 0.)), tip)
bc_Fint  = DirichletBC(V.sub(3), Constant((0., 0., 0.)), tip)

bc = [bc_t, bc_n, bc_Omega, bc_Fint]
```

Solving

We solve the equation using the Newton method. We first calculate the Jacobian of the variational formulation

```
Jac = derivative(F, sol)
```

then initialise the solver

```
problem = NonlinearVariationalProblem(F, sol, bc, Jac)
solver  = NonlinearVariationalSolver(problem)

solver.parameters['newton_solver']['maximum_iterations']   = 50
solver.parameters['newton_solver']['relative_tolerance']   = 1e-6
solver.parameters['newton_solver']['absolute_tolerance']   = 1e-8
solver.parameters['newton_solver']['relaxation_parameter'] = 0.8
```

and finally launch the simulation

```
solver.solve()
```

Additional features for transient simulations

Additional variable

Since we reduce the temporal order of the governing equation by considering the new variable $\boldsymbol{v} = \dot{\boldsymbol{w}}$, the mixed function space `V` must have 6 subspaces

```
element = MixedElement(Ve, Ve, Ve, Ve, Ve, Ve)
V = FunctionSpace(mesh, element)
```

Also, because we consider a backward Euler scheme, we need to create the solution function `sol_old` of the prior time step

```
sol  = Function(V)
sol_ = Function(V)

sol_old = Function(V)
```

The function `sol_old` must be initialised with the initial configuration of the rod

```
S0 = sol_old.vector()[:]

for v in vertices(mesh):
    i = v.index()

    t0_i = t0(coords[i])
    n0_i = n0(coords[i])

    Omega0_i = Omega0(coords[i])
    Fint0_i  = Fint0(coords[i])

    w0_i = coords[i]
    v0_i = [0., 0., .0] # zero initial velocity

    S0[v2d[i*18+ 0:i*18+ 3]] = t0_i
    S0[v2d[i*18+ 3:i*18+ 6]] = n0_i
```

```
    S0[v2d[i*18+ 6:i*18+ 9]] = Omega0_i
    S0[v2d[i*18+ 9:i*18+12]] = Fint0_i
    S0[v2d[i*18+12:i*18+15]] = w0_i
    S0[v2d[i*18+15:i*18+18]] = v0_i

sol_old.vector()[:] = S0
```

The function `Omega` and `Fint` can be created with the same method we explained above for the vector $\boldsymbol{n}_0$ using equations (7.52) and (7.53).

Time-dependent forces

In the case where the upstream velocity is time-dependent, we consider an `Expression` of the normalised speed $U(t)/U_0$ that comprises the time variable

```
class Speed(UserExpression):
    def __init__(self, t_n, **kwargs):
        self.t_n = t_n

        super().__init__(**kwargs)

    def eval(self, values, x):
        speed = speed_function(self.t_n)
        values[0] = speed

u_rel = speed*u0_ufl - lmbda*v

un = np.dot(n, u_rel)
ub = np.dot(b, u_rel)

drag_mag = ForceMagnitude(magnitude=Cd*Cy, degree=3)
fext = drag_mag*(un*abs(un)*n + ub*abs(ub)*b)
```

where the function `speed_function` returns the normalised speed at `t_n`. Notice that in the dimensionless relative velocity `u_rel`, the parameter `lmbda` should not be a time-dependent expression because it is inversely proportional to the speed magnitude U_0 – not the variable speed $U(t)$ – as in equation (7.26).

After splitting the mixed variables `sol` and `sol_old`, we add the definition of $\boldsymbol{v}$ and the discretised acceleration into the internal stress equation

```
L_dFds = dot(dFds + fext - (v - v_old)/dt, Fint_)
L_dwdt = dot((w - w_old)/dt - v, v_)
```

in order to finally obtain

```
L = L_dwds + L_dtds + L_dnds + L_dMds + L_dFds + L_dwdt
F = L*dx(degree=1)
```

Time integration

A possible implementation layout of the time integration loop is

```
t_n = 0

for n in range(Nt):
    t_n += dt

    ############
    # Update the value of all time-dependent expressions
    drag_mag.t_n = t_n
    ...
    ############

    solver.solve()

    ############
    # Results extraction
    ############

    sol_old.assign(sol)
```